

NONLINEAR FINITE ELEMENT ANALYSES OF THE END WEB CRIPPLING STRENGTH OF W-SHAPE STEEL BEAMS

by

José Abigail Marcano

Thesis submitted to the faculty of the
Virginia Polytechnic Institute and State University
in partial fulfillment of the requirements for the degree of

MASTER OF SCIENCE
IN
CIVIL ENGINEERING

APPROVED:

Thomas M. Murray, Chairman

W. Samuel Easterling

Carin L. Roberts-Wollmann

August 2002

BLACKSBURG, VIRGINIA 24061

Keywords: Web Crippling; Finite Element; ANSYS; Geometric Imperfections; Large Deformations; Material Nonlinearities.

NONLINEAR FINITE ELEMENT ANALYSES OF THE END WEB CRIPPLING STRENGTH OF W-SHAPE STEEL BEAMS

by

José Abigail Marcano

Thomas M. Murray, Chairman

Structural Engineering and Materials Program

Charles E. Via Department of Civil Engineering

Virginia Polytechnic Institute and State University

(ABSTRACT)

The 1999 AISC Specification for Structural Steel Buildings establishes two design equations for the web crippling limit state at the supports. However, investigators have suggested that the basis of these equations, which is based on an assumed collapse mechanism, is conservative especially for long bearing lengths. Most of the experimental studies conducted to validate those formulas have considered short span lengths and relatively small bearing-to-depth ratios. Therefore, a further investigation of the web crippling capacity of W-shape steel beams for larger span lengths and larger bearing-to-length ratios was undertaken.

The primary objective of this study is to analytically investigate the web crippling strength of W-shape steel beams for large bearing-to-depth ratios on large span beams, and to compare the results with the 1999 AISC LRFD web crippling design equation (K1-5b). The web crippling strength of W-shape steel beams was investigated by means of the finite element technique. The commercial finite element package ANSYS 6.0 was used to model the steel beams. Material nonlinearities, large deformation effects and initial geometric imperfections were taken into account in the finite element models.

The validation results shown that the finite element models closely predicted the ultimate load and web crippling failure mode shape of the tested beams. Conclusions based on the predictions of the finite element analyses and the current 1999 AISC end web crippling design equation (K1-5b) are presented in the study.

ACKNOWLEDGEMENTS

I would like to sincerely thank my advisor Dr. Thomas M. Murray for his generosity, patience, and guidance throughout this thesis and my graduate program. His thoughtfulness and willingness to help are deeply appreciated. It has been a pleasure to have him as a professor as well as a mentor. My gratitude and appreciation also go to Dr. Finley A. Charney for his guidance and advice in computer modeling, and to Dr. W. Samuel Easterling and Dr. Carin L. Roberts-Wollmann for serving as members of my committee.

Next, I would like to thank Dr. Scott W. Case for providing me with the commercial finite element package, ANSYS, and to Ms. Sherry Yavelak for taking time to save my data in compact discs. Thanks also go to my fellows students William M. Downs and Youngjin Woo for taking time to share with me their knowledge of computer modeling.

I would like to thank my friends Miguel Pando, José L. Perdomo, and Juan C. Piñero for giving me their advice and help throughout my graduate studies. Thanks also go to Christy J. Butler for her love and encouragement during the last year of my graduate studies. Thank you guys and gal for cheering me up in difficult times!

Most importantly, I would like to thank my parents, Mrs. Rufina Rivera and Mr. Abigail Marcano, my brother Luis, and my sister Evelyn for being such an inspirational influence in my life. Their love, support, and encouragement throughout my academic career have allowed me to make it this far. This work is dedicated to all of you, “*Los Amo Mucho*”.

Finally, I thank God, the Father Almighty, for giving me health, strength, and wisdom in order to achieve my goals. “*Sin Ti no soy nada, y Contigo lo tengo todo...Amen*”.

TABLE OF CONTENTS

	Page
ACKNOWLEDGEMENTS	iv
LIST OF FIGURES	vii
LIST OF TABLES	xi
CHAPTER	
I. INTRODUCTION AND LITERATURE REVIEW	1
1.1 Introduction	1
1.2 Literature Review	4
1.2.1 Experimental Studies	4
1.2.2 Finite Element Studies	10
1.3 Scope of the Research	14
1.4 Thesis Outline	15
II. EXPERIMENTAL STUDIES AND RESULTS	16
2.1 General	16
2.2 Elgaaly and Salkar	16
2.3 Bryant	20
III. FINITE ELEMENT MODEL DETAILS	24
3.1 General	24
3.2 Mesh Elements	24
3.3 Material Properties	26
3.4 Boundary Condition	28
3.5 Loading	29
3.6 Geometric Imperfections	31
3.7 Solution Options	34
IV. FINITE ELEMENT RESULTS, COMPARISONS AND DISCUSSION	36
4.1 GENERAL	36
4.2 Sensitivity Analysis	37
4.2.1 Type of Shell Element	37

4.2.2 Imperfection Size Sensitivity	38
4.2.3 Element Size Sensitivity	40
4.3 Finite Element Results and Comparisons	43
4.3.1 Validation Analysis	43
4.3.1.1 Non-composite Models	44
4.3.1.2 Steel-Concrete Composite Models	49
4.3.2 Parametric Analysis	50
4.3.2.1 Non-composite Models	52
4.3.2.2 Steel-Concrete Composite Models	61
4.4. Discussion	66
V. SUMMARY AND CONCLUSIONS	72
5.1. Summary	72
5.2. Conclusions	73
REFERENCES	75
APPENDIX	
A. CREATING AND ANALYZING THE FE MODEL	77
B. FINITE ELEMENT RESULTS	96
C. ADDITIONAL SCREENED END WEB CRIPPLING DATA	108
VITA	113

LIST OF FIGURES

	Page
FIGURE	
1.1 Typical testing configuration for web crippling at an interior patch load	2
1.2 Typical testing configuration for web crippling over the support	2
1.3 A second testing configuration for web crippling over the support	3
1.4 Typical failure mechanism observed from experimental tests	7
1.5 Roberts' assumed collapse mechanism for web crippling at an interior patch load	7
1.6 Inconsistencies in the end web crippling derivation as a result of halving the interior web crippling equation	9
1.7 Cross-sectional web imperfections	13
3.1 Stress-strain relationship defined in the finite element analyses	28
3.2 Flange-to-bearing connection in the finite element analyses	30
3.3 Restraints in the composite models as defined in the finite element analyses	30
3.4 Assumed web imperfection	32
3.5 View of the geometrical imperfection pattern in the finite element model	32
3.6 Newton-Raphson interaction coupled with arc-length method	35
4.1 Behavior of the model FEA-15a with different shell-type elements	37
4.2 Web imperfection sensitivity for the model FEA-14a	39
4.3 Web imperfection sensitivity for the model FEA-4a	39
4.4 Element size sensitivity for the model FEA-14a	41
4.5 Element size sensitivity for the model FEA-4a	41
4.6 Load deflection response of the model FEA-14a	45
4.7 Load deflection response of the model FEA-15a	45
4.8 Load deflection response of the model FEA-4a	46
4.9 Load deflection response of the model FEA-7a	47
4.10 Load deflection response of the model FEA-7b	47
4.11 Load-deflection response of the model FEA-4b	48

4.12	Load-deflection response of the model FEA-SC-2a	50
4.13	Load-deflection response of the model FEA-14b, W12x16 with N = 3.0 in.	53
4.14	Load-deflection response of the model FEA-14c, W12x16 with N = 4.0 in.	54
4.15	Load-deflection response of the model FEA-7c, W12x16 with N = 5.0 in.	54
4.16	Load-deflection response of the model FEA-7d, W12x16 with N = 6.0 in.	55
4.17	Load-deflection response of the model FEA-7e, W12x16 with N = 7.0 in.	55
4.18	Load-deflection response of the model FEA-7f, W12x16 with N = 8.0 in.	56
4.19	Load-deflection response of the model FEA-7g, W12x16 with N = 9.0 in.	56
4.20	Load-deflection response of the model FEA-7h, W12x16 with N = 10.0 in.	57
4.21	Load-deflection response of the model FEA-7i, W12x16 with N = 11.0 in.	57
4.22	Typical web crippling shape at different load steps for models with relatively small bearing-to-depth ratio	59
4.23	Web crippling shape at the end of the beam section at different load steps of the model FEA-7i	60
4.24	Web crippling shape at 5.0 in. from the end of the beam section at different load steps of the model FEA-7i	60
4.25	Load-deflection response of the model FEA-SC-2b, W14x22 with N = 4.43 in.	62
4.26	Load-deflection response of the model FEA-SC-2c, W14x22 with N = 5.36 in.	63
4.27	Load-deflection response of the model FEA-SC-2d, W14x22 with N = 7.22 in.	63
4.28	Load-deflection response of the model FEA-SC-2e, W14x22 with N = 9.02 in.	64
4.29	Load-deflection response of the model FEA-SC-2f, W14x22 with N = 10.93 in.	64
4.30	Web crippling shape at 10.0 in. from the end of the beam different load steps of the model FEA-SC-2f	65
4.31	Comparison between the experimental and FE web crippling failure Mode shapes	68
4.32	FEM failure load-to-AISC load ratio versus bearing-to-depth ratio	69
4.33	Prediction accuracy of the 1999 AISC LRFD web crippling equations on a W12x16 section	70
4.34	Prediction accuracy of the 1999 AISC LRFD web crippling equations on a W16x31 section	70

4.35	Prediction accuracy of the 1999 AISC LRFD web crippling equations on a W14x22 section	71
B.1	Web crippling shape at different load steps of the model FEA-14a	97
B.2	Web crippling shape at different load steps of the model FEA-14b	97
B.3	Web crippling shape at different load steps of the model FEA-14b	98
B.4	Web crippling shape at different load steps of the model FEA-15a	98
B.5	Web crippling shape at different load steps of the model FEA-4a	99
B.6	Web crippling shape at different load steps of the model FEA-4b	99
B.7	Web crippling shape at different load steps of the model FEA-7a	100
B.8	Web crippling shape at different load steps of the model FEA-7b	100
B.9	Web crippling shape at different load steps of the model FEA-7c	101
B.10	Web crippling shape at different load steps of the model FEA-7d	101
B.11	Web crippling shape at different load steps of the model FEA-7e	102
B.12	Web crippling shape at different load steps of the model FEA-7f	102
B.13	Web crippling shape at different load steps of the model FEA-7g	103
B.14	Web crippling shape at different load steps of the model FEA-7h	103
B.15	Web crippling shape at different load steps of the model FEA-7i	104
B.16	Web crippling shape at different load steps of the model FEA-SC-2a	104
B.17	Web crippling shape at different load steps of the model FEA-SC-2b	105
B.18	Web crippling shape at different load steps of the model FEA-SC-2c	105

B.19	Web crippling shape at different load steps of the model	
	FEA-SC-2 <i>d</i>	106
B.20	Web crippling shape at different load steps of the model	
	FEA-SC-2 <i>e</i>	106
B.21	Web crippling shape at different load steps of the model	
	FEA-SC-2 <i>f</i>	107

LIST OF TABLES

	Page
TABLE	
2.1 Summary of the geometric and material properties for the first set of tests conducted by Elgaaly and Salkar	17
2.2 Summary of the geometric and material properties for the second set of tests conducted by Elgaaly and Salkar	18
2.3 Summary of the screened web crippling strength results from experimental studies conducted by Elgaaly and Salkar	19
2.4 Summary of the geometric and material properties for the steel beam of the tests conducted by Bryant	21
2.5 Summary of the geometric and material properties for the concrete slab and shear studs of the tests conducted by Bryant	22
2.6 Position and maximum end reaction for each load location of the tests conducted by Bryant (1993)	23
2.7 Summary of the screened web crippling strength results from experimental studies conducted by Bryant	23
3.1 Description of the Capabilities of Elements <i>SHELL143</i> and <i>SHELL181</i>	25
3.2 Corresponding λ -and L_0 -values for each W section	34
4.1 Summary of the imperfection sensitivity results for the models FEA-14a and FEA-4a	40
4.2 Summary of the element sensitivity results for the models FEA-14a and FEA-4a	42
4.3 Designation of each validation model and its relation with experimental data	43
4.4 Summary of the characteristics of each analysis model	51
4.5 Summary and comparison between the FE web crippling strength results of the non-composite models and the predictions of the 1999 AISC LFRD web crippling equation (K1-5b)	58
4.6 Summary and comparison between the FE web crippling strength results of the composite models and the predictions of the 1999 AISC LFRD web crippling (K1-5b)	65

4.7	Summary of the finite element analyses with different shear span-to-depth ratios	67
C.1	Summary of the geometric and material properties for the series F tests conducted by Ketchum and Draffin	109
C.2	Summary of the geometric and material properties for the midspan-loaded Series K tests conducted by Ketchum and Draffin	110
C.3	Summary of the geometric and material properties for the midspan-loaded series K tests conducted by Ketchum and Draffin, and which the beam was projected beyond the outer edge of the bearing block	111
C.4	Summary of the screened web crippling strength results from experimental studies conducted by Ketchum and Draffin	112

NONLINEAR FINITE ELEMENT ANALYSES OF THE END WEB CRIPPLING STRENGTH OF W-SHAPE STEEL BEAMS

CHAPTER 1

INTRODUCTION AND LITERATURE REVIEW

1.1 Introduction

Webs of W-shape steel beams are subjected to in-plane compressive loading in many engineering designs. The failure modes induced by concentrated in-plane compressive loads are yielding and crippling of the web material in a local area under the load. Transverse stiffeners can be used to reinforce the web so that web crippling does not occur; however, the use of transverse stiffeners is minimized or avoided for practical and economic reasons.

The loading configuration considered to study interior web crippling behavior is shown in Figure 1.1, while the loading configuration frequently considered to study the web behavior over the support is shown in Figure 1.2. Figure 1.3 shows an alternative loading configuration to study the web crippling at the supports. As shown in the three figures, the beam is simply supported and the load is applied at the top of the flange and centered on the web of the beam section to study web crippling. To study interior web crippling, transverse stiffeners are designed to reinforce the web over the supports such that the web fails in a local area under the application of the load. When failure of the web is wanted at a support, transverse stiffeners are designed to reinforce the web under the loaded patch. The test beam section is often laterally braced to prevent torsional buckling.

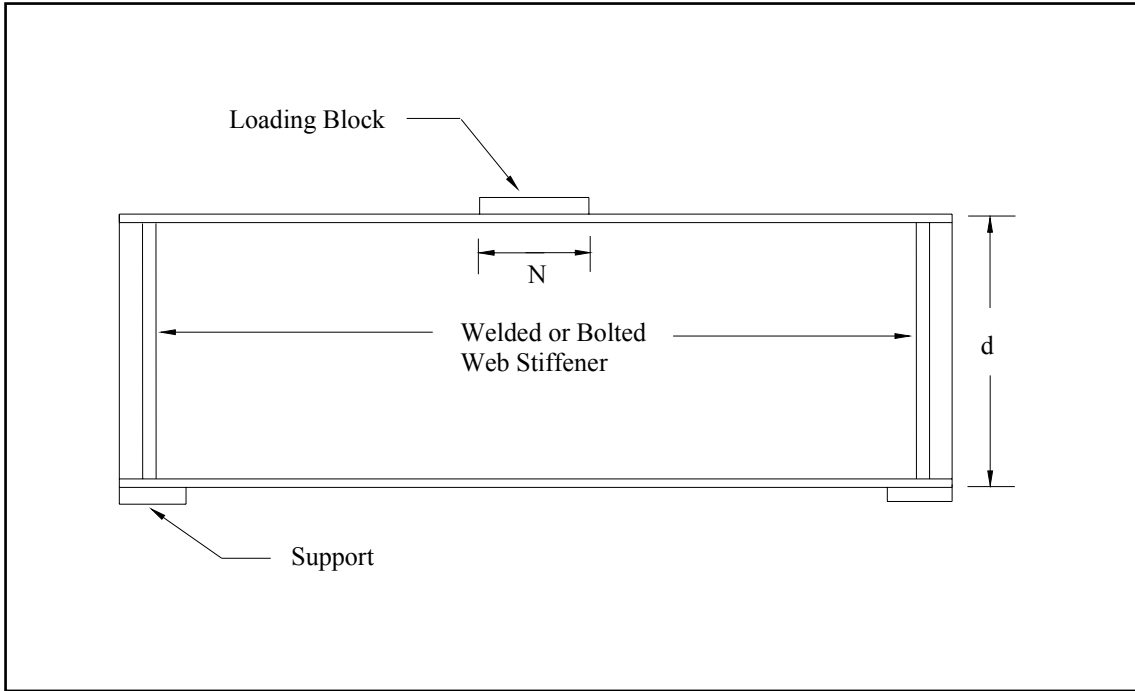


Figure 1.1 Typical testing configuration for web crippling at an interior patch load.

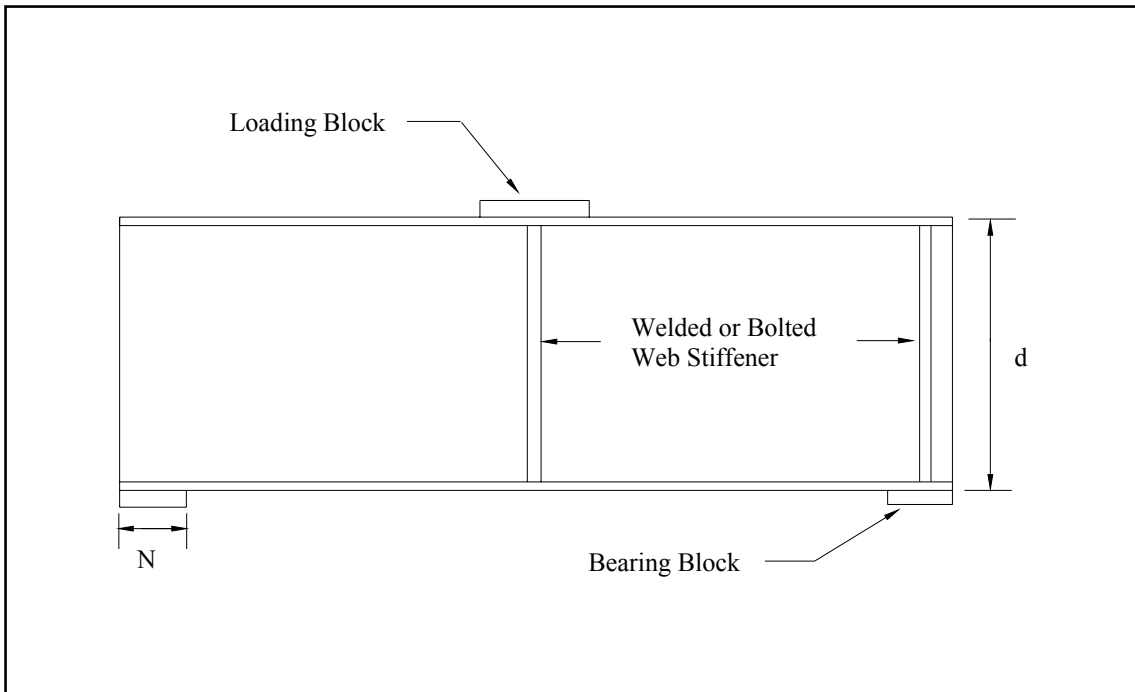


Figure 1.2 Typical testing configuration for web crippling over the support.

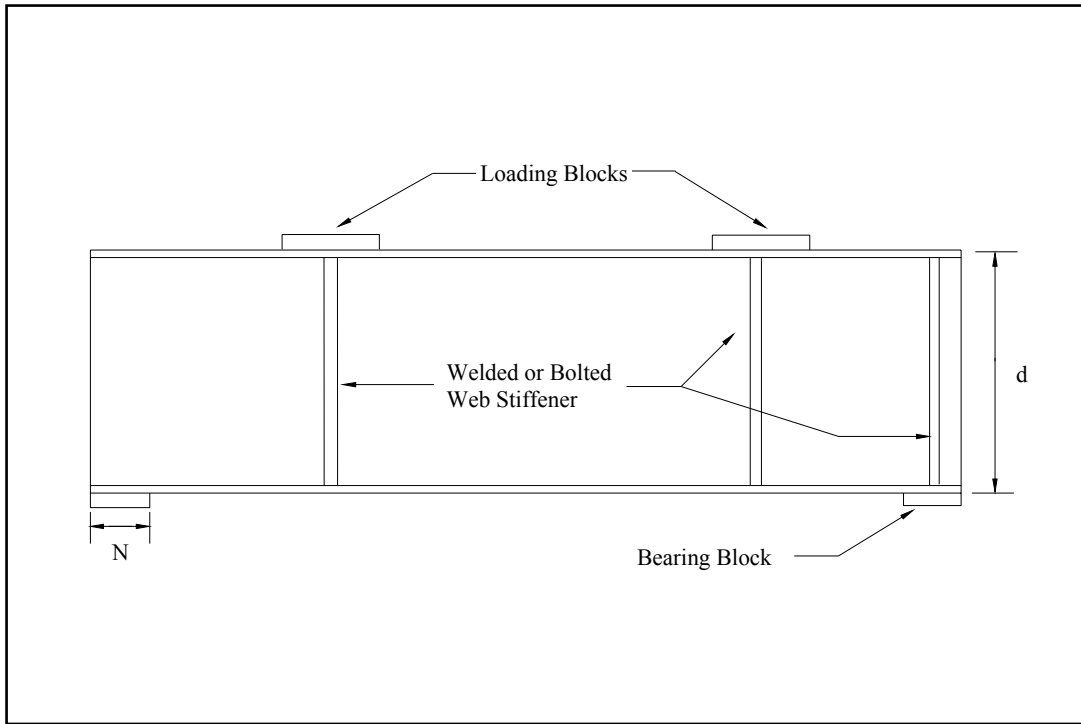


Figure 1.3 A second testing configuration for web crippling over the support.

Since web crippling can occur either under the application of the concentrated load or over the supports, both situations have been investigated since the early 1930's. Both experimental and analytical studies have been conducted to predict the ultimate strength of the webs due to crippling failure, and several formulae have been proposed to predict the web crippling strength of steel beams. Majority of these studies are summarized by Rockey (1976), Roberts and Rockey (1979), and Elgaaly (1983).

The 1999 AISC LRFD Specification for Structural Steel Buildings (AISC, 1999) establishes two design equations for the web crippling limit state at the supports. However, the basis of the web crippling limit state at the support, which is indirectly derived from an assumed interior collapse mechanism, is believed to be conservative for large bearing lengths, N . Also, most of the experimental studies conducted to calibrate the 1999 AISC LRFD web crippling equation (K1-5b) used short span lengths and relatively small bearing-to-depth ratios.

The objectives of this study are to develop a finite element model that can predict the web crippling failure load of test specimens, to investigate the web crippling strength of W-shape steel beams for large bearing-to-length ratios on realistic span beams, and to compare the results with the predictions of the 1999 AISC LRFD web crippling design equation (K1-5b). The commercial finite element package, ANSYS 6.0, is used to for this purpose.

1.2 Literature Review

1.2.1 Experimental Studies

One of the first experimental studies to consider webs under compressive loads was conducted in the early 30's, when Ketchum and Draffin (1932) tested 66 light W-shape steel beams for failure of the web over the supports. Ketchum and Draffin observed that the ultimate collapse load for those beam sections tested with a single concentrated load located at midspan (Figure 1.1) was slightly higher than those same beam sections tested with two concentrated loads located at quarter points (Figure 1.2). The difference was about 10% of the ultimate load capacity. They attributed this effect to the fact that, in the second testing configuration, the load was applied at a distance equal to one-half of the beam depth. This loading configuration may have caused the beam to fail due to direct compression loads. In general, they concluded that the failure of the beams was due to buckling of the web over the support. They also concluded that the stress, which caused web crippling, could be closely approximated by the so-called Carnegie formula:

$$\sigma_b = \frac{R_n}{t_w \left(N + \frac{d}{4} \right)} \quad (1.1)$$

where:

σ_b : Allowable bearing stress, ksi

R_n : End reaction, kips

N : Bearing length, in.

d : Depth of the section, in.

t_w : Web thickness, in.

Bergfelt (1976) conducted several tests on plate girders to study the parameters that affect the strength of the web material under edge compressive loads. He observed an increase in the ultimate load capacity of the web with an increase in the flange-to-web thickness ratio, t_f/t_w . Bergfelt considered the influence of the web yield stress, F_y , and the modulus of elasticity, E , and proposed the following equation to predict the web crippling strength of steel girders.

$$R_n = 0.68t_w^2(EF_{yw})^{0.5}\left(\frac{t_f}{t_w}\right)^{0.6} \quad (1.2)$$

where:

E : Modulus of Elasticity, ksi

F_{yw} : Yield Stress of the web, ksi

t_f : Flange thickness, in.

Bergfelt was one of the first authors to propose a design formula for predicting the web crippling failure load. Subsequently, several other formulae have been proposed to predict the web crippling strength of welded plate girders. Those formulae are summarized in the papers published by Rockey (1976), Roberts and Rockey (1979) and Elgaaly (1983). Roberts and Rockey (1979) summarized and analyzed the design formulae proposed by other investigators to predict the ultimate load due to web crippling failure. Most important, Roberts and Rockey developed an assumed collapse mechanism, based on experimental observations, to predict the ultimate load for web crippling. The

typical failure mechanism observed from experimental tests is shown in Figure 1.4, while the collapse mechanism considered by Roberts and Rockey is shown in Figure 1.5. Based on this collapse mechanism and yield line theory, they derived an expression to predict the collapse load of the web. Two years later, Roberts (1981) conducted a series of experimental studies to validate the mechanism solution. Based on experimental observations, he reduced the original mechanism solution to a simple form. He concluded that the simple formula provided satisfactory predictions of the ultimate load for all the available data. However, he recommended that the formula should be limited for bearing-to-depth ratios, N/d , less than 0.2. He mentioned that when N/d becomes larger, the flange will not remain flat between the inner plastic hinges, and therefore this assumption becomes no longer valid. The semi-empirical formula developed by Robert is:

$$R_n = 135 t_w^2 \left[1 + 3 \left(\frac{N}{d} \right) \left(\frac{t_w}{t_f} \right)^{1.5} \right] \sqrt{F_{yw} \frac{t_f}{t_w}} \quad (1.3)$$

This new formula was introduced in the 1986 AISC LRFD Specification (AISC, 1986), and only applies to interior patch loads. The AISC LRFD strength for end reactions is approximately one-half of that given by Equation 1.3:

$$R_n = 68 t_w^2 \left[1 + 3 \left(\frac{N}{d} \right) \left(\frac{t_w}{t_f} \right)^{1.5} \right] \sqrt{F_{yw} \frac{t_f}{t_w}} \quad (1.4)$$

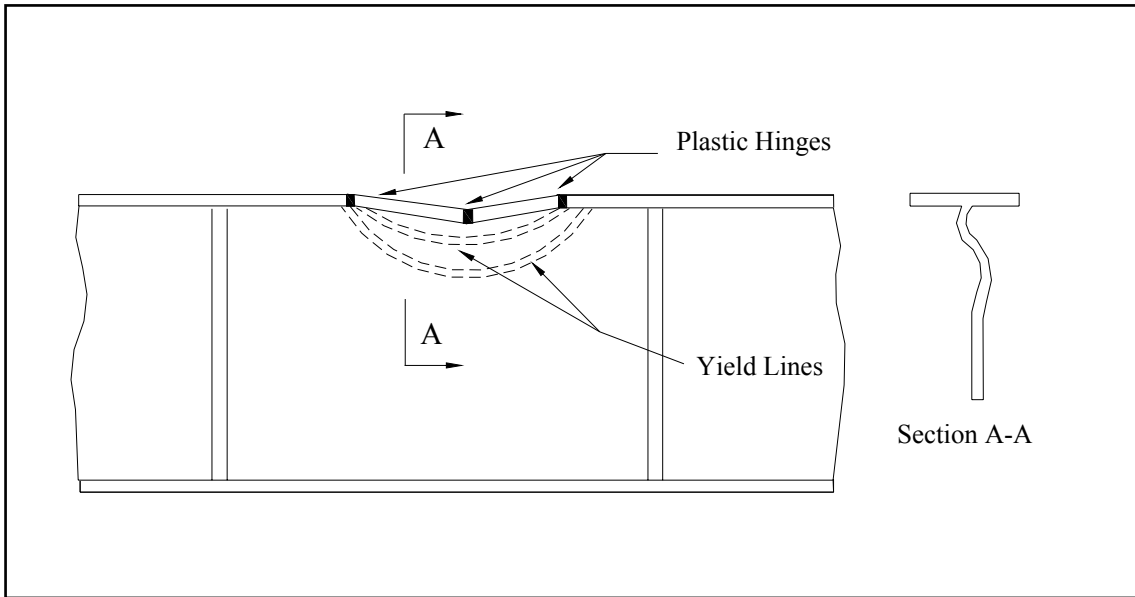


Figure 1.4 Typical failure mechanism observed from experimental tests.

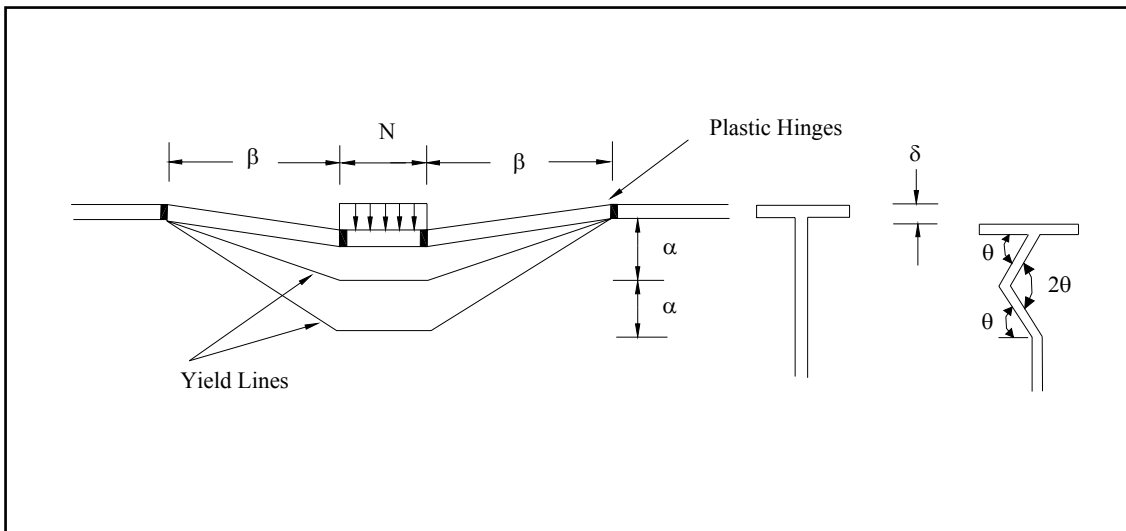


Figure 1.5 Roberts' assumed collapse mechanism for web crippling at an interior patch load.

Elgaaly and Salkar (1991) conducted a series of tests to study the ultimate load capacity of web crippling over the supports to validate the 1986 AISC LRFD (AISC, 1986) web crippling equation (K1-5). They tested twenty-seven hot-rolled steel beams of

short span, where thirteen out of the twenty-seven were loaded at a distance from the face of the support less than the depth of the section. Based on the results, they observed a tendency for the test load-to-calculated load ratios, P_{ts}/P_{uc} , to increase with increasing N/d ratio. They concluded that the 1986 AISC LRFD design equation for web crippling over the support is conservative. Based on those results, the 1993 AISC LRFD Specification (AISC, 1993) introduced a new set of equations for end web crippling limit state. The equation K1-5a is identical to equation K1-5 of the 1986 AISC LRFD Specification, and applies when the bearing-to-depth ratio, N/d is less than 0.2. The new equation, K1-5b, is written as follows:

$$R_n = 68t_w^2 \left[1 + \left(4 \frac{N}{d} - 0.2 \right) \left(\frac{t_w}{t_f} \right)^{1.5} \right] \sqrt{F_{yw} \frac{t_f}{t_w}} \quad (1.5)$$

The new equation K1-5b, which applies when the N/d ratio is greater than 0.2, gives slightly higher strength values than the previous equation K1-5. However, most of the tests conducted by Elgaaly and Salkar used to calibrate this new equation were conducted on short span length beams with the shear span less than 3/4th of the depth of the beams. This loading configuration could alter the behavior of the web since it may have induced direct compression, and thus influence the ultimate collapse load of the steel beams. In fact, Ketchum and Draffin (1932) observed a decrease of 10% in the ultimate load for those beams tested with shear span less than the depth of the section versus the same beam sections tested with shear span-to-depth ratio greater than 1.0.

Since few experimental data were available to better assess the web crippling strength over the support, the American Institute of Steel Construction (AISC) called for additional research on this subject. Bryant (1993) conducted an experimental study, sponsored by the AISC, to examine the origin of the equation for web crippling at the supports, which was obtained indirectly from Roberts' derivation for interior web crippling. He identified inconsistencies in the end web crippling derivations as a result of using the same assumptions as for the interior web crippling derivation. One of those

inconsistencies is apparent from Figure 1.6. Based on this and other inconsistencies, he developed a new and more realistic collapse mechanism, and derived a new equation specifically for web crippling failure at the supports. The new proposed end web crippling equation is:

$$R_n = 24t_w^2 \left[\sqrt{F_{yw} \frac{t_f}{t_w}} + 48 \left(\frac{c}{b_f} \right) \left(\frac{t_w}{t_f} \right) \right] \quad (1.6)$$

where:

$$c = N + k$$

k : Vertical fillet distance of the section, in.

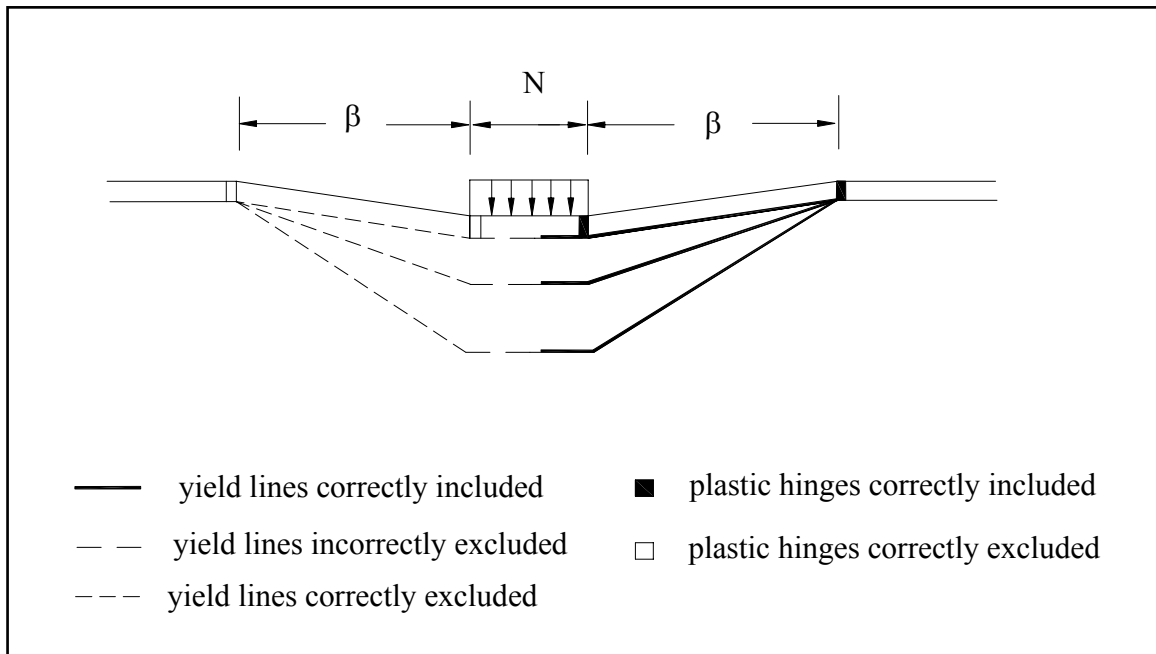


Figure 1.6 Inconsistencies in the end web crippling derivation as a result of halving the interior web crippling equation.

In addition, five full-scale tests were conducted to verify the accuracy of the proposed equation. Three of those tests were performed using steel-concrete composite beams. The proposed new equation for end web crippling accurately predicted the

collapse load for these tests. However, an evaluation of the equation with historical experimental data demonstrated that the 1993 AISC LRFD web crippling equation (K1-5b) better predicts the ultimate collapse load of the web crippling over the supports than the proposed new equation. Bryant pointed out that the methods of testing in previous experimental studies have a significant effect on the web crippling strength of the steel beams. Most of the beams tested in previous experimental studies were not laterally braced and were loaded by a point load located very near to the end bearing connection.

1.2.2 Finite Element Studies

The finite element method is a numerical technique developed in the early 1940's by aircraft structural engineers to better approach the analysis of complex airframes. Since then, many mathematicians, physicists, and engineers have made significant contributions to the finite element method which, along with high-speed digital computers, has become widely accepted as a valuable numerical technique for solving complex engineering problems. Most important, this technique is an effective way to assess the response of the structural elements compared to full-scale experiments since it is relatively inexpensive and time efficient.

The behavior of webs under interior compressive loads has been recently studied by the mean of the finite element technique. Granath (1997), by using the commercial finite element package ABAQUS 5.4, studied the influence of the moment capacity and stiffness of the flanges on the ultimate web crippling load. He created and analyzed three finite element models for interior patch loading similar to the specimens tested by Roberts (1981). The elements used to model the plate girders were shell elements. Granath modeled the ends of the girders as infinitely stiff, so the web crippling phenomena occurs under the loaded patch and not over the supports. The steel was modeled as an isotropic material using the von Mises yield criterion and the isotropic work hardening assumption. The cosine shape was used to model the geometrical imperfection of the web. Amplitude of 1 mm (0.04 in.) was imposed over the whole web plate for the parametric analyses. Since the level of the geometrical imperfection was

unknown, Granath conducted an imperfection sensitivity study. He considered different imperfection amplitudes ranging from 0.1 mm (0.004 in.) to 5.0 mm (0.20 in.). In his sensitivity analysis, he found little variation in the ultimate load capacity of the models. He also observed that the web deformed with the same shape as the chosen geometric imperfection. Based on his results, he concluded that the moment capacity of the flange does not have an influence in the web crippling capacity, while the flange stiffness does. Granath did not consider the web crippling phenomena over the supports in the study.

Tryland *et al.* (1999) studied the response of numerical simulations of steel beams under concentrated loading. The finite element code LS-DYNA was employed to perform this study. Three load cases were included in the study: concentrated forces applied to an unstiffened girder end, concentrated forces applied to the top flange, and opposite concentrated forces applied on both flanges. The concentrated loads were applied either at the midspan or at the end of the support. Shell elements were used to model the steel girders. The steel material was modeled as elastic-plastic with isotropic linear elasticity, von Mises yield criterion, and isotropic strain hardening. A bilinear stress-strain curve having a modulus of elasticity of 204 GPa (29,500 ksi), and a tangent modulus of 0.5 GPa (72.5 ksi) was used in the finite element analyses. Geometrical imperfections were introduced in the finite element models with an assumed imperfection pattern. The web distortion was modeled as a sine wave over its height, while a number of half sine waves were imposed along the plate girder. In the validation process of the finite element model, they observed that an element size of 20 mm (0.8 in.) was appropriate. Tryland *et al.* obtained good correlation for both the load-deflection curve and ultimate collapse load between the experiments and the finite element predictions. They reported that the error in the predicted ultimate strength was within 11%. They concluded that the geometrical imperfections imposed in the models govern the deformation mode, and therefore influence the response of the structural elements.

Two years later, Tryland *et al.* (2001) published another paper on the finite element modeling of beams under concentrated loads. At this time, the finite element simulations were performed using solid elements. An eight-node brick element from the

LS-DYNA code was used. The same structural steel properties and load cases as defined in the previous study were employed in this study. In the validation process, they found it necessary to use very small elements especially in the area beneath the compressive load. An element size of 3.5 mm (0.14 in.) was found appropriate for the steel girders. This element size is about 83% smaller than the element size obtained from the validation process in the previous study. Tryland *et al.* concluded that the correlation between the experimental and numerical results was quite good. They pointed out that this numerical simulation, which used solid elements, was very complicated and the computational time increased greatly compared to the previous study.

The most recent finite element study on webs under patch loading was performed by Graciano and Edlund (2002). The purpose of their study was to investigate the ultimate load behavior of longitudinally stiffened girder webs under patch loading by employing the finite element technique. The commercial finite element program ABAQUS was used to perform the nonlinear finite element analyses. Shell elements were used to model the web, flanges, and the longitudinal stiffeners. The steel was modeled as an elastic-plastic material with a stress-strain curve as defined in the Swedish code for steel construction. The modulus of elasticity was set to 210 GPa (30,500 ksi) and Poisson's ratio to 0.3. Graciano and Edlund (2002) reported that the two tested girders had different imperfection patterns. As shown in Figure 1.7 the imperfection patterns were similar to an S-shape for the first girder, and a C-shape for the second girder. In the finite element model, the girders were modeled with two opposite half wave shapes similar to an S-shape, and a half wave shape similar to a C-shape. The S-shape was modeled using cosine functions both in the transverse and longitudinal direction:

$$w_u = \frac{w_1}{4} \left[\cos\left(1 - \frac{2\pi x}{a}\right) \cos\left(1 - \frac{2\pi y}{h_w - z_1}\right) \right] \quad (1.7)$$

$$w_l = \frac{w_2}{4} \left[\cos\left(1 - \frac{2\pi x}{a}\right) \cos\left(1 - \frac{2\pi y}{z_1}\right) \right] \quad (1.8)$$

For the C-shape imperfection pattern, the cosine function was written as follows:

$$w = \frac{w_0}{4} \left[\cos\left(1 - \frac{2\pi x}{a}\right) \cos\left(1 - \frac{2\pi y}{h_w}\right) \right] \quad (1.9)$$

where:

w : Out-of-plane deformation, in.

a : Length of the web panel, in.

h_w : Web height, in.

x : Coordinate of the imperfection value in x-direction, in.

y : Coordinate of the imperfection value in y-direction, in.

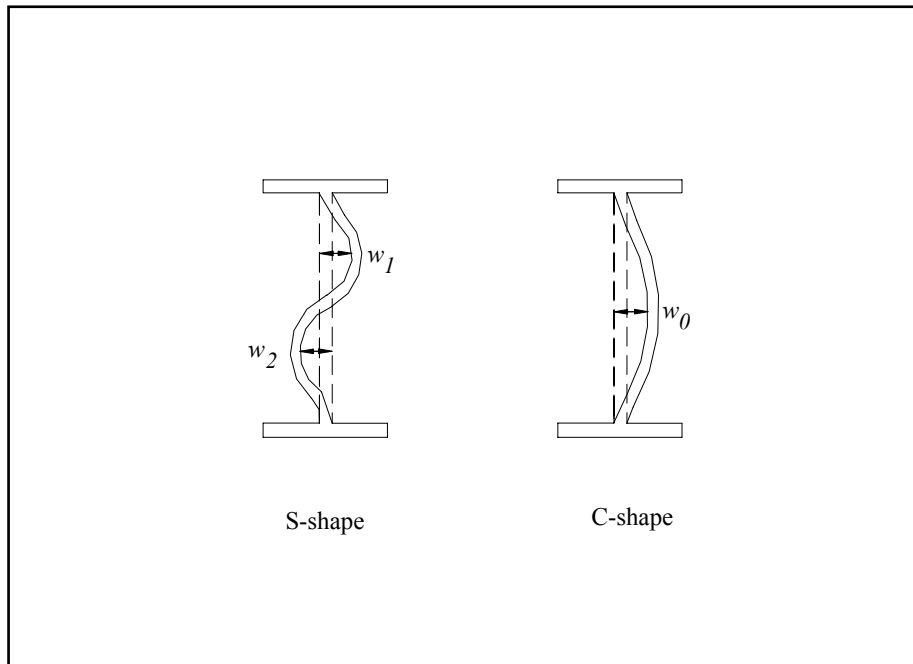


Figure 1.7 Cross-sectional web imperfections.

The measured experimental imperfections for the two tested girders were: $w_1 = 5.4$ mm. (0.21 in.), and $w_2 = 5$ mm (0.20 in.) for the first girder; and $w_0 = 9$ mm (0.35 in.) for the

second girder. Graciano and Edlund performed an imperfection sensitivity analysis for the model with the C-shape. They used amplitudes of 5.4 mm. (0.21 in.), and 9 mm (0.35 in.). The results of the sensitivity analysis showed that the difference in the ultimate failure load was not great. The difference in the ultimate load using these two different imperfection amplitudes was about 2%. A great difference in the ultimate failure load was found when a different imperfection shapes were used. They observed that for the same imperfection amplitude, a C-shape imperfection pattern carried approximately 7% more load than a S-shape. In their validation analyses, they obtained collapse load similar to the experiment for the girder with an S-shape imperfection pattern, while for the girder with a C-shape imperfection pattern the difference in the collapse load obtained from the finite element analysis and experimental test was approximately 9%. In both analyses, the correlation of the load-deflection curve between the experimental and finite element results was not good. The load-deflection behavior was similar but the experimental path was not closely followed.

Throughout these studies, it has been demonstrated that the finite element technique can be used to adequately predict the ultimate collapse load and the response mode shape of the web crippling over a beam support. However, it is important to observe that the characteristics of the models, i.e. geometrical imperfections, are not standard in the finite element method. In fact, this is a process of engineering judgment. Any finite element model has to be validated against the test data before relying on the finite element results.

1.3 Scope of the Research

This study further investigates the web crippling strength of W-shape steel beams at the supports for bearing-to-depth ratio greater than 0.2 on realistic span beams. The commercial finite element package, ANSYS version 6.0, was used to model and analyze the web crippling behavior of the beam sections. The numerical simulations consisted of two main stages: the validation stage and parametric stage. In the validation stage, models similar to beam sections experimentally tested by other authors were created. A

nonlinear finite element analysis was performed to determine the web crippling behavior of the models and to validate them against experimental results. In the parametric stage, the validated characteristics of the models were used to analytically determine the web crippling strength of the beam sections for different bearing-to-depth ratios on realistic span lengths. Finally, the results obtained from finite element analyses were compared to the predictions of the 1999 ASIC LRFD (AISC, 1999) design equation for end web crippling equation (K1-5b) to determine its accuracy.

1.4. Thesis Outline

This thesis presents a study conducted on the end web crippling strength of W-shape steel beams for bearing-to-depth ratio greater than 0.2 by employing the finite element technique. The results from previous studies conducted by other authors are compiled and presented in Chapter 2. These experimental results were used to validate the finite element models. This chapter also contains the description of the test configuration used in each study. In Chapter 3, descriptions of the finite element models developed in this study are presented. The finite element results are presented in Chapter 4. This chapter also presents a discussion of the behavior of the finite element model and a comparison between the 1999 AISC LRFD design equation for end web crippling (K1-5b) and the finite element predictions. A summary and the major conclusions of this study are presented in Chapter 5. Three appendices are included in this study. Appendix A, presents the procedure employed to create, analyze, and view the results of the nonlinear finite element model by using the ANSYS' Graphical User Interface. Additional finite element results are presented in Appendix B. Finally, Appendix C presents additional screened end web crippling data not included in Chapter 2.

CHAPTER 2

EXPERIMENTAL STUDIES AND RESULTS

2.1. General

This section describes the testing procedure and experimental results from the two most recent studies conducted to investigate the end web crippling behavior of hot-rolled steel beams. The two sets of experimental data are from Elgaaly and Salkar (1991), and Bryant (1993). Not all experimental results from Elgaaly and Salkar are valid to assess the end web crippling behavior of steel beams. Therefore, this study presents only the screened end web-crippling data. Those valid test results include eighteen tests of a total of twenty-seven tests from Elgaaly and Salkar, and all five tests from Bryant.

2.2. Elgaaly and Salkar

Elgaaly and Salkar (1991) published the results of a series of tests conducted at the University of Maine to study the behavior of webs under compressive loading. Among the data reported, there were two sets of tests conducted to study the web crippling behavior over a support. Hot-rolled beam sections ranging from W12 to W21 were used in their experimental studies. The first set of valid data comprised tests conducted on W12x14, W14x22, W16x31, W18x35, and W21x50 sections where the span length-to-depth ratio ranged from 1.58 to 1.77. Therefore, the shear span lengths were less than 3/4th of the depth of the beam section for all specimens in this series. The second set of valid data comprised of experimental tests conducted on W12x16 sections where the span length ranged from 3.0 ft to 4.0 ft. In this testing arrangement, the shear span length was greater than the depth of the beam. All test beams were simply supported, and loaded by a single concentrated load located at midspan. Tables 2.1 and 2.2 include a description of the test specimens for the first and second series, respectively. Table 2.3 the ultimate collapse load based on the test results and the 1999 AISC LRFD Specification web crippling equations are listed.

Table 2.1.

Summary of the geometric and material properties for the first set of tests conducted by Elgaaly and Salkar.

Test Designation *	Beam Section	Span (in.)	N (in.)	t_w (in.)	t_f (in.)	d (in.)	b_f (in.)	F_y (ksi)
1	W12x14	21.0	2.38	0.201	0.215	11.88	4.03	53.2
4	W14x22	24.0	2.76	0.237	0.329	13.81	5.12	54.4
7	W16x31	26.9	3.19	0.263	0.431	15.94	5.64	57.6
8	W16x31	26.9	4.92	0.300	0.432	15.88	5.52	51.3
10	W18x35	30.0	3.55	0.294	0.429	17.75	6.05	62.6
12	W21x50	33.1	4.19	0.362	0.525	20.94	6.62	62.8

* Numbering system as per Elgaaly and Salkar (1991)

Table 2.2.

Summary of the geometric and material properties for the second set of tests conducted by Elgaaly and Salkar.

Test Designation *	Beam Section	Span (in.)	N (in.)	t_w (in.)	t_f (in.)	d (in.)	b_f (in.)	F_y (ksi)
14	W12x16	36.0	2.40	0.220	0.265	11.99	3.99	46.5
15	W12X6	36.0	2.40	0.220	0.265	11.99	3.99	44.1
16	W12X6	36.0	3.00	0.220	0.265	11.99	3.99	44.3
17	W12X6	36.0	3.60	0.220	0.265	11.99	3.99	43.5
18	W12X6	36.0	3.60	0.220	0.265	11.99	3.99	45.9
19	W12X6	36.0	4.20	0.220	0.265	11.99	3.99	45.4
20	W12X6	36.0	4.80	0.220	0.265	11.99	3.99	44.2
21	W12X6	36.0	4.80	0.220	0.265	11.99	3.99	44.7
22	W12X6	42.0	5.40	0.220	0.265	11.99	3.99	52.3
24	W12X6	42.0	6.00	0.220	0.265	11.99	3.99	66.5
25	W12X6	48.0	6.59	0.220	0.265	11.99	3.99	49.6
27	W12X6	42.0	7.19	0.220	0.265	11.99	3.99	49.9

* Numbering system as per Elgaaly and Salkar (1991)

Table 2.3.

Summary of the screened web crippling strength results from experimental studies conducted by Elgaaly and Salkar.

Test Designation *	Beam Section	N/d	Experimental Failure Load, R_U (kips)	1999 AISC LRFD Specification, R_{AISC} (kips)	R_U / R_{AISC}
1	W12X14	0.200	28.25	31.96	0.8942
14	W12X16	0.200	36.52	35.81	1.020
15	W12X16	0.200	35.02	34.84	1.005
16	W12X16	0.250	43.52	38.59	1.128
17	W12X16	0.300	46.10	41.84	1.102
18	W12X16	0.300	44.98	42.98	1.046
19	W12X16	0.350	52.30	46.43	1.126
20	W12X16	0.400	50.60	49.43	1.024
21	W12X16	0.400	55.05	49.72	1.107
22	W12X16	0.450	68.00	57.74	1.178
24	W12X16	0.500	72.80	69.56	1.046
25	W12X16	0.550	68.25	63.93	1.068
27	W12X16	0.600	57.80	67.98	0.8503
4	W14X22	0.200	46.00	45.37	1.014
7	W16X31	0.200	67.50	58.77	1.148
8	W16X31	0.310	91.15	84.26	1.082
10	W18X35	0.200	73.25	75.30	0.9728
12	W21X50	0.200	127.50	114.26	1.116

* Numbering system as per Elgaaly and Salkar (1991)

Three sets of test data from this study were used to create and validate the finite element models; Test Nos. 3, 15, and 17. The validation results of these models are presented in Chapter 4.

2.3. Bryant

Bryant (1993) conducted various experimental tests at Virginia Polytechnic Institute and State University to evaluate the predictions of the 1993 AISC LRFD Specification web crippling equation (K1-5b) and his own web crippling formula. Five steel-concrete composite beams with W12, W14, and W16 sections were tested for web crippling failure at the support. Tables 2.4 and 2.5 present a summary of the geometric and material properties for the steel, and the concrete slab and shear studs, respectively. Two concentrated loads were symmetrically applied to the specimens with respect to the centerline of the beam section. Table 2.6 shows the location of the concentrated loads for each test. The ultimate collapse loads based on the test results and the 1999 AISC LRFD Specification web crippling equation predictions are given in Table 2.7.

The experimental data of the Test SC-2 from this study was used to create and validate the finite element model. The validation results of this model are also presented in Chapter 4.

Table 2.4.

Summary of the geometric and material properties for the steel beam of the tests conducted by Bryant

Test Designation *	Beam Section	Span (in.)	N (in.)	t_w (in.)	t_f (in.)	d (in.)	b_f (in.)	F_y (ksi)
SC-1	W16x26	408.0	3.50	0.260	0.336	15.81	5.44	60.6
SC-2	W14x22	228.0	3.50	0.228	0.338	13.75	4.69	60.9
SC-3	W14x22	192.0	3.50	0.228	0.338	13.75	4.69	60.9
SC-4	W12x16	66.00	2.50	0.201	0.287	11.97	4.00	56.9
SC-5	W12x16	54.00	2.50	0.201	0.287	11.97	4.00	56.9

* Steel-concrete composite beams.

Table 2.5.

Summary of the geometric and material properties for the concrete slab and shear studs of the tests conducted by Bryant

Test Designation *	Beam Section	b_s^{**} (in.)	t_s^+ (in.)	f'_c (psi)	N_s	d_s^{++} (in.)	h_s^{+++} (in.)	I_{eff} (in ⁴)
SC-1	W16x26	80.0	5.00	5300	30	0.75	3.50	1070
SC-2	W14x22	80.0	5.00	6300	20	0.75	3.50	668
SC-3	W14x22	80.0	5.00	6300	20	0.75	3.50	668

* Steel-concrete composite beams.

** Width of the concrete

+ Thickness of the concrete slab

++ Diameter of the shear studs

+++ Height of the shear studs

Table 2.6.

Position and maximum end reaction for each load location for the tests conducted by Bryant (1993).

Test Designation *	Loading Sequence	Distance from the Support Centerline and the Point Load (in.)	Maximum End Reaction (kips)
SC-1	1	86.00	39.90
	2	62.00	55.50
	3	50.00	68.00
	4	44.00	68.00
SC-2	1	48.00	44.00
	2	36.00	53.00
SC-3	1	36.00	48.00
SC-4	1	15.50	33.88
SC-5	1	22.00	33.43

* Steel-concrete composite beams.

Table 2.7.

Summary of the screened web crippling strength results from experimental studies conducted by Bryant.

Test Designation *	Beam Section	N/d	Experimental Failure Load, R_U (kips)	1999 AISC LRFD Specification, R_{AISC} (kips)	R_U / R_{AISC}
SC-1	W16x26	0.221	68.00	59.66	1.140
SC-2	W14X2	0.255	53.00	48.84	1.085
SC-3	W14X2	0.255	48.00	48.81	0.9834
SC-4	W12X6	0.209	33.88	33.98	0.9970
SC-5	W12X6	0.209	33.43	33.98	0.9838

* Steel-concrete composite beams.

CHAPTER 3

FINITE ELEMENT MODEL DETAILS

3.1. General

This chapter describes the details of the finite element models created and analyzed in this study. In general, the finite element models consist of simple supported steel beams, where the bottom flange of the beam section is constrained at the ends by a bearing block. The bearing block is modeled at one end of the beam by restricting all six degrees of freedom associated with translational and rotational movements of the applicable nodes. The opposite end is modeled as a roller support by restricting only vertical and traverse translations of the far end nodes. Lateral transverse movement of the top flange is restricted by applying constraints in the horizontal direction on the nodes. The following sections give a detailed description of the finite element models developed using the commercial software ANSYS version 6.0.

3.2. Mesh Elements

The process of subdividing a continuum into small elements is not standard in the finite element method. In fact, this process is an exercise of engineering judgment. The factors considered in this process are number, shape, size and type of elements, as well as, the element aspect ratio, which is defined as the ratio of the largest dimension of the element to its smallest dimension.

A shell-type element was used to model the steel beam because of its capability for out-of-plane deformations. Shell elements were also used to model the concrete slab for the steel-concrete composite models. ANSYS *SHELL143* and *SHELL181* elements were only considered in this study. Both shell elements are well suited to analyze thin to moderately thick structures for nonlinear behavior. Table 3.1 gives a brief description, taken from the ANSYS user's manual, of the capabilities of both elements.

Table 3.1.

Description of the Capabilities of Elements *SHELL143* and *SHELL181*.

Element Type	Capabilities *
SHELL143	<p>Suited to model nonlinear, flat or warped, thin to moderately thick shell structures. The element has four nodes with six degrees of freedom at each node: translations in the nodal x, y, and z directions and rotations about the nodal x, y, and z-axes.</p> <p>The deformation shapes are linear in both in-plane directions. For the out-of-plane motion, it uses a mixed interpolation of tensorial components.</p> <p>The element has plasticity, stress stiffening, large deflection, and small strain capabilities.</p>
SHELL181	<p>Suitable for analyzing thin to moderately thick shell structures. The element has four nodes with six degrees of freedom at each node: translations in the x, y, and z directions, and rotations about the x, y, and z-axes.</p> <p>Suited for linear, large rotation, and/or large strain nonlinear applications.</p>

* Taken from the ANSYS user's manual

Beam elements were used to model the shear studs of the composite beam models. The element *BEAM4* was selected for this purpose. This element is a uniaxial element with tension, compression, torsion, and bending capabilities. The element has six degrees of freedom at each node: translations in the nodal x, y, and z directions and rotations about the nodal x, y, and z-axes. Stress stiffening and large deflection capabilities are included.

Mapped meshing was used to subdivide the continuum in small elements. This option was preferred over free meshing because it restricts the element shape and the pattern of the mesh providing a better control of the mesh density, which is important when performing a convergence analysis. Since the mapped meshing option was chosen, either only rectangular or only triangular elements could be used. Rectangular elements

were selected to define the small elements because of their advantages over the triangular elements in obtaining better engineering results.

As a rule of thumb among the analysts of the finite element method, an element aspect ratio less than 2 is considered necessary. In fact, better results are obtained if the aspect ratio is closer to unity. The element aspect ratio used to model the beams with non-composite action was between 1 and 1.5 depending on the size of the model. Actually, in the validation models, an element aspect ratio equal to 1 was used because the modeled experimental tests were performed on short span beams. The models created to perform the parametric analysis used an element aspect ratio of 1.5 in order to minimize the running time and reduce computer memory. For those models with composite action, an element aspect ratio equal to 2 was used.

The number and size of the elements used to perform the analysis were determined by performing a convergence analysis. The element sizes considered in this study were 0.75, 1.0, 1.25, and 2.0 in. In the next chapter, the results of the convergence analysis are presented.

3.3. Material Properties

The behavior of any engineering material is nonlinear. However, in many engineering applications, it is practical and convenient to assume linear behavior. On the other hand, there are some applications that required nonlinear analysis to better assess the response and capacity of the structural components. Both cases were considered in this study when defining the properties of the structural components of the models. The shear studs and the concrete slab of the steel-concrete composite models were modeled as a linear elastic material since their behavior does not influence the ultimate load of the webs. The beam sections were modeled as a nonlinear material since the web material will encounter post-yielding and large deformations behavior, as well as buckling deformations.

Structural nonlinearities of the steel beams modeled in this study were both geometric and material. Geometric nonlinearity is characterized by large displacements or large rotations. The change in geometric configuration causes the structure to respond nonlinearly since the stiffness changes. The ANSYS software activates the large deflection effects when the *NLGEOM,ON* option is used. Nonlinear stress-strain relationships are also a common cause of nonlinear structural behavior. This phenomenon is defined as a material nonlinearity. The *Bilinear Isotropic Hardening (BISO)* option was used to define the plasticity behavior of the steel material. As shown in the Figure 3.1, the elastic-plastic stress-strain curve is characterized by a linear relationship up to a level known as the proportional limit, σ_y . Then, the material yield and the slope of the stress-strain relationship become flatter than the initial slope. Because there is usually little difference between the yield point and the proportional limit, the ANSYS software assumes that these two points are coincident in plasticity analysis. The use of *Bilinear Isotropic Hardening (BISO)* option assumes that the total stress range is equal to twice the yield stress. It also uses the von Mises yield criteria coupled with an isotropic work hardening assumption. This option is often preferred for large strain analyses. Stress Stiffness was also used in the nonlinear analysis to account for buckling or bifurcation behavior of the web panel. This option was activated using the *SSTIFF, ON* option.

A modulus of elasticity (E) of 29,000 ksi, a Poisson's ratio (μ) of 0.3, a tangent modulus (E_t) of 2,900 ksi, and a specific weight density of 0.000284 kips/in³ were used as the material properties of steel for the validation and analysis models. The yield stress used in the validation process was equal to the yield stress reported by each author. The yield stress for the analysis models was set to 50 ksi except for the steel-concrete composite models where the actual yield stress was used. Those yield stress values are found in Chapter 2.

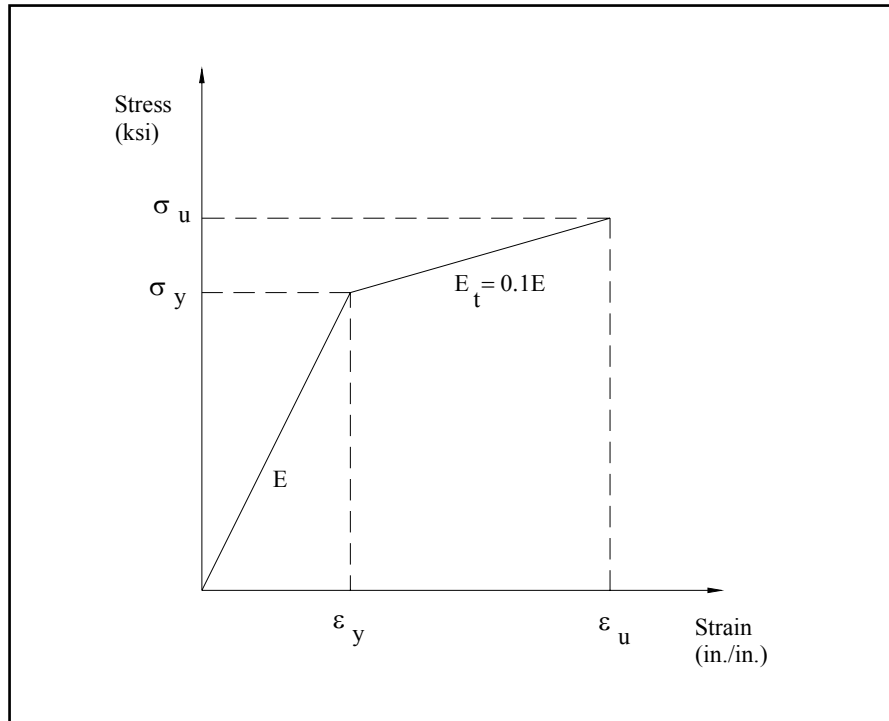


Figure 3.1 Stress-strain relationship defined in the finite element analyses.

The concrete slab and the shear studs were modeled as linear elastic material. Since the structural behavior of these components does not have an effect on the web crippling strength of the steel beams, only their elastic properties were used. The shear studs were defined with a modulus of elasticity of 29,000 ksi, and a Poisson's ratio of 0.3. The modulus of elasticity and the weight density of the concrete slab were taken as 6,300 ksi and 0.000121 kips/in³, respectively. This weight density value was different than the actual value because the effective width of the concrete slab of the specimen tested by Bryant was used in the models. Therefore, it was necessary to compute an equivalent weight density value to obtain the actual effect of the concrete slab.

3.4. Boundary Conditions

Constraints in the model can be defined on the *keypoints*, which are the points that define the geometry of the section, or on the nodes of the meshed section. Three types of supports were modeled in the finite element model by restraining several specific nodes.

The bearing block was defined by restraining all degrees of freedom (translations in the x, y, and z directions, and rotations about the x, y, and z-axes) on those nodes located at the bottom flange of the beam section. Experimentally, the steel beam is connected to the bearing block using bolts. The bottom flange-to-bearing block connection is overdesigned so that no failure due to the connection occurs during the test. Although some rotation or some settlement may occur, depending on how many bolts are attached, it is appropriate to neglect those effects in the model. No experimental data was found to validate these assumptions in the finite element model. Figure 3.2 shows the flange-to-bearing connection in the finite element model. The opposite end of the beam was modeled as a roller support. The far end nodes were restrained against translation in the vertical in-plane and horizontal out-of-plane directions, while all rotations and the longitudinal translation were left unrestrained. Lateral buckling was prevented in the model by restraining out-of-plane movement of all nodes at the top flange of the section. Those models that considered composite action were prevented from lateral movements by restraining the longitudinal edge nodes of the concrete slab. The lateral restraints for the non-composite model can be seen in the Figure 3.2, while Figure 3.3 shows the composite model with its boundary conditions.

3.5. Loading

The loading condition employed to study the web crippling phenomenon over the support is compressive in-plane loads applied at the top flange and centered on the web of the test beam. The perfectly in-plane loads are applied at the top flange of the beam through a loading pad. The area of the loading pad is small enough to assume that a concentrated load is being applied. In the ANSYS program, the load can be applied to the finite element model using solid-model loads or finite-element loads. The solid-loads are applied on the *keypoints*, while the finite-element loads are applied to the nodes of the meshed section. If the solid-model loads are used to load the finite element model, then the program automatically transfers them to the nodes and elements at the beginning of solution. In this study, the loads were applied to the finite element model by using finite-element loads to avoid certain problems which can occur when using solid-model loads.

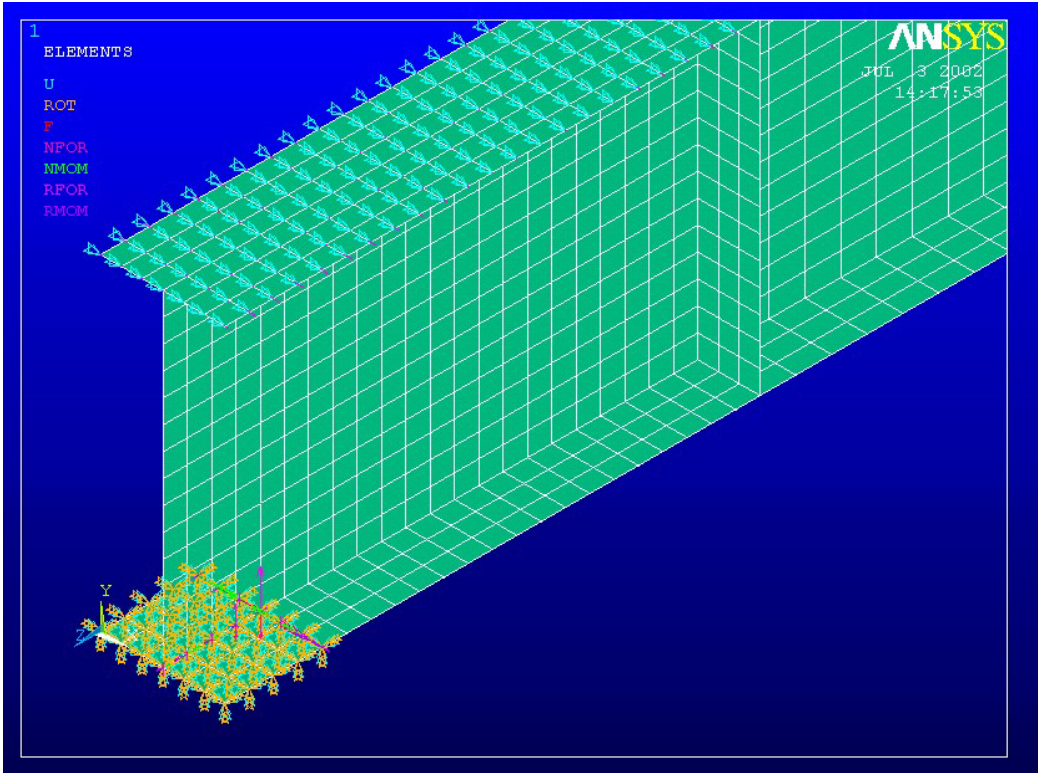


Figure 3.2 Flange-to-bearing connection in the finite element analyses.

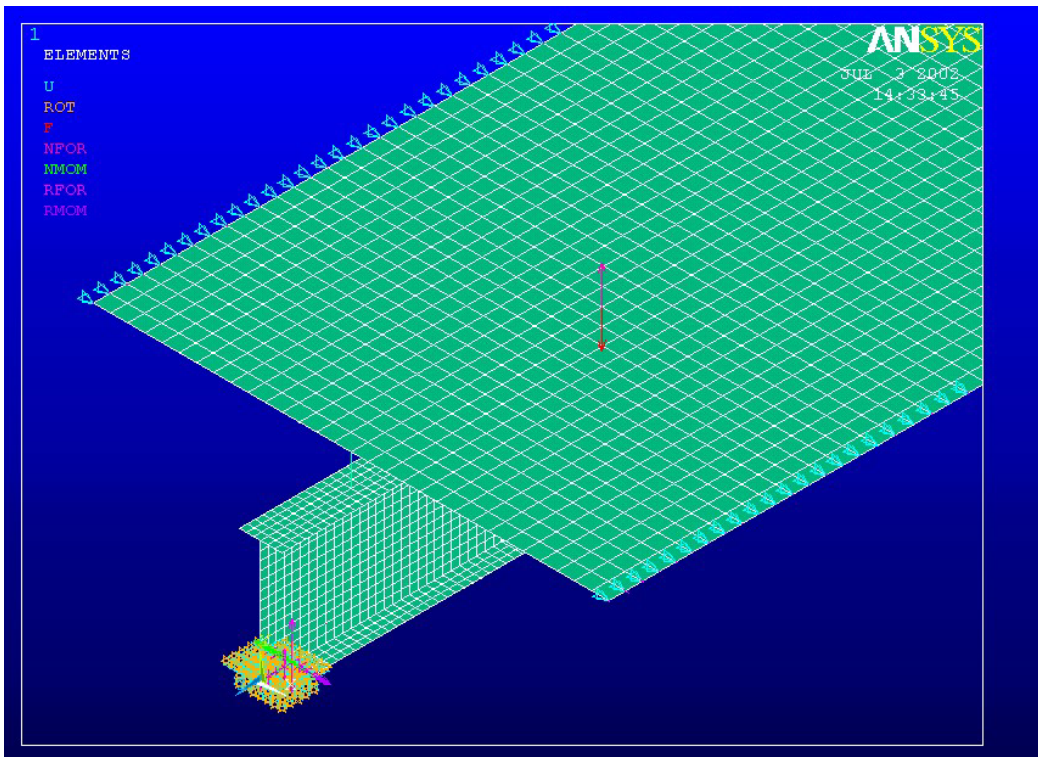


Figure 3.3 Restraints in the composite models as defined in the finite element analyses.

In some finite element applications, it is convenient to apply the load to a series of nearby nodes such that singularity is avoided. However, smaller sized elements are required if a concentrated load is to be so modeled. The loads, in this study, were applied to a single node instead. Stiffeners were used, similar to the experimental tests, to reinforce the web. In this manner, singularity was not encountered in the analysis.

A series of substeps were used to define the loading rate in the finite element model. When using multiple substeps, it is important to achieve a balance between accuracy and economy. More substeps usually result in better accuracy, but at a cost of increased run time and computer memory. Unless otherwise specified, the load was applied to the finite element model with increments of 5 kips, and until the steel material approached the yield point, at which point the load increments were reduced to 2 kips. This loading protocol was found to be sufficient to model the actual test load-response curve and for convergence.

3.6. Geometric Imperfections

The web crippling phenomena cannot be modeled in the finite element method unless small out-of-plane deformations, necessary to initiate the buckling response, are imposed in the web of the beam section. Most of the previous finite element studies used either a half sine or a half cosine shape to define the geometric imperfections that initiate the buckling response. Since the half cosine shape has some similarity to the web crippling failure mode, it is preferred over the half sine shape. As shown in Figure 3.4, the web of the beam section was given a half cosine shape in the transverse direction of the web with a maximum amplitude at mid-depth and a half cosine shape in the longitudinal direction with a maximum plateau at a distance L_0 from the end of the beam section. Figure 3.5 shows the finite element model with its imperfection pattern.

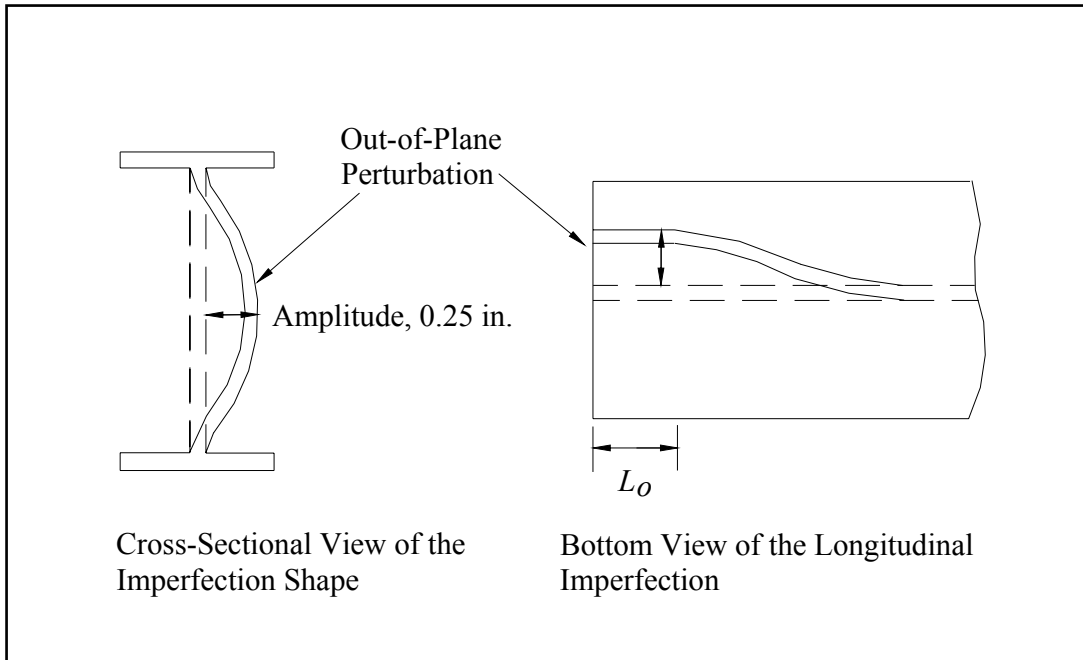


Figure 3.4 Assumed web imperfection.

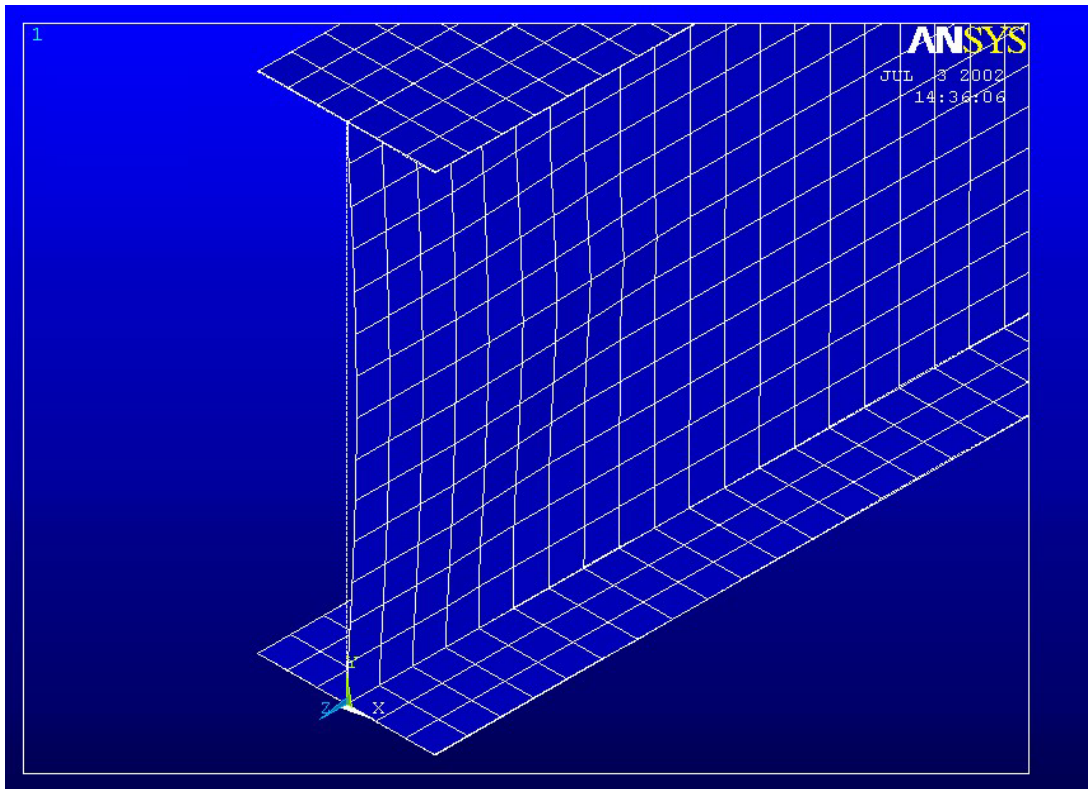


Figure 3.5 View of the geometrical imperfection pattern in the finite element model.

The following simple equation was developed to define the geometric imperfection pattern in the transverse direction of the web.

$$I_o = A \cos(\lambda H_y) \quad (3.1)$$

where,

A : Amplitude, in.

I_o : Out-of-plane perturbation in the plateau region, in.

λ : Variable depending on the depth of the web.

H_y : Coordinate of the imperfection value in the transverse direction of the web measured from the mid-depth of the beam section, in.

The equation that define the geometric imperfection pattern in the longitudinal direction of the web is:

$$I = I_o \cos(\lambda H_x) \quad (3.2)$$

where,

I : Out-of-plane perturbation, in.

I_o : Out-of-plane perturbation in the plateau region, in.

λ : Variable depending on the depth of the web.

H_x : Coordinate of the imperfection value in the longitudinal direction of the web measured from a distance L_o from the end of the beam section, in.

The corresponding λ -and L_o -values for each beam section evaluated in this study are found in the Table 3.2. The length of the plateau, L_o , was taken as 0.2 times the section depth.

Table 3.2.

Corresponding λ -and L_o -values for each W section.

Model Designation Series	Beam Section	λ	L_o (in.)
FEA-14x	W12x16	0.268	2.40
FEA-15x	W12x16	0.268	2.40
FEA-4x	W14x22	0.233	2.76
FEA-SC-2x	W14x22*	0.234	2.63
FEA-7x	W16x31	0.203	3.00

* Steel-concrete composite design

3.7. Solution Options

The basic way to do nonlinear analysis in ANSYS is to use Newton-Raphson iteration and many default settings. However, to assure that the analysis will closely follow the structure's load-response curve, several solution options have to be specified. Such options include the arc-length method as shown in Figure 3.6. This method causes the Newton-Raphson equilibrium iterations to converge along an arc, often preventing divergence. The arc-length maximum multiplier, *MAXARC*, was set to 1.0, while the arc-length minimum multiplier, *MINARC*, was set to 0.0001. It was found that these values were sufficient after several trials.

Another solution option available in the ANSYS program is the bisection option. ANSYS activates the bisection option if the convergence criteria have not been satisfied within the number of limiting equilibrium iteration equations, which was set to 25 equations in the finite element analyses. This feature cuts a time step size in half whenever equilibrium iterations fail to converge and automatically restarts from the last converged substep. If the halved time step again fails to converge, bisection will again cut the time step size and restart, continuing the process until convergence is achieved or until the minimum time step size is reached.

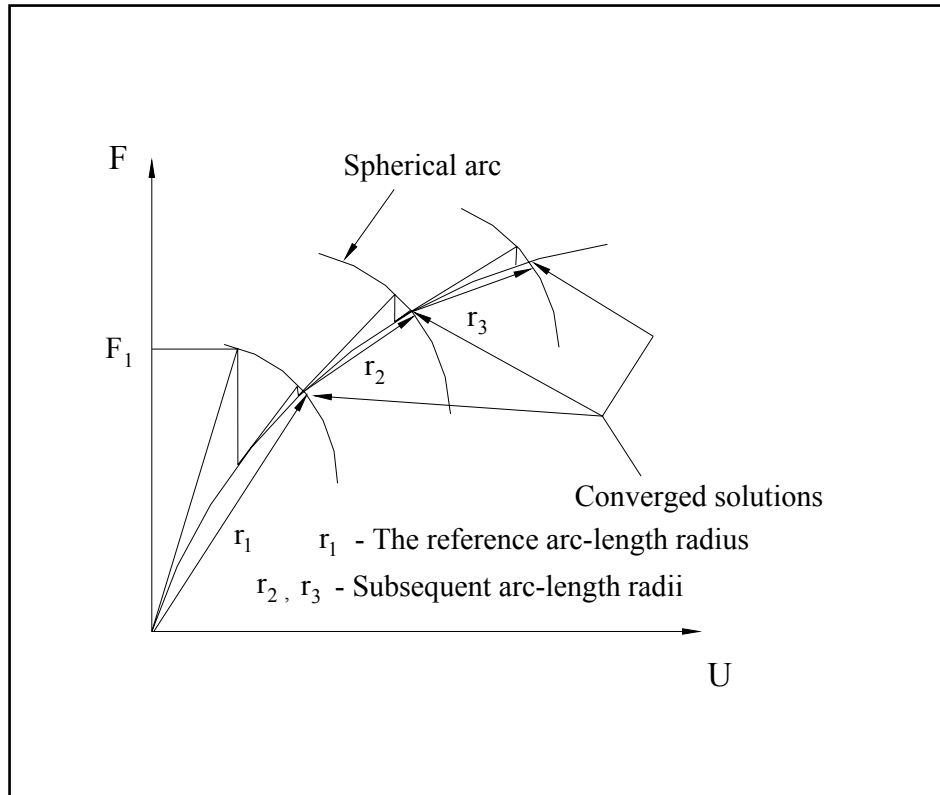


Figure 3.6 Newton-Raphson interaction coupled with arc-length method.

The *Sparse Direct Solver* (direct elimination solver) was used in this study. This solver was found to execute very well while doing nonlinear finite element analyses, especially with large model of shell elements. Although the geometry of the section and the loading conditions are symmetrical about midspan, no symmetry was considered in the model since the web crippling response is not symmetrical.

CHAPTER 4

FINITE ELEMENT RESULTS, COMPARISONS AND DISCUSSION

4.1 General

The numerical simulations consisted of two main stages, the validation and analysis stage. The first stage of this study consisted of validating the characteristics of the finite element models against experimental data. The experimental data from Elgaaly and Salkar (1991), and Bryant (1993) presented in Chapter 2 were used for this purpose. Finite element models of W12x16, W14x22, and W16x31 sections as tested by Elgaaly and Salkar were created and validated. An additional finite element model of the W14x22 section using steel-concrete composite action as tested by Bryant was also created and validated. The second stage of this study was a parametric analysis using the FEA models that satisfactorily predicted the respective experimental failure load. The bearing-to-depth ratio was gradually increased to investigate the web crippling strength of the steel beams.

Each finite element model was designated as FEA-Nx, where: FEA stands for finite element analysis; N is the number designation used by each author; and x represents the analysis sequence of a particular model. The commercial finite element package ANSYS 6.0 was used to create and analyze the beam models. A detailed description of the procedure employed to create and analyze the nonlinear finite element model by using the ANSYS' Graphical User Interface is presented in the Appendix A. The results of the validation analyses and the parametric analyses for each finite element model are presented below.

4.2 Sensitivity Analysis

4.2.1 Type of Shell Element

Elements *SHELL143* and *SHELL181*, from the ANSYS Library of Elements, were used in this study. These shell elements were selected because they are well suited to analyze thin to moderately thick plate structures that encounter nonlinear behavior. Figure 4.1 shows the behavior of the model FEA-15a using each type of element. As shown in the Figure, *SHELL181* converged to the experimental failure load, while element *SHELL143* failed to converge. Furthermore, the web crippling behavior was not developed when *SHELL143* was used. Instead, the model failed by flange bending. Although, web imperfection was imposed to both models, only *SHELL181* developed the web crippling failure mode. Because *SHELL181* predicted the experimental failure load and web crippling mode, this shell-type element was used in the remaining of the study.

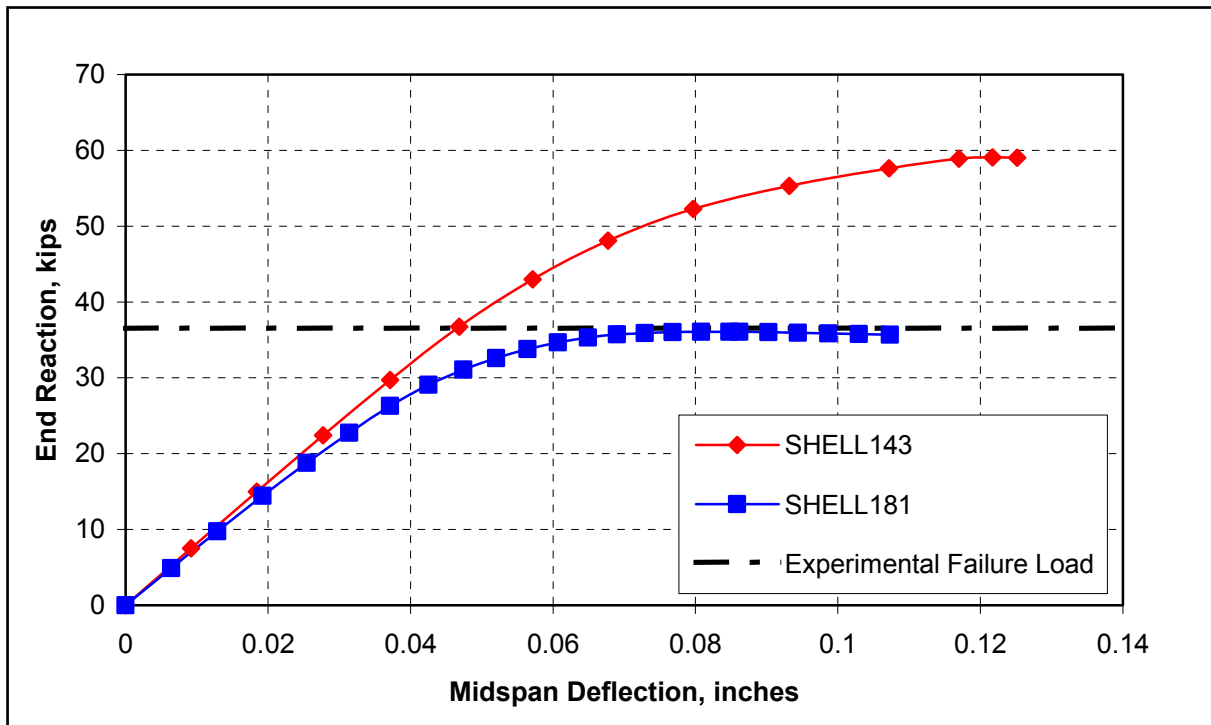


Figure 4.1 Behavior of the model FEA-15a with different shell-type elements.

4.2.2 Imperfection Size Sensitivity

The sensitivity of the web crippling strength by using different imperfection amplitudes was studied to determine the amplitude to be used in the analyses. As mentioned earlier, the web of the beam section was given a half cosine shape in the transverse and longitudinal directions of the web with maximum amplitude over the bearing support. Web imperfection amplitudes of 0.0 in. (perfectly straight web), 0.10 in., 0.20 in., 0.25 in., and 0.30 in. were evaluated with an initially assumed element size of 1.0 in. The resulting load-deflection curve was used to compare the response of the model with different imperfection sizes.

Figures 4.2 and 4.3 show the behavior of the web crippling strength for different imperfection amplitudes of models FEA-14a and FEA-4a, respectively. As expected, the web did not cripple when no imperfection amplitude was imposed to the web. This phenomenon occurs in numerical simulations because the loading on the structure is perfectly in-plane. As result, the out-of-plane deflections needed to begin the buckling response will not develop. It can be seen in Figure 4.2 that the tested failure load of 36.52 kips was well predicted by imperfection amplitudes of 0.20 in. and 0.25 in. FEA-14a carried maximum loads of 36.74 kips and 36.07 kips when imperfection amplitudes of 0.20 in. and 0.25 in. were imposed to the web, respectively. For the model FEA-4a, imperfection amplitudes of 0.25 in. and 0.30 in. accurately predicted the experimental failure load. As shown in Table 4.1, the FEM load-to-test load ratio, R_{FEA}/R_U , for this model was 1.005 and 0.9887 for imperfection amplitudes of 0.25 in. and 0.30 in., respectively. Concluding, it can be seen that an imperfection amplitude of 0.25 in. better predicts the experimental failure load in both finite element models. Therefore, this imperfection amplitude was used throughout the parametric analysis.

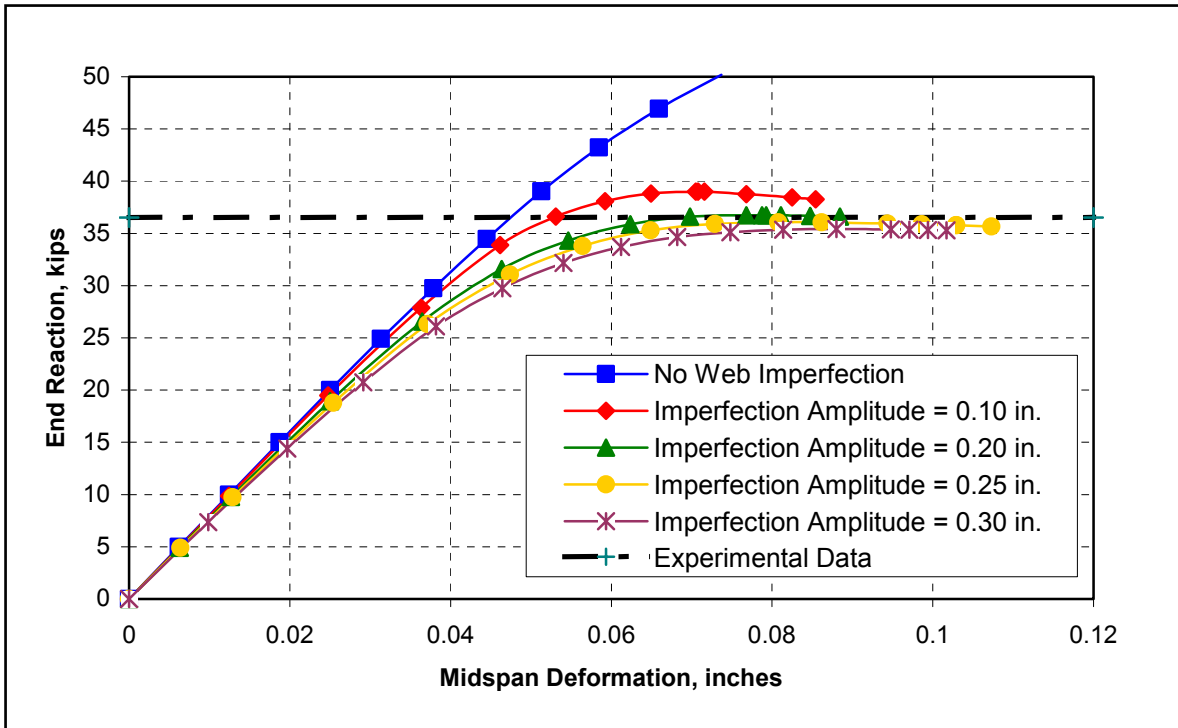


Figure 4.2 Web imperfection sensitivity for the model FEA-14a.

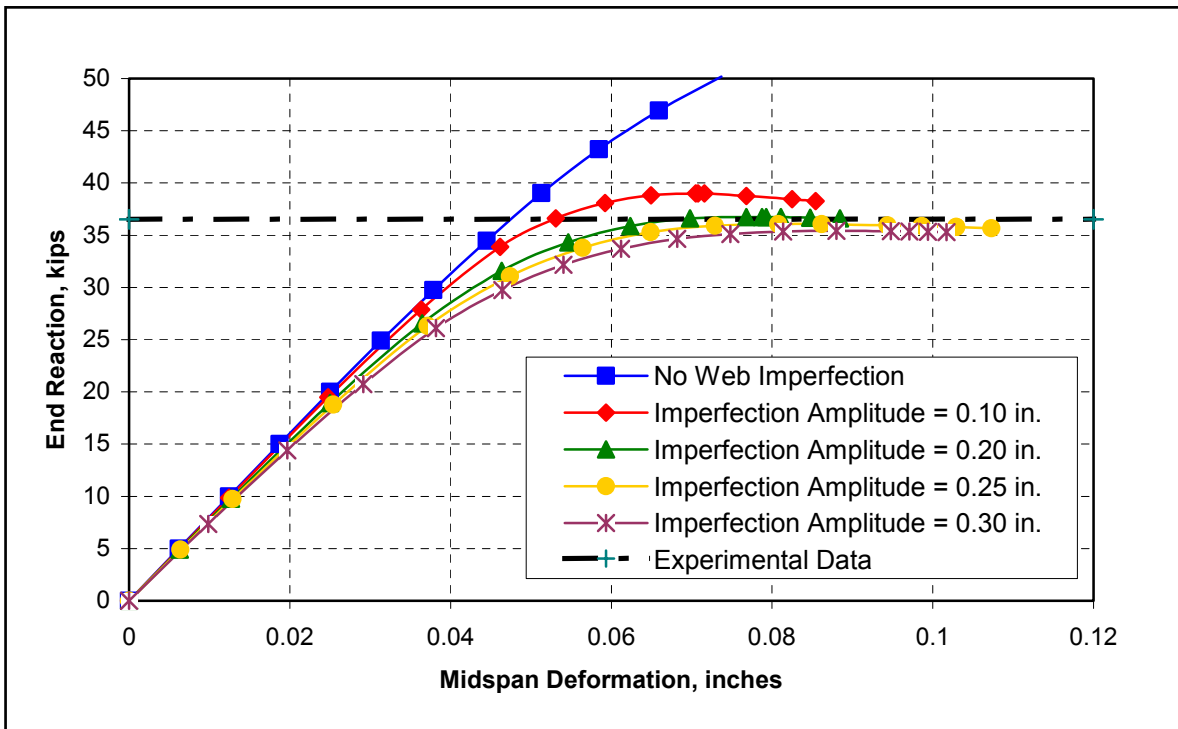


Figure 4.3 Web imperfection sensitivity for the model FEA-4a.

Table 4.1.

Summary of the imperfection sensitivity results for the models FEA-14a and FEA-4a.

Test Designation	Beam Section	Imperfection Amplitude (in.)	FEM Failure Load, R_{FEM} (kips)	Experimental Failure Load, R_U (kips)	R_{FEM} / R_U
FEA-14a	W12x16	0.10	39.01	36.52	1.07
		0.20	36.74	36.52	1.01
		0.25	36.07	36.52	0.988
		0.30	35.42	36.52	0.970
FEA-4a	W14x22	0.10	49.45	46.00	1.08
		0.20	49.99	46.00	1.02
		0.25	46.24	46.00	1.01
		0.30	45.48	46.00	0.989

4.2.3 Element Size Sensitivity

An element size sensitivity analysis was also performed to establish the mesh density to be used throughout the analyses. Element sizes of 0.75 in., 1.0 in. (initially assumed), 1.25 in., and 2.0 in. were considered. Since web crippling is investigated in this study, the variation of the out-of-plate deformation of the web under the support was the parameter used to study the sensitivity of web crippling strength by using different element sizes. Figures 4.4 and 4.5 present the sensitivity of the models FEA-14a and FEA-4a for different element sizes. It can be seen that there is little variation in the out-of-plane deformation of the web when using element sizes of 0.75 in., 1.0 in., and 1.25 in. The paths of the load-deformation curves were quite similar, and the experimental failure load was well predicted by all three element sizes.

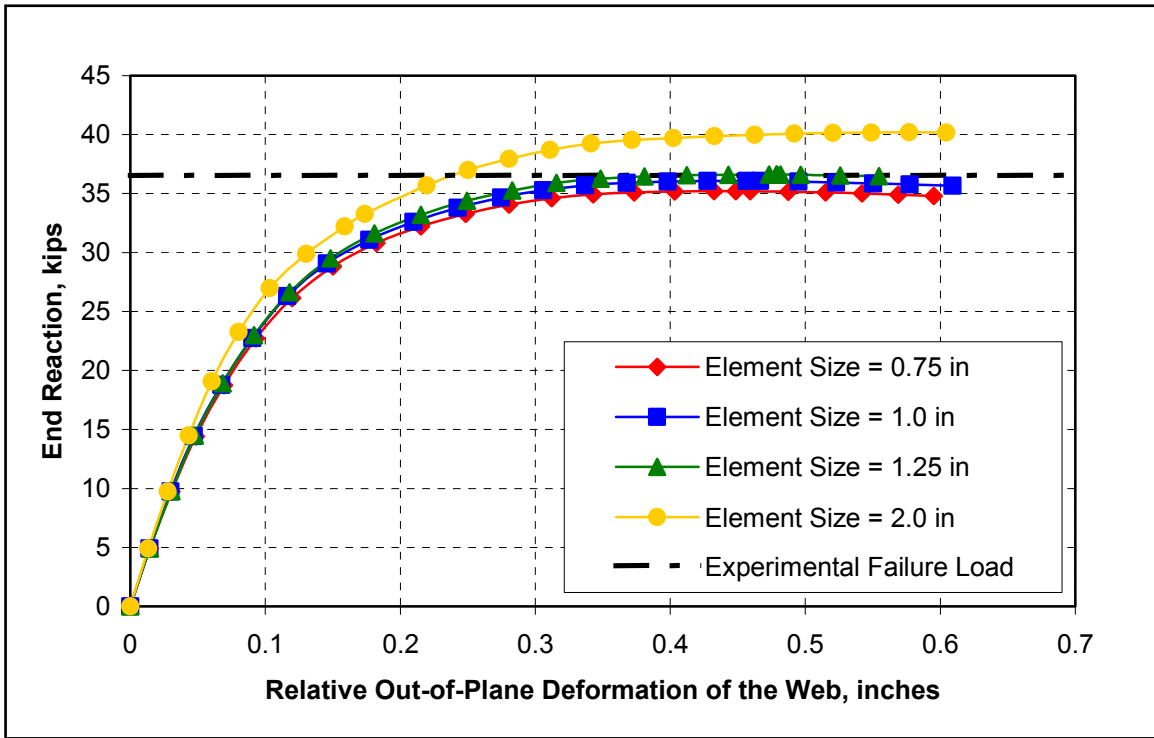


Figure 4.4 Element size sensitivity for the model FEA-14a.

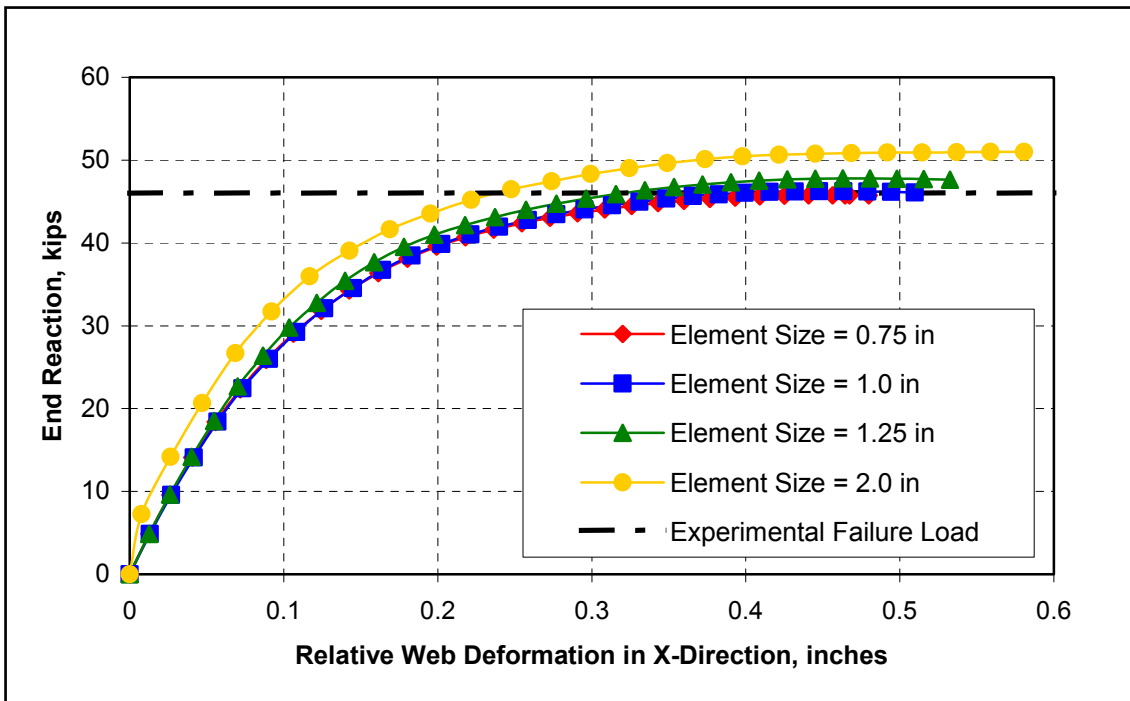


Figure 4.5 Element size sensitivity for the model FEA-4a.

For a better comparison of the element sensitivity results for the models FEA-14a and FEA-4a, Table 4.2 presents the FEM load-to-test load ratio for each element size. It can be easily seen that element sizes of 1.0 in. and 1.25 in. accurately predict the ultimate collapse load for the model FEA-14a, while for the model FEA-4a element sizes of 0.75 in. and 1.0 in. give good correlation between the FEM and experimental failure loads. The differential values between the finite element and experimental failure loads were less than 1.25% in both cases. Thus it has been demonstrated that an element size of 1.0 in., which was initially assumed, provides good correlation between the FEM and experimental failure load. Therefore, this element size was used to subdivide the components in all of the following parametric analyses.

Table 4.2.

Summary of the element sensitivity results for the models FEA-14a and FEA-4a.

Test Designation	Beam Section	Element Size (in.)	FEM Failure Load, R_{FEM} (kips)	Experimental Failure Load, R_U (kips)	R_{FEM} / R_U
FEA-14a	W12x16	0.75	35.21	36.52	0.964
		1.00	36.07	36.52	0.988
		1.25	36.60	36.52	1.00
		36.52	41.19	36.52	1.28
FEA-4a	W14x22	0.75	45.76	46.00	0.995
		1.00	46.24	46.00	1.01
		1.25	47.79	46.00	1.04
		2.00	50.99	46.00	1.11

4.3 Finite Element Results and Comparisons

4.3.1 Validation Analysis

Four non-composite beam models and one composite beam model were validated against experimental data. The non-composite models consisted of simply supported beams loaded with a single concentrated load located at midspan. Therefore, each support reaction takes one-half of the applied load. The span length for these specimens ranged from 2.0 ft to 3.0 ft. The fifth validation model consisted of a simply supported steel-concrete composite beam with span length of 19.0 ft. This specimen was loaded with two single concentrated loads located 36 in. from the centerline of the supports. Since the loading was symmetrical about midspan of the beam section, the same load had to be resisted at each support. For a detailed description of the experimental specimens refer to Chapter 2. Table 4.3 presents the designation system used for the validation models and its relation with the experimental data.

Table 4.3.

Designation of each validation model and its relation with experimental data.

Model Designation	Test Designation *	Beam Section	Bearing Length, N (in.)
FEA-14a	14	W12x16	2.40
FEA-15a	15	W12x16	2.40
FEA-4a	4	W14x22	2.76
FEA-7a	7	W16x31	3.19
FEA-SC-2a	SC-2	W14x22 **	3.50

* Numbering system as reported by Elgaaly and Salkar (1991) and Bryant (1993)

** Steel-concrete composite beam

4.3.1.1 Non-Composite Models

Figures 4.6 to 4.10 present the load-deflection curves from basic beam theory, stiffness analysis with and without shear deformations considered, and finite element analysis as well as the experimental failure load for the non-composite sections. The stiffness method analyses were made using the commercial software RISA 3D (RISA 3D User's Manual, 2001). It can be easily seen that the deflection behavior of the stiffness analysis models was affected by shear deformations, where the span length for those specimens was less than 3 ft. Good agreement was found between the load-deflection curves obtained from the FEM analysis and the curve obtained from RISA 3D with shear deformations considered. In addition, the FEM validation model closely predicted the experimental failure load. The FEM failure load for the model FEA-14a was 36.07 kips, while the experimental failure load was 36.52 kips. An additional finite element model using a W12x16 section was also validated. This validation model is designated as FEA-15a. As seen in the Figure 4.7 the finite element model accurately predicts the experimental collapse load. The difference between the FEM and experimental failure loads was just 0.15%.

The validation results for the finite element model FEA-4a is shown in Figure 4.8. Good correlation was also found between the finite element and experimental failure loads. The FEM failure load was 46.24 kips against 46.00 kips from experimental data, representing 0.52% difference.

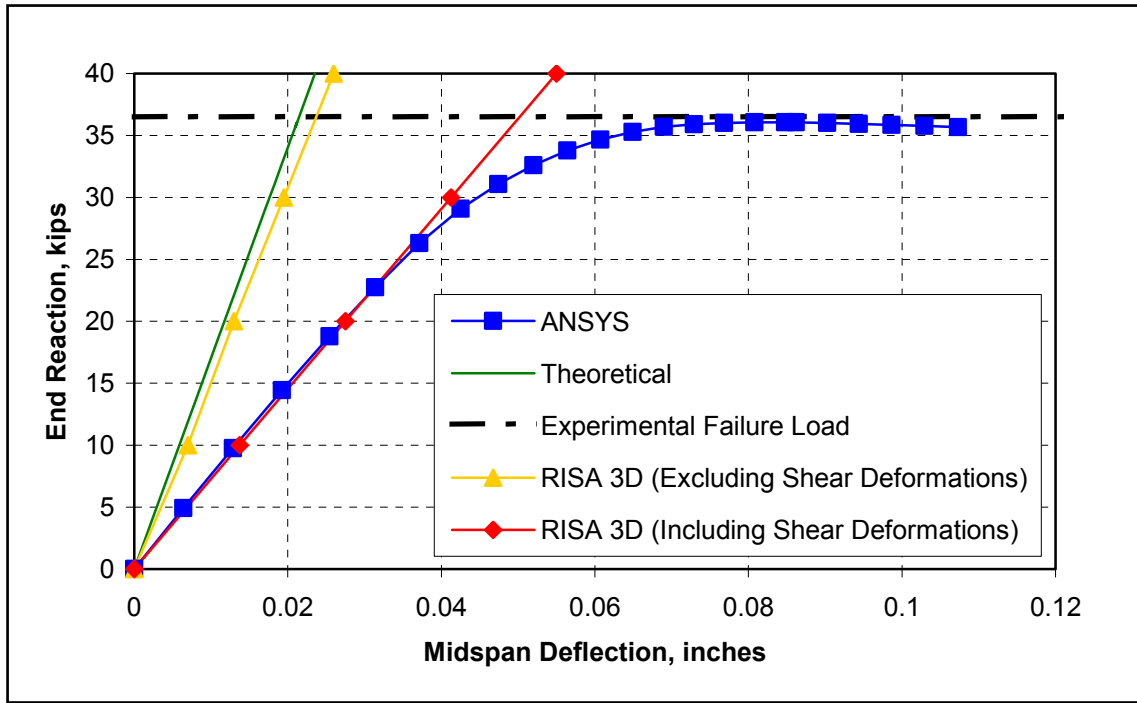


Figure 4.6 Load-deflection response of the model FEA-14a.

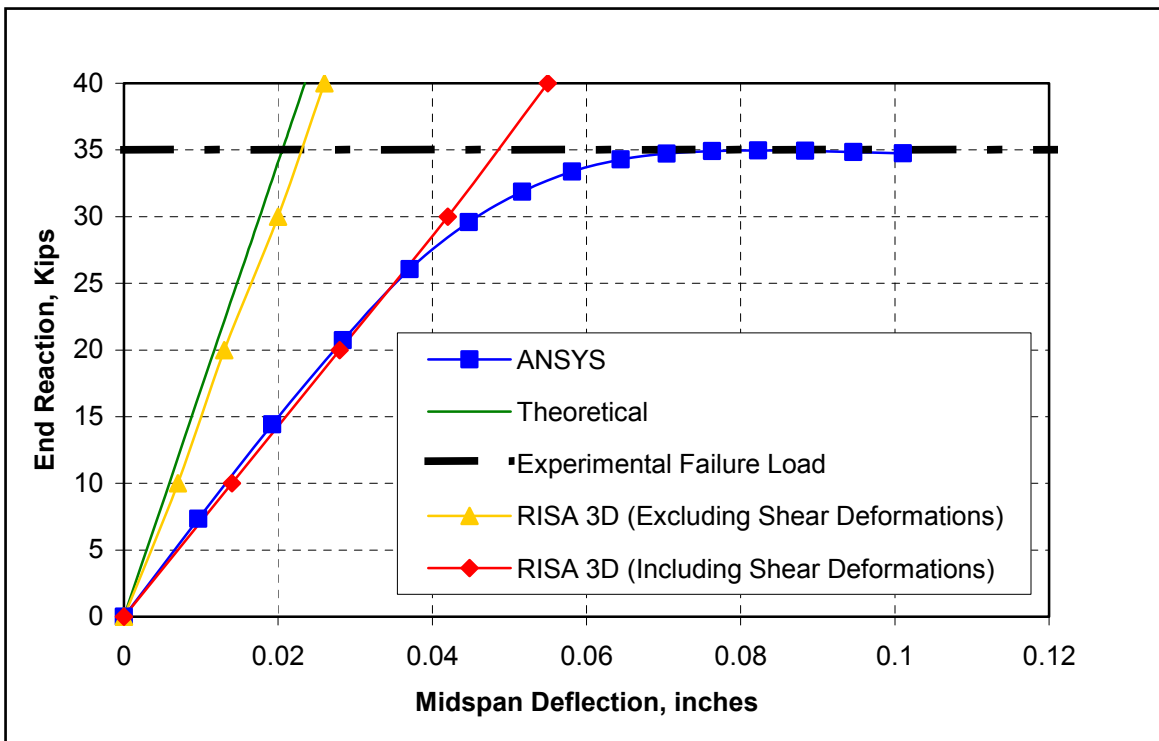


Figure 4.7 Load-deflection response of the model FEA-15a.

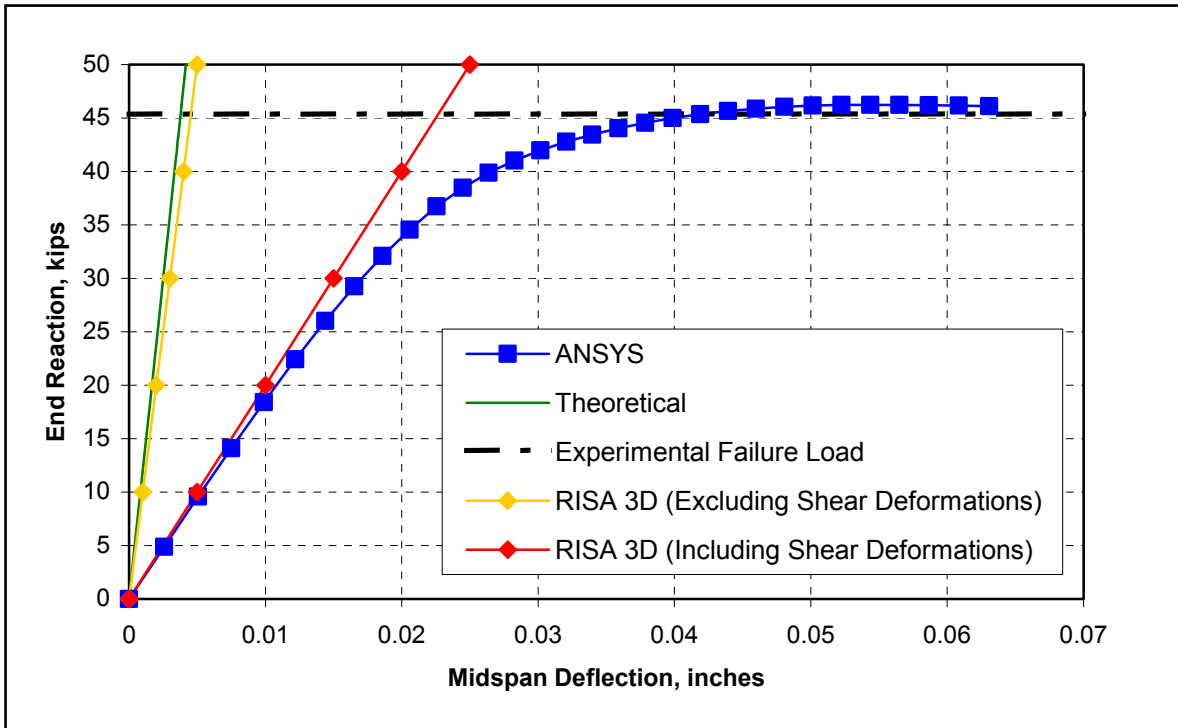


Figure 4.8 Load-deflection response of the model FEA-4a.

Figure 4.9 presents the validation results for the model FEA-7a. The initial load-deflection response of this model was fairly similar to that obtained from RISA 3D. However, it can be seen that the finite element model predicted a failure load below the experimental failure load. The FEM failure load was 61.53 kips against 67.50 kips from experimental data. It appears that this model failed to accurately predict the experimental failure load. It is important to mention that most of the specimens tested by Elgaaly and Salkar were performed on short span length, where the shear span was less than the depth of the section. For this particular specimen the shear span-to-depth ratio was 0.644, which may have influenced the behavior of the model. To investigate if in fact the model was affected by direct loading, an additional model similar to FEA-7a was created using a larger shear span length. A span length of 12.0 ft with a shear span-to-depth of 1.49 was used. As shown in Figure 4.10, the finite element model carried 9.18% more load than the previous model. It can also be seen that the model FEA-7b closely predicted the experimental failure load. The FEM failure load was 67.18 kips, while the experimental failure load was 67.50 kips.

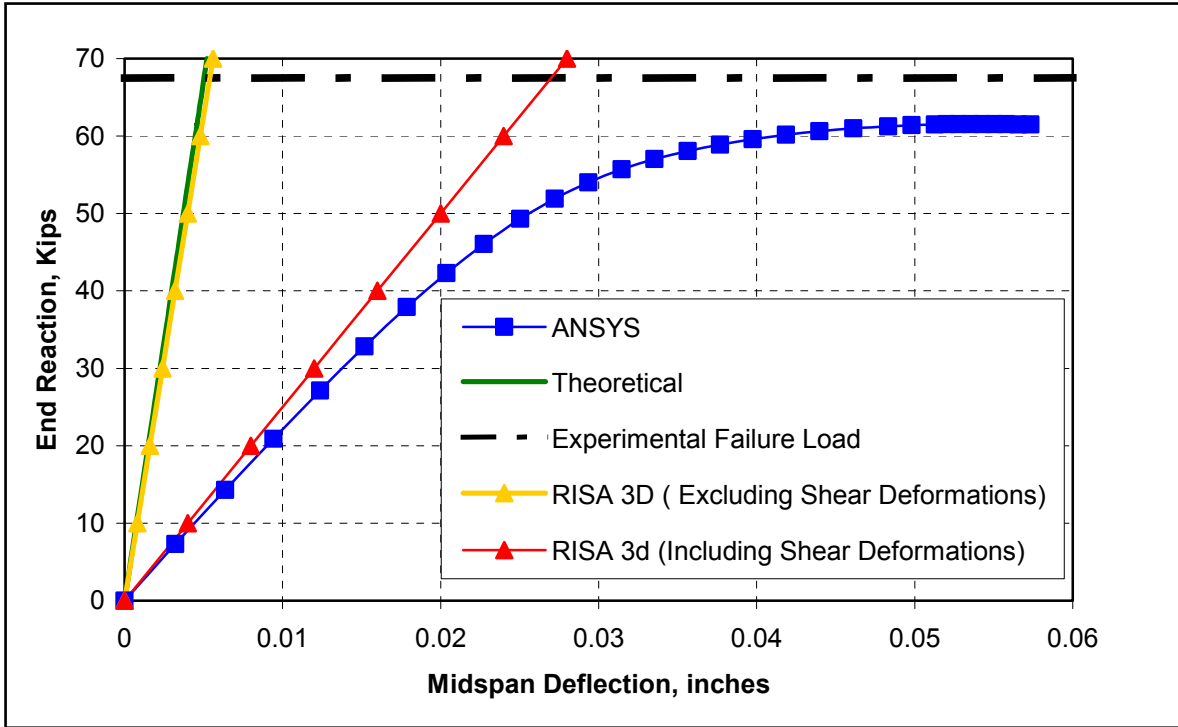


Figure 4.9 Load-deflection response of the model FEA-7a.

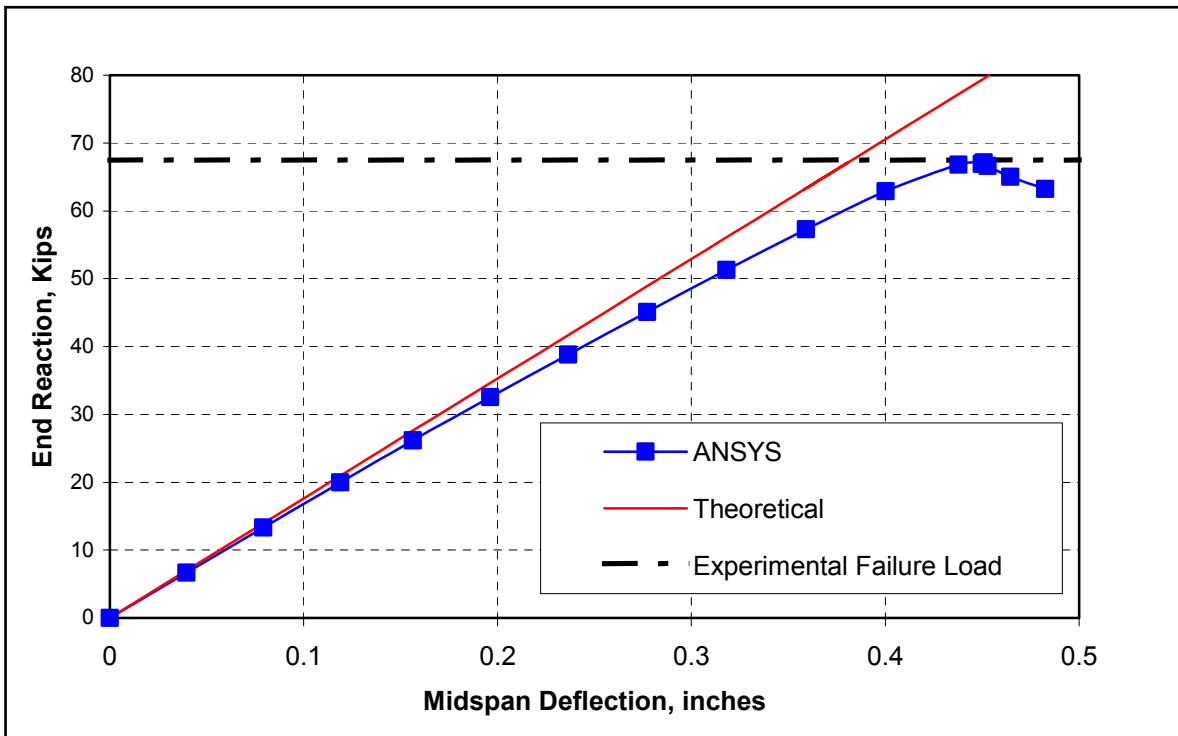


Figure 4.10 Load-deflection response of the model FEA-7b.

Since the behavior of the model FEA-7a was influenced by the fact that the shear span length was less than the depth of the beam, the model FEA-4a, which closely predicted the experimental failure load of the specimen, could have experienced similar behavior. The shear span-to-depth ratio for this specimen was 0.6691. To verify this, an additional model FEA-4b with cross-section and material properties similar to FEA-4a, but with higher shear span-to-depth ratio, was analyzed. The span length for the model FEA-4b was 12.00 ft, while shear span-to-depth ratio was 1.393. As shown in Figure 4.11, the finite element model carried more load than the previous model. The FEM failure load was 48.47 kips, which represent 4.823% more than the FEA-4a failure load, and 5.400% more than the experimental failure load. This result demonstrates, once again, that the shear span length has an influence in the web crippling strength of the models. Because the ultimate load obtained from the model FEA-4b was 2.46 kips more than the experimental failure load, the model was not used in the second stage of this study.

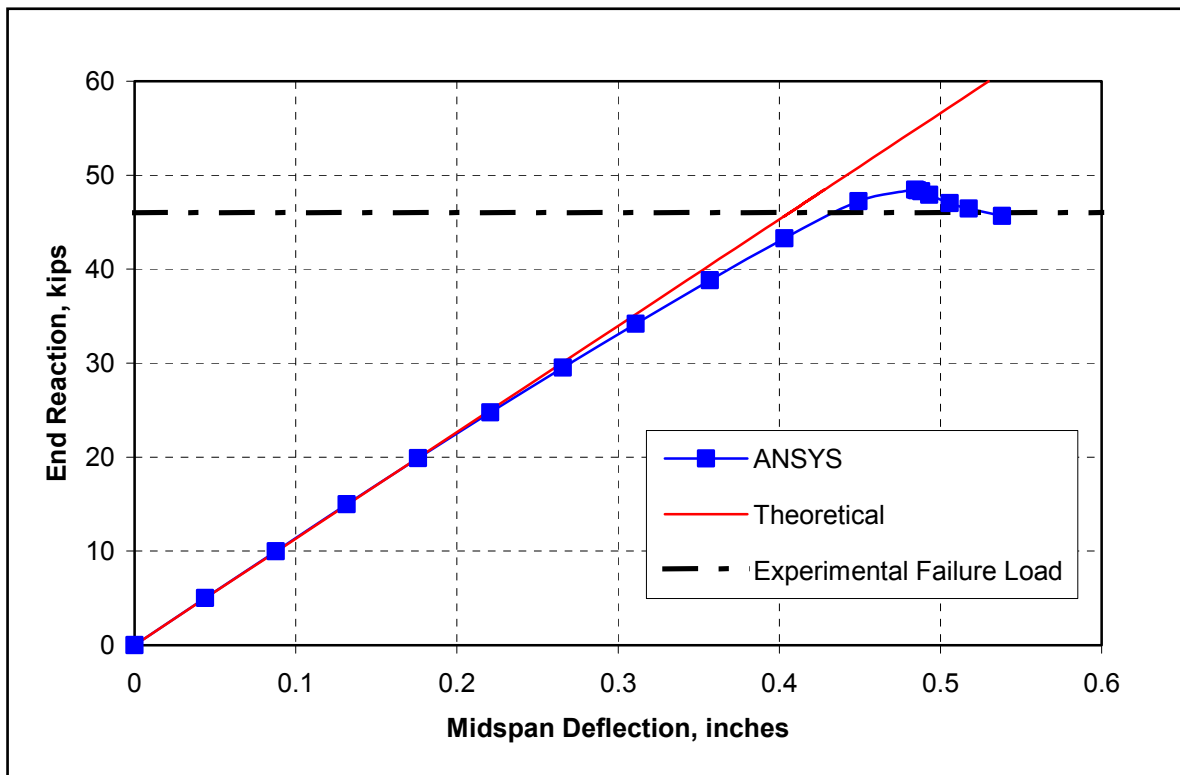


Figure 4.11 Load-deflection response of the model FEA-4b.

4.3.1.2 Steel-Concrete Composite Model

Figure 4.12 presents the validation results obtained for the steel-concrete composite model. The load-deflection curves from beam theory, stiffness analysis, and experimental data are shown in this figure. It can be seen that the load-deflection relationship has two different slopes. The initial slope of the load-deflection curve represents the initial experimental deflection and support reaction of the beam section due to the self-weight of the concrete slab. Although, this behavior might be possible to model in ANSYS by applying an initial condition to the element nodes it is impractical since the model has hundreds of nodes. Furthermore, the behavior of the section will not be affected by the initial midspan deflection due to self-weight of the concrete slab since the specimens were configured to fail by web crippling and not by flange bending at midspan. To make a fair comparison of the finite element results against the theoretical and experimental data, the initial deflection and support reaction were used as starting point for the FEM results. In other words, the initial deflection was added to the midspan deflections obtained by the finite element analysis, while the initial support reaction was added to the applied load at each step of the finite element analysis. Comparing both the experimental and FEM load-deflection curves, it can be seen that the finite element model satisfactorily predicted the load-deflection response and failure load of the tested composite beam. The ultimate failure load of the finite element model was 52.60 kips, while the experimental failure load was 53.00 kips. This represents a difference of just 0.754%.

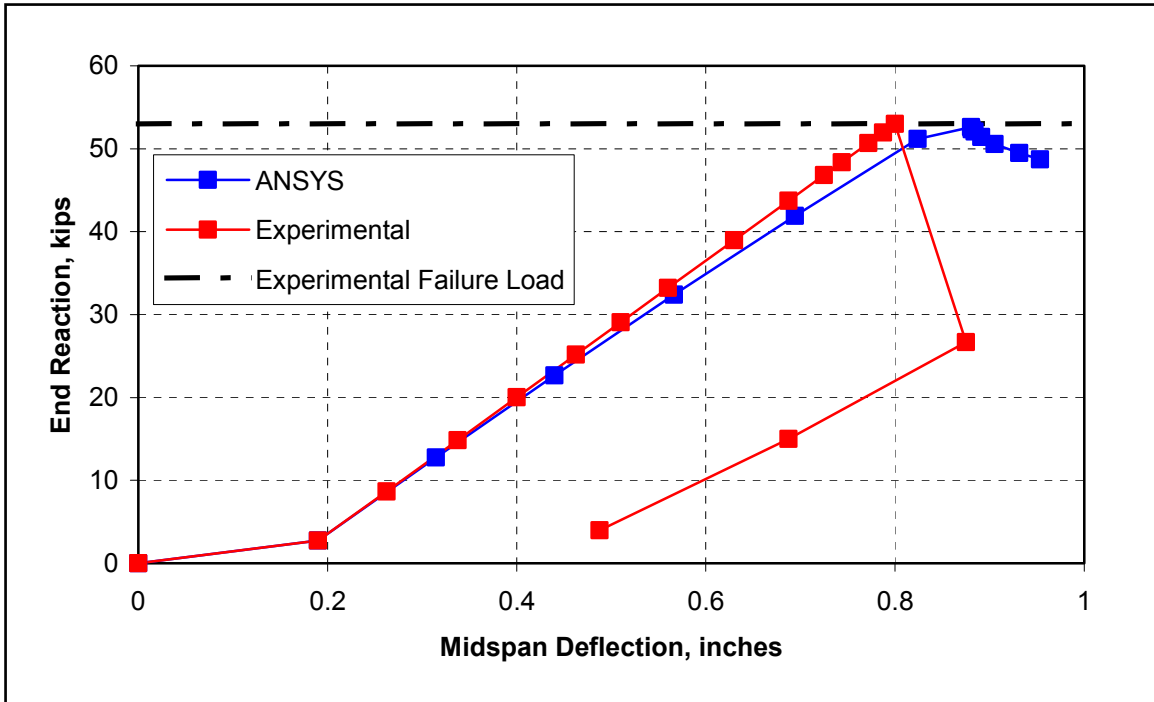


Figure 4.12 Load-deflection response of the model FEA-SC-2a.

4.3.2 Parametric Analysis

After validating the FEM models, a parametric analysis was performed by increasing the bearing-to-depth ratio, N/d , of the validated models. The material properties for the models with FEA-14x and FEA-7x series were set to 50 ksi and the span length was increased to 12.0 ft. The loading configuration also changed for these sections. Since the span length was increased to 12.0 ft, the single concentrated load applied at midspan would cause bending failure rather than web crippling failure over the supports. Instead, two single concentrated loads located symmetrically with respect to midspan were applied to these models. The location of the two single concentrated loads was such that the shear span-to-depth ratio was greater than 1.0, and that bending failure at midspan was not developed. The same concentrated load has to be resisted at each support. For the models with FEA-SC-2x series, the initial loading rate was increased to reduce the running time and computer memory. The initial loading rate was changed

from 5 kips to 10 kips, while the loading rate when the model was approaching the yield point remained at 2 kips. Table 4.4 shows the characteristics and identification system designated to the models.

Table 4.4.

Summary of the characteristics of each analysis model.

Model Designation	Beam Section	Bearing Length (in.)	Bearing-to-Depth Ratio	Span-to-Depth Ratio	Shear Span-to-Depth Ratio
FEA-14 <i>b</i>	W12x16 *	3.00	0.250	12.01	1.42
FEA-14 <i>c</i>	W12x16 *	4.00	0.334	12.01	1.08
FEA-7 <i>c</i>	W16x31 *	5.00	0.314	9.03	1.38
FEA-7 <i>d</i>	W16x31 *	6.00	0.376	9.03	1.13
FEA-7 <i>e</i>	W16x31 *	7.00	0.439	9.03	1.26
FEA-7 <i>f</i>	W16x31 *	8.00	0.502	9.03	1.00
FEA-7 <i>g</i>	W16x31 *	9.00	0.565	9.03	1.13
FEA-7 <i>h</i>	W16x31 *	10.00	0.627	9.03	1.00
FEA-7 <i>i</i>	W16x31 *	11.00	0.690	9.03	1.00
FEA-SC-2 <i>b</i>	W14x22 **	4.43	0.322	16.58	2.49
FEA-SC-2 <i>c</i>	W14x22 **	5.36	0.390	16.58	2.49
FEA-SC-2 <i>d</i>	W14x22 **	7.22	0.525	16.58	2.49
FEA-SC-2 <i>e</i>	W14x22 **	9.07	0.660	16.58	2.49
FEA-SC-2 <i>f</i>	W14x22 **	10.93	0.795	16.58	2.49

* Cross-section properties as reported by Elgaaly and Salkar (1991) were used only.

** Section and material properties as reported by Bryant (1993) were used.

4.3.2.1 Non-Composite Models

A total of nine non-composite, finite element models were analyzed. The bearing-to-depth ratio, N/d , for these models ranged from 0.250 to 0.690. Figures 4.13 to 4.21 present the comparison between the FEM and theoretical load-deflection curves. The beam theory equation used to compute the midspan deflection is:

$$\Delta_{\max} = \frac{Ra}{24EI} (3l^2 - 4a^2) \quad (4.1)$$

where:

Δ_{\max} : Maximum midspan deflection, in.

R : End reaction, kips

l : Span length from supports centerline, in.

a : Location of the concentrated load from support centerline, in.

E : Modulus of elasticity, 29000 ksi.

I : Moment of inertia of the beam section, in⁴.

In general, good agreement was found between the FEM and theoretical load-deflection responses at initial loading for most of the models. An unexpected load-deflection response was obtained from those models with relatively large bearing-to-depth ratio as seen in Figures 4.19 to 4.21. The load-deflection response for those models has some similarity to an arc, and it is more noticeable for very large bearing-to-depth ratio. From Figures 4.13 to 4.18, it can be seen that when the length of the bearing is relatively small the deflection behavior of the model is similar to a simply supported beam. However, different behavior is observed when the length of the bearing becomes larger. This is because the bearing support restricts the end rotation of the beam section resulting in lower midspan deflections than predicted. It is worth noting that, even when the bearing block was defined by restraining all degrees of freedom (translations in the x, y, and z directions, and rotations about the x, y, and z-axes) on those nodes located at the bottom flange of the beam section, this boundary condition is still considered as a pin

connection since the end of the beam is free to rotate. However, the rotation of the beam is certainly more restricted for a large bearing length.

The comparison between FEM failure load and the predictions of the current 1999 AISC LRFD web crippling equation (K1-5b) is also shown in the Figures 4.13 to 4.21. It can be easily seen that the FEM web crippling strength is consistently higher than the predictions of the web crippling equation (K1-5b). Table 4.5 presents a summary of the finite element results and the comparison with the predicted failure load for the current 1999 AISC LRFD web crippling equation (K1-5b). From the table, a tendency for the FEM load-to-AISC load ratio to decrease with increasing N/d ratio within the same series, except the model FEA-7d in the FEA-7x series, is seen.

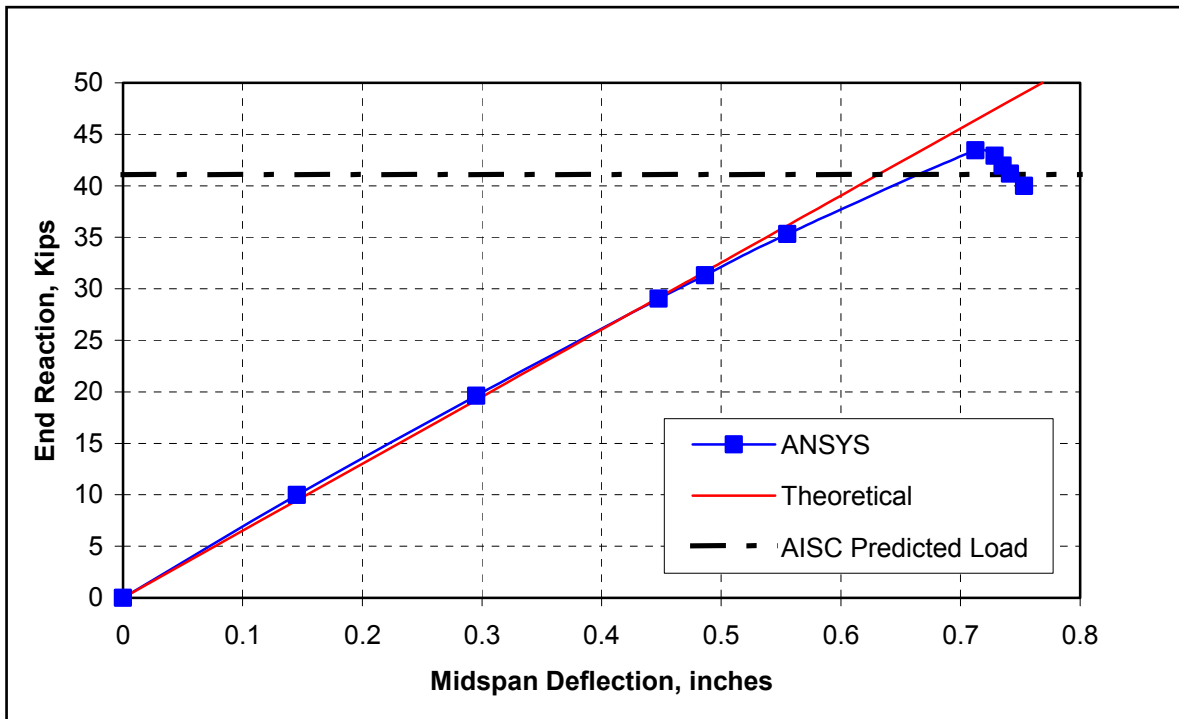


Figure 4.13 Load-deflection response of the model FEA-14b, W12x16 with $N = 3.0$ in.

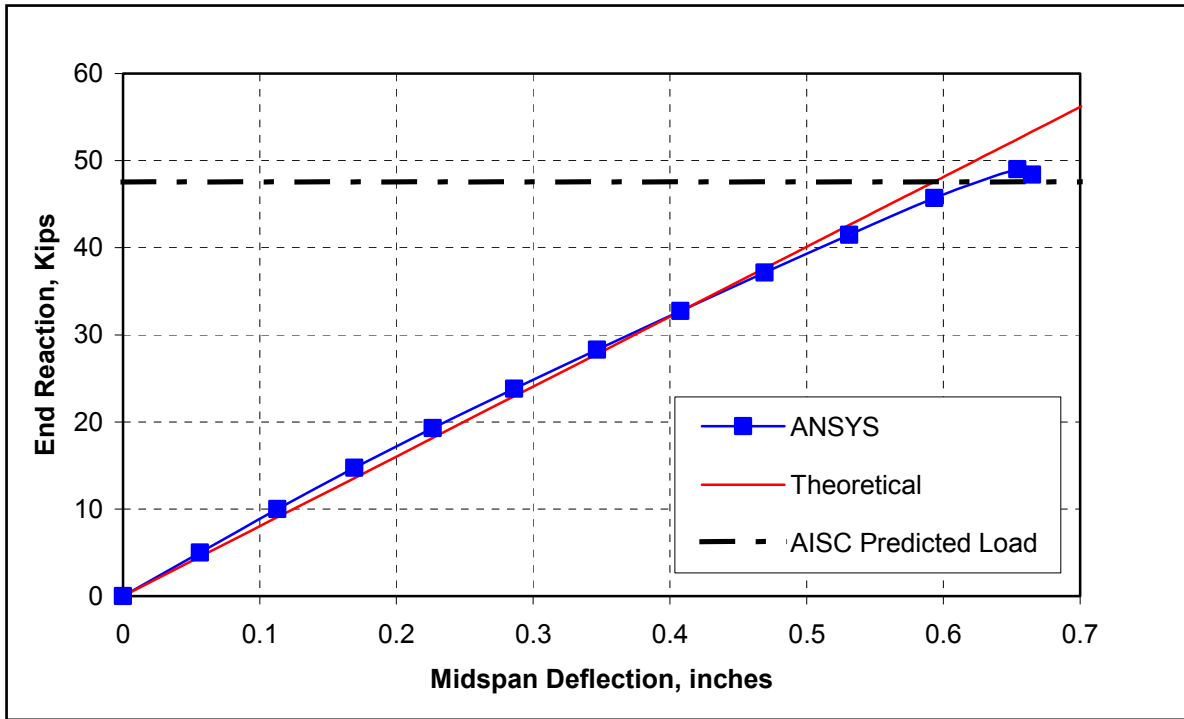


Figure 4.14 Load-deflection response of the model FEA-14c, W12x16 with N = 4.0 in.

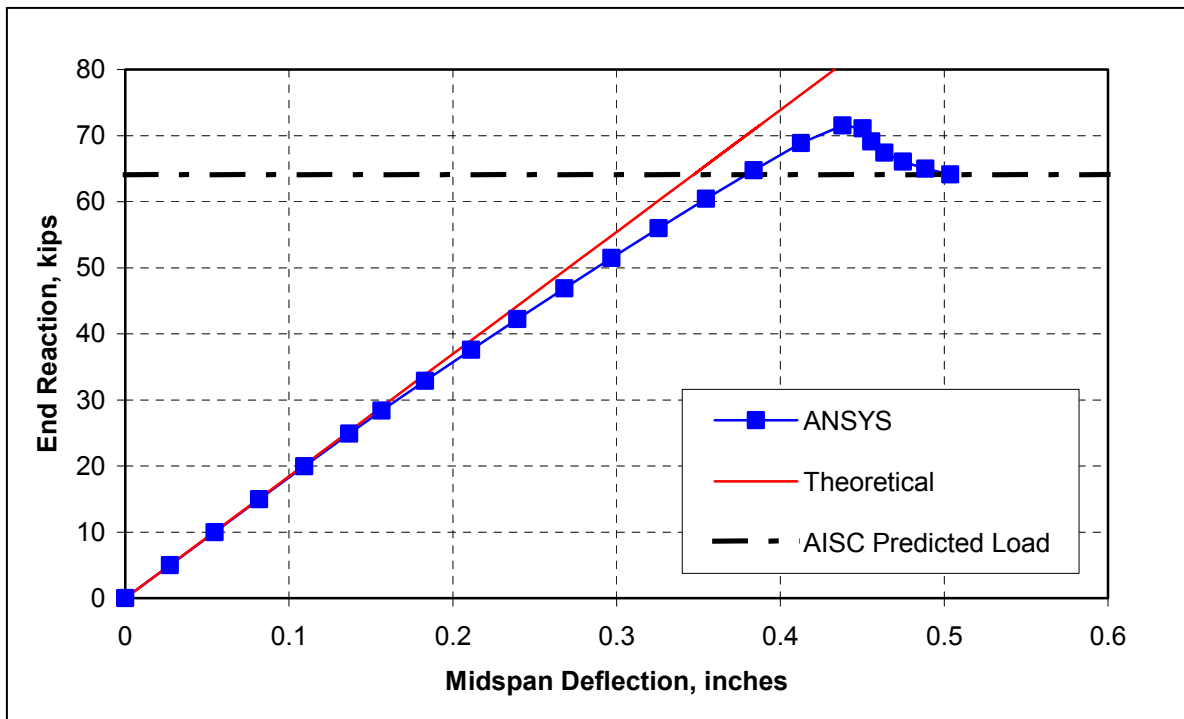


Figure 4.15 Load-deflection response of the model FEA-7c, W16x31 with N = 5.0 in.

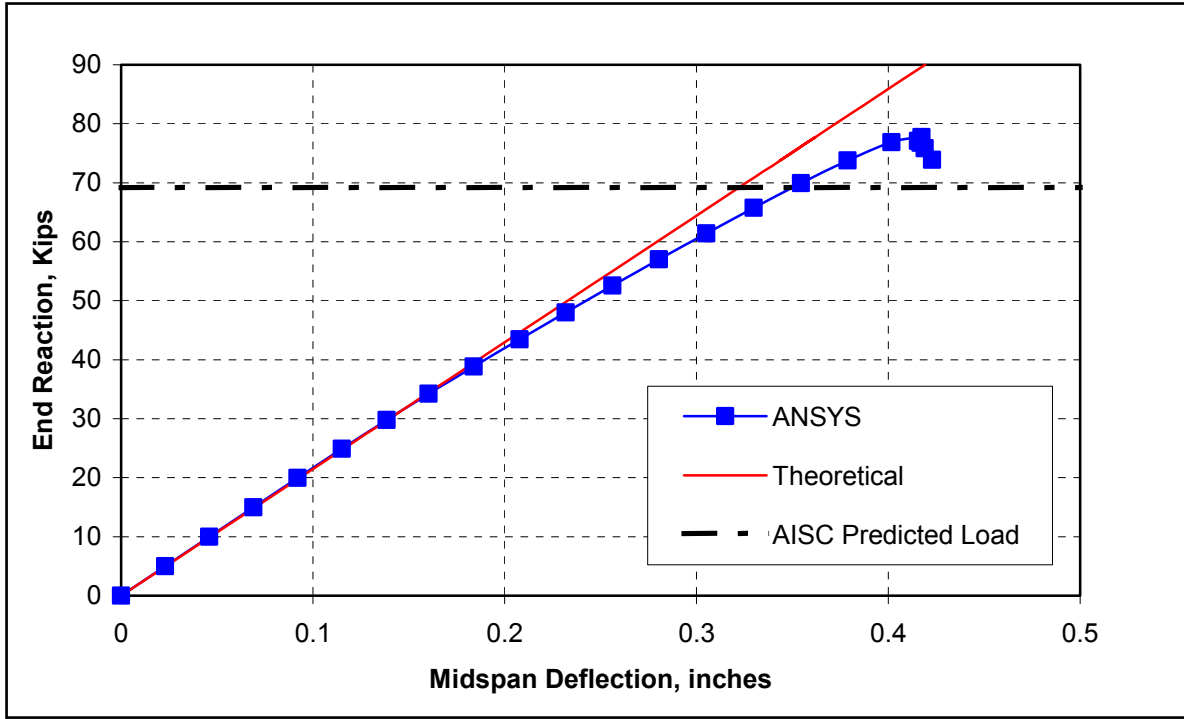


Figure 4.16 Load-deflection response of the model FEA-7d, W16x31 with N = 6.0 in.

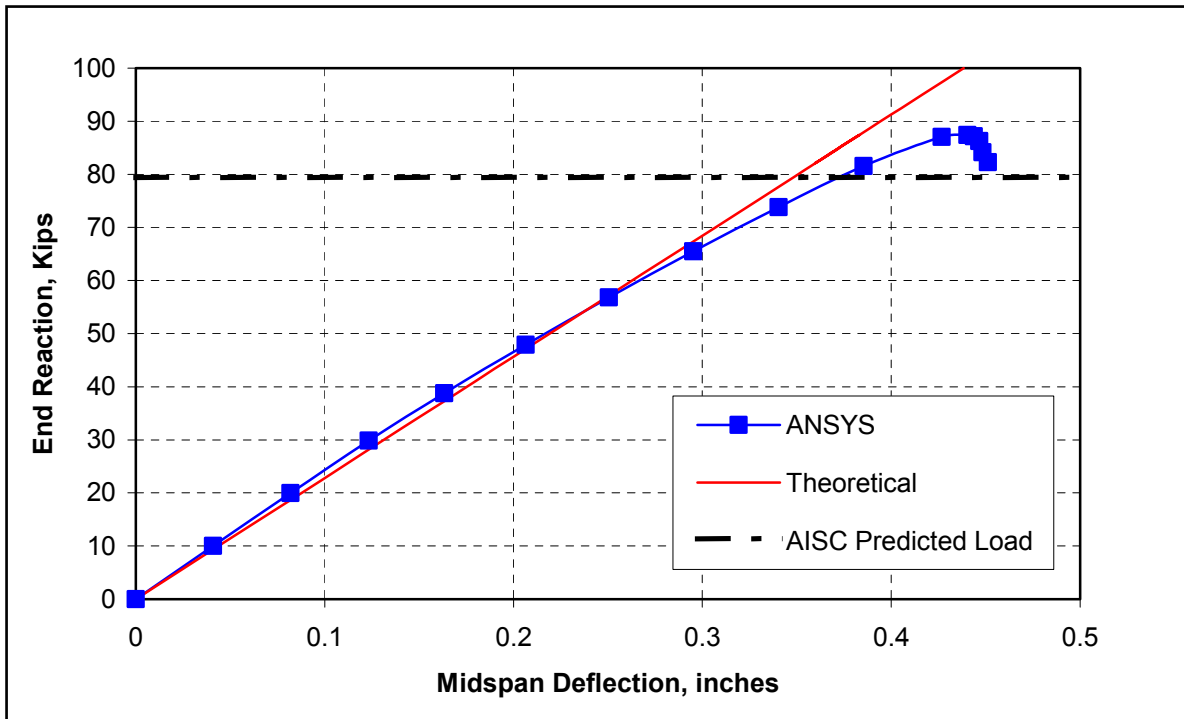


Figure 4.17 Load-deflection response of the model FEA-7e, W16x31 with N = 7.0 in.

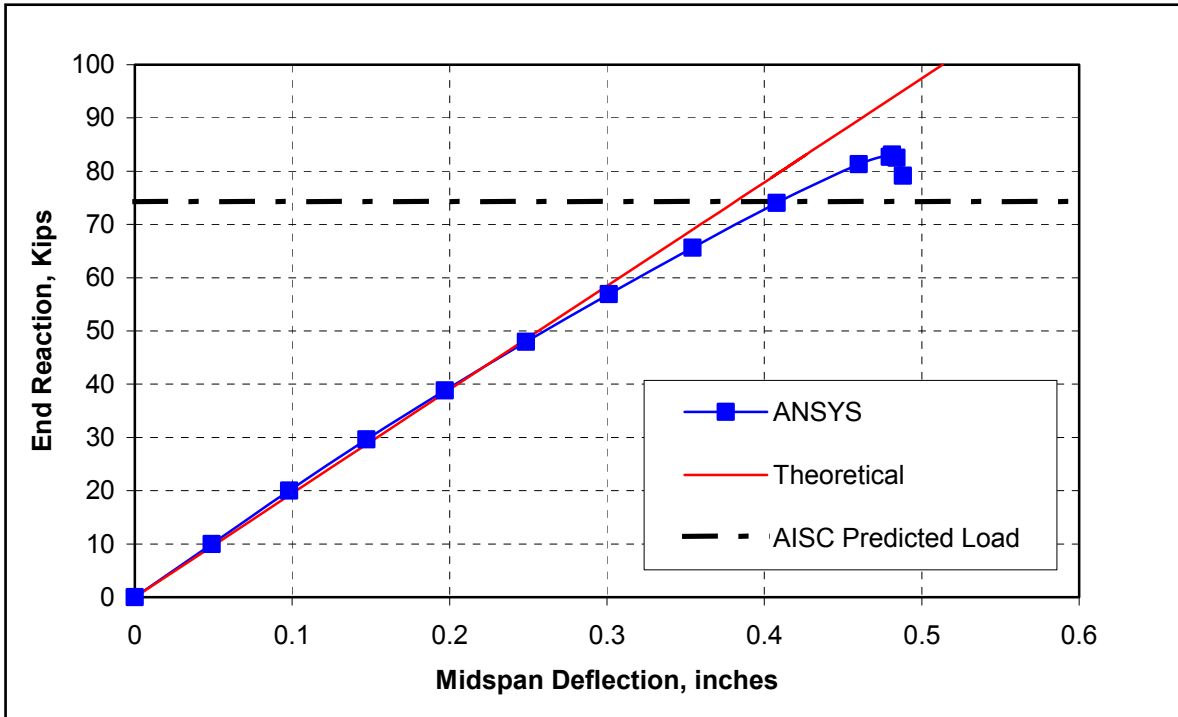


Figure 4.18 Load-deflection response of the model FEA-7f, W16x31 with N = 8.0 in.

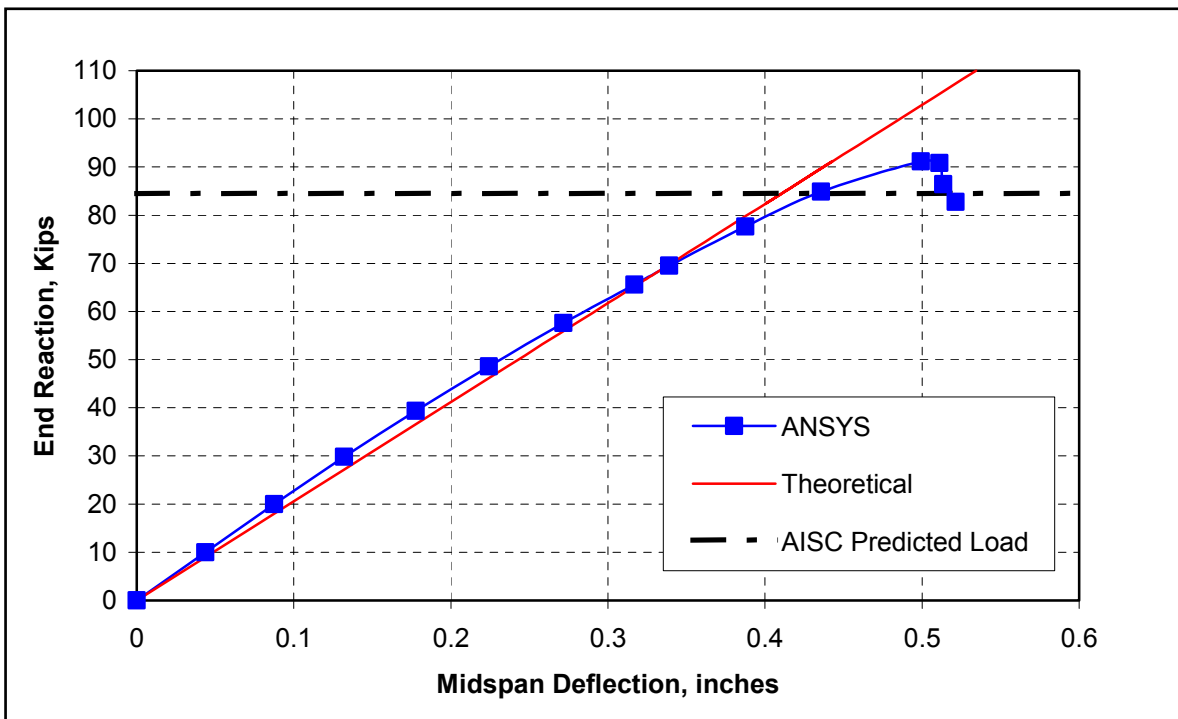


Figure 4.19 Load-deflection response of the model FEA-7g, W16x31 with N = 9.0 in.

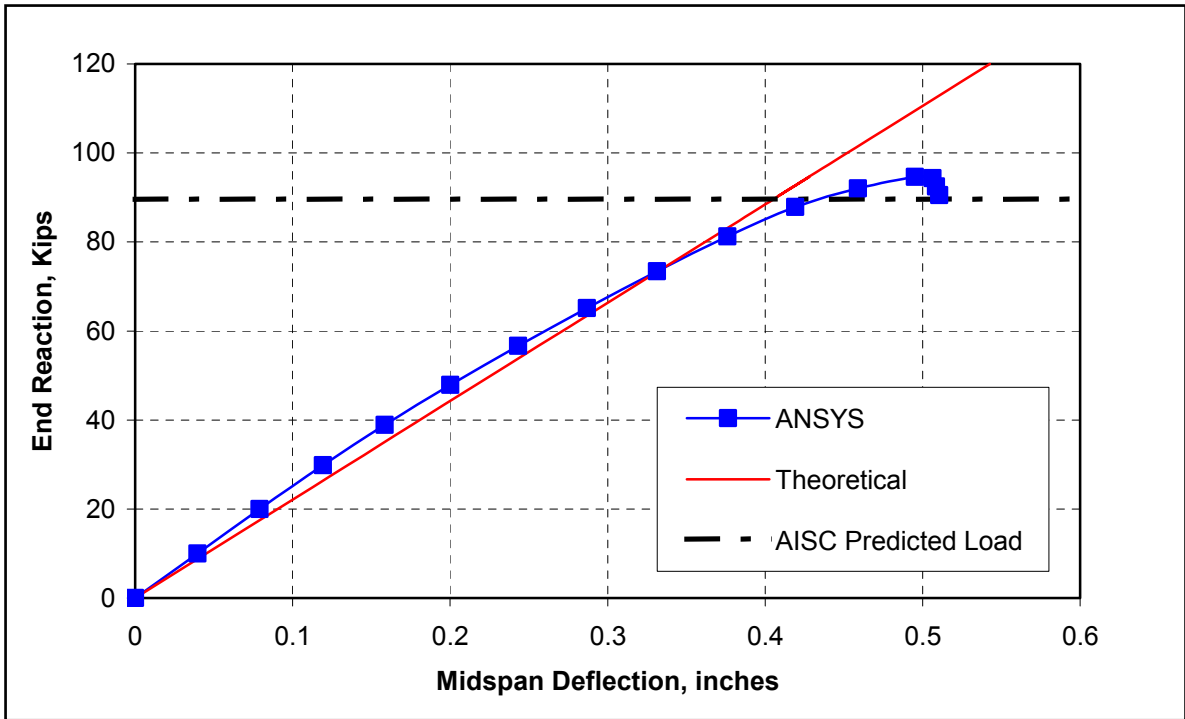


Figure 4.20 Load-deflection response of the model FEA-7h, W16x31 with N = 10.0 in.

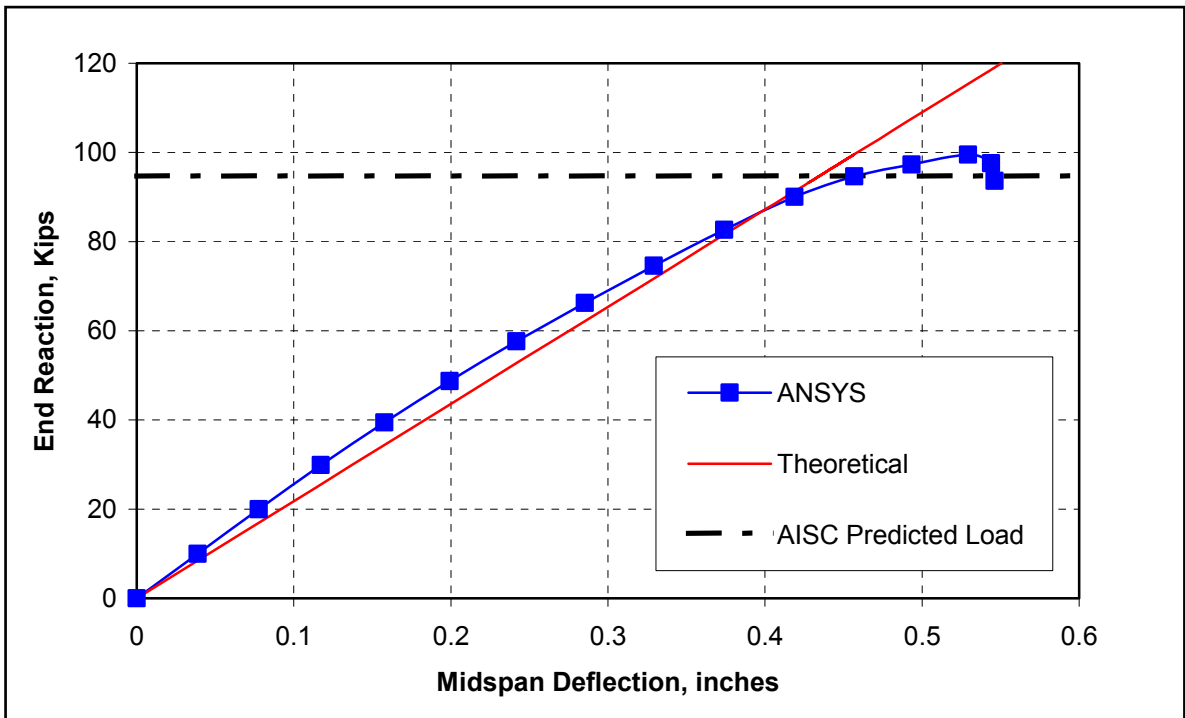


Figure 4.21 Load-deflection response of the model FEA-7i, W16x31 with N = 11.0 in.

Table 4.5.

Summary and comparison between the FEM web crippling strength results of the non-composite models and the predictions of the 1999 AISC LFRD web crippling equation (K1-5b).

Test Designation	Beam Section	Bearing Length (in.)	N/d	FEM Failure Load, R_{FEM} (kips)	1999 AISC LFRD Failure Load, R_{AISC} (kips)	R_{FEM} / R_{AISC}
FEA-14b	W12X16	3.00	0.250	43.45	41.09	1.06
FEA-14c	W12X16	4.00	0.334	49.02	47.54	1.03
FEA-7c	W16x31	5.00	0.314	71.54	64.09	1.12
FEA-7d	W16x31	6.00	0.376	77.72	69.19	1.12
FEA-7e	W16x31	7.00	0.439	83.10	74.29	1.12
FEA-7f	W16x31	8.00	0.502	87.04	79.40	1.10
FEA-7g	W16x31	9.00	0.565	91.13	84.50	1.08
FEA-7h	W16x31	10.00	0.627	94.61	89.60	1.06
FEA-7i	W16x31	11.00	0.690	99.53	94.70	1.05

Web crippling behavior is not evident from the load-deflection curves. However, web crippling behavior can be seen by plotting the web crippling shape at different load steps. Figure 4.22 shows a typical web crippling shape for those models with relatively small bearing-to-depth ratios. Appendix B includes the web crippling response for each finite element model analyzed in this study. As seen in the figure, the web progressively moved as the load increased until failure occurred. Note that the web crippling mode is similar to the initial imperfection shape. A different behavior was experienced by the models with relatively large bearing-to-depth ratios. Figure 4.23 illustrates the web crippling shape at the end of the web of model FEA-7i. The bearing-to-depth ratio for this model was 0.690. As seen in the figure, the web begins to deform opposite to the direction of its initial imperfection. The web reached a minimum out-of-plane deformation of 0.174 in. at a load equal to 66.58% of the failure load, and then the web began to progressively cripple until it failed in the same direction as the initial

deformation. The out-of-plane deformation at failure load was 0.506 in. Again, it can be noted that the web crippling shape at every load step was similar to its initial web deformation. The behavior of decreasing the out-of-plane deformation of the web at initial loading can be explained by examining the web crippling shape at a different location. Figure 4.24 shows the web crippling shape at 5.0 in. from the end of the web of the model FEA-7*i*. It can be seen that the web appears to cripple initially at 1/4 of the height of the web and opposite to the direction of the initial imperfection; however, the web finally crippled in the same direction of the initial deformation. This behavior also demonstrates that the initial imperfection governs the web crippling failure mode.

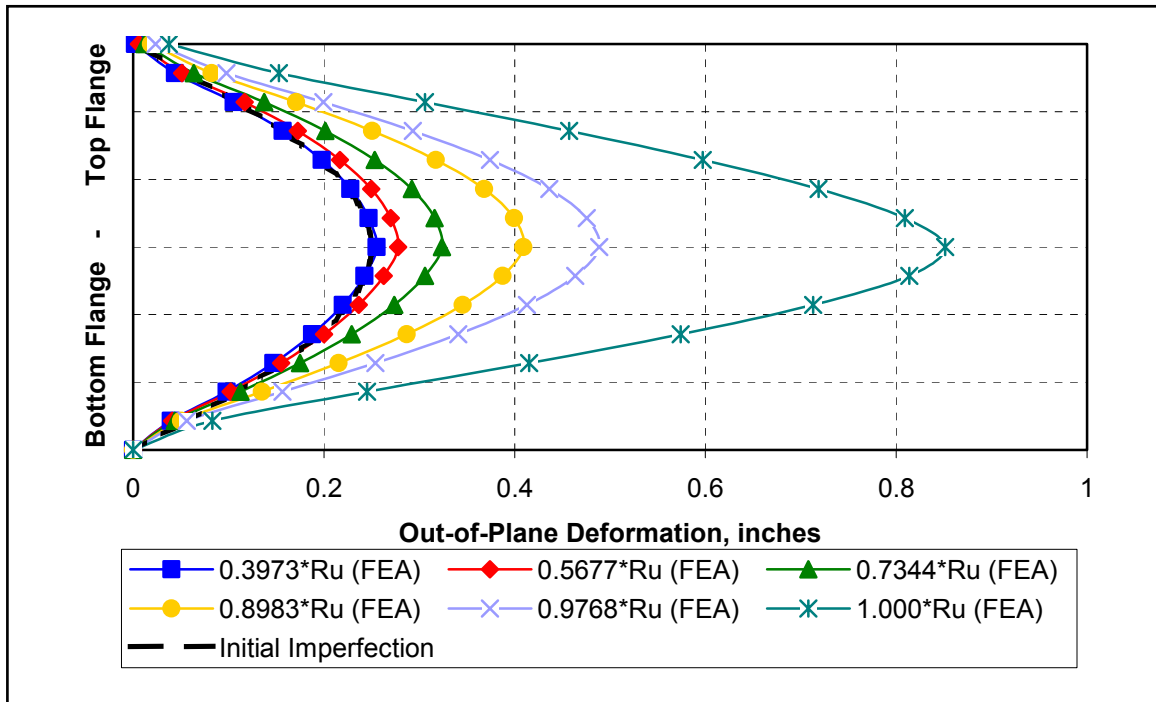


Figure 4.22 Typical web crippling shape at different load steps for models with relatively small bearing-to-depth ratio.

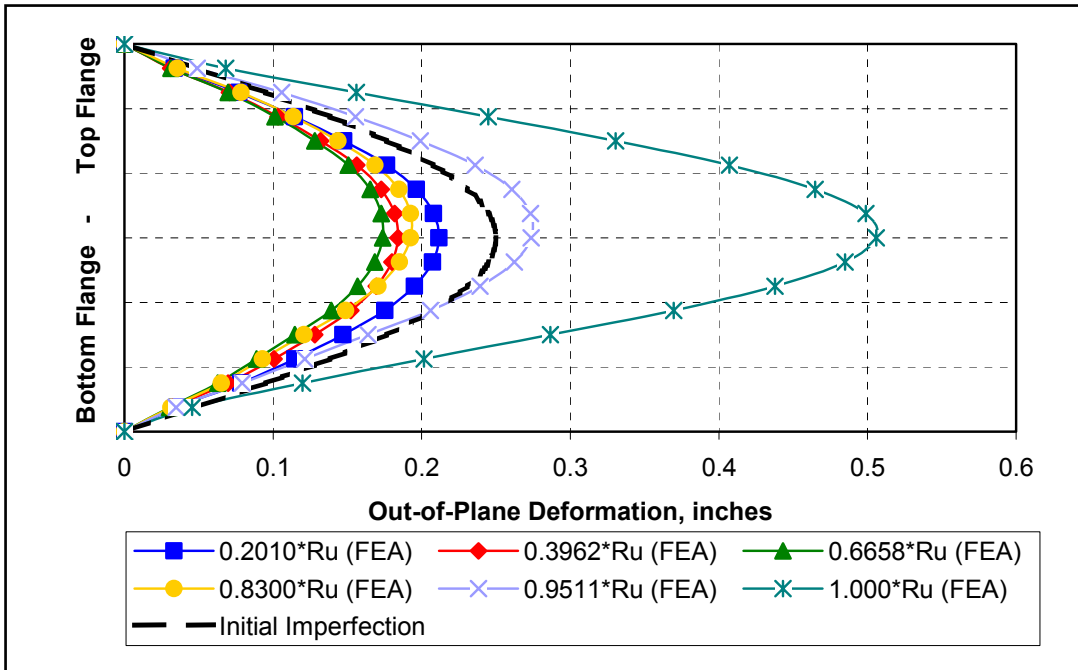


Figure 4.23 Web crippling shape at the end of the beam section at different load steps of the model FEA-7i.

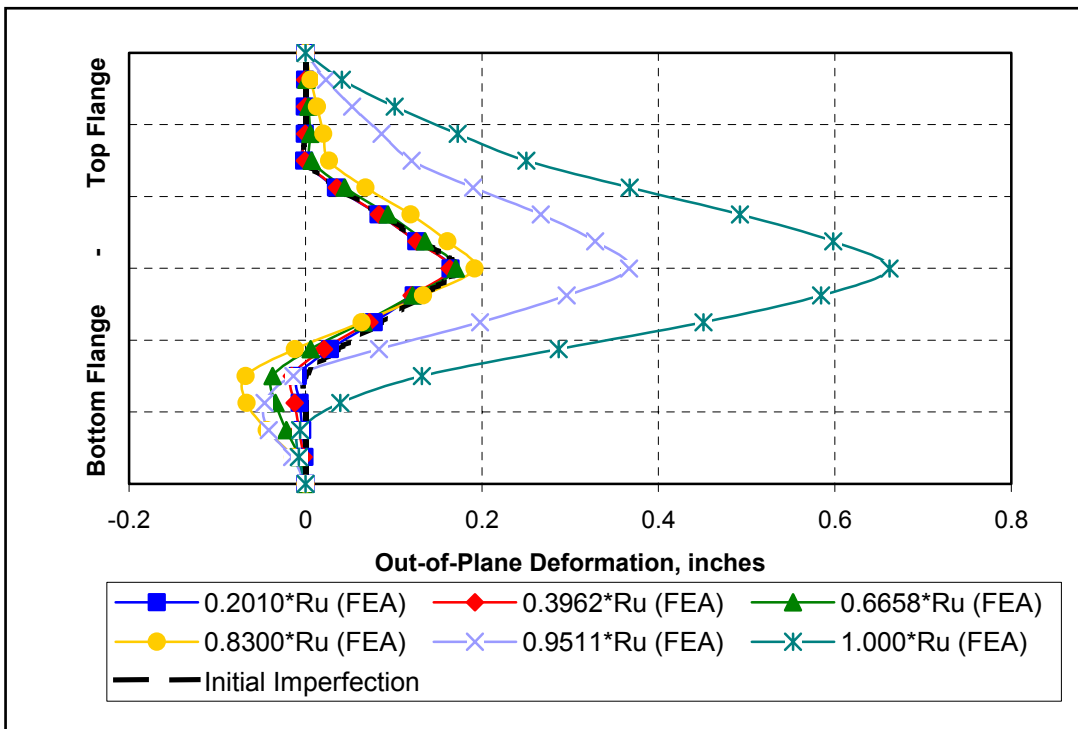


Figure 4.24 Web crippling shape at 5.0 in. from the end of the beam section at different load steps of the model FEA-7i.

4.3.2.2 Steel-Concrete Composite Models

Five finite element models using composite action were analyzed. The bearing-to-depth ratio for these models ranged from 0.322 to 0.795. Figure 4.25 to 4.29 show the comparison between the FEM and theoretical load-deflection curves. The initial slope of the load-deflection curve is similar to the experimental data and was included in the load-deflection curve. The initial deflection and end reaction caused by the self-weight of the concrete slab were taken as 0.190 in. and 2.75 kips, respectively. These initial values were used as starting points for the FEM results. Equation (4.1) was used to predict the midspan deflection of the composite models. The effective moment of inertia was taken from the experimental data as 668.0 in^4 .

From the figures, it can be noted that the load-deflection response of those models, with relatively small bearing-to-depth ratios, was quite similar to the beam theory curve at initial loading. Contrary to the behavior observed with the non-composite models, the load-deflection curve was much more similar to the beam theory curve for those models with relatively large bearing-to-depth ratio. The load-deflection curve of the model FEA-SC-2*f* better shows the arc-like behavior as consequence of having a large bearing length.

The maximum web crippling strength predicted by the FEM results and the predictions of the current 1999 AISC LRFD Specification are also shown in Figures 4.25 to 4.29. As seen in these figures, the FEM failure loads were higher than the prediction from the 1999 AISC LRFD web crippling Equation (K1-5b), except for models FEA-SC-2*d* and FEA-SC-2*e*. The FEM failure load of the FEA-SC-2*d* was close to the AISC predictions, while the FEM failure load of the FEA-SC-2*e* was slightly lower than that predicted by the AISC web crippling Equation (K1-5b). Table 4.6 presents a summary of the finite element results as well as a comparison with the predicted failure load for the current 1999 AISC LRFD web crippling Equation (K1-5b). As previously shown, there is a tendency for the FEM load-to-AISC load ratio to decrease with increasing N/d ratio except for the model FEA-SC-2*f*. Again, the initial web deformation seems to influence

the ultimate strength. This can be noted from the behavior of the model FEA-SC-2*f*, which had a very different web crippling behavior than any other model in this series. Figure 4.30 shows the web crippling shape of the model FEA-SC-2*f*. As seen in this figure, the maximum web deformation was not obtained at the mid-height of the web. Instead, it was seen at approximated 1/3 of the depth of the beam section. Furthermore, the beam section crimped opposite to the imperfection imposed to the web. As result, the section carried 6.220 kips more than the prediction of the 1999 AISC LRFD web crippling equation (K1-5b), which was the largest difference within this series, deviating from the tendency mentioned before.

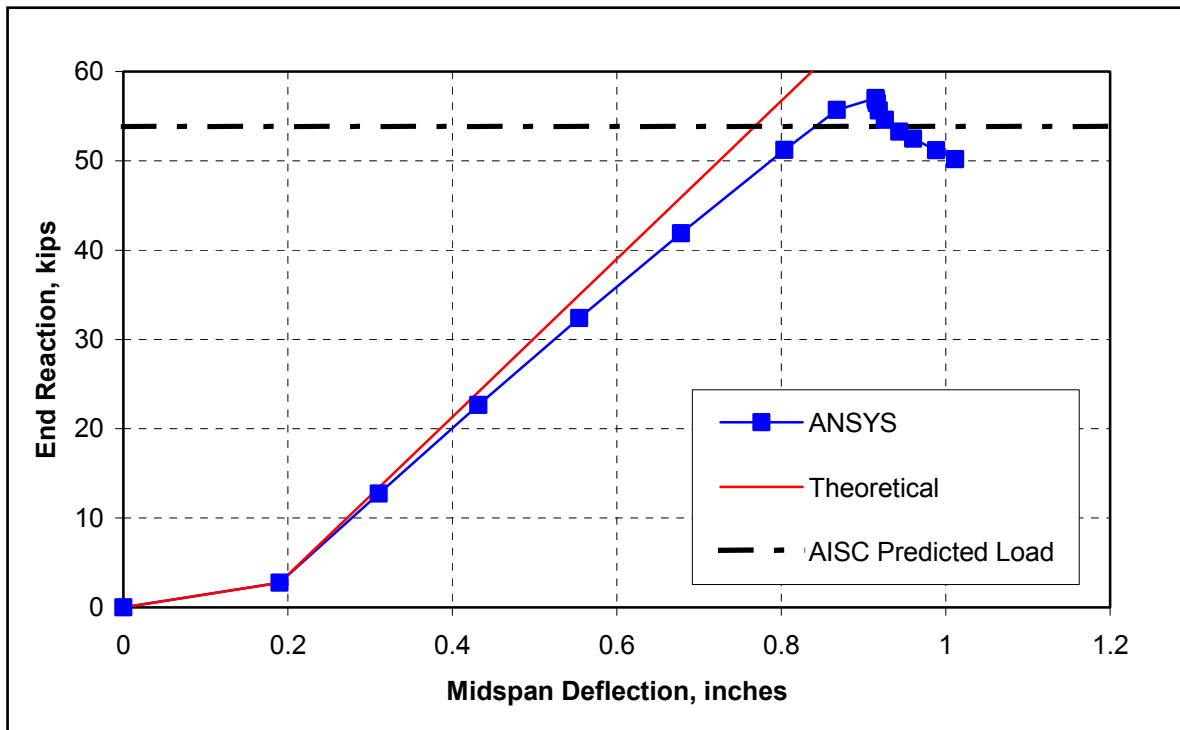


Figure 4.25 Load-deflection response of the model FEA-SC-2*b*, W14x22 with N = 4.43 in.

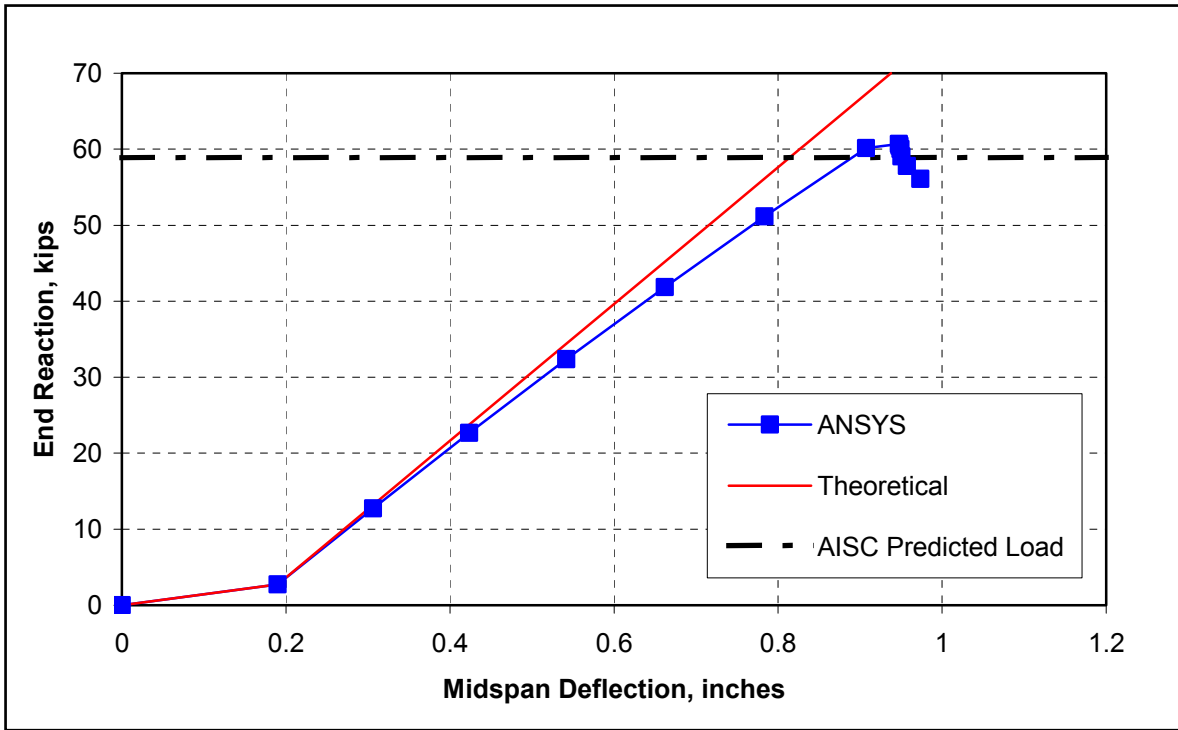


Figure 4.26 Load-deflection response of the model FEA-SC-2c, W14x22 with $N = 5.36$ in.

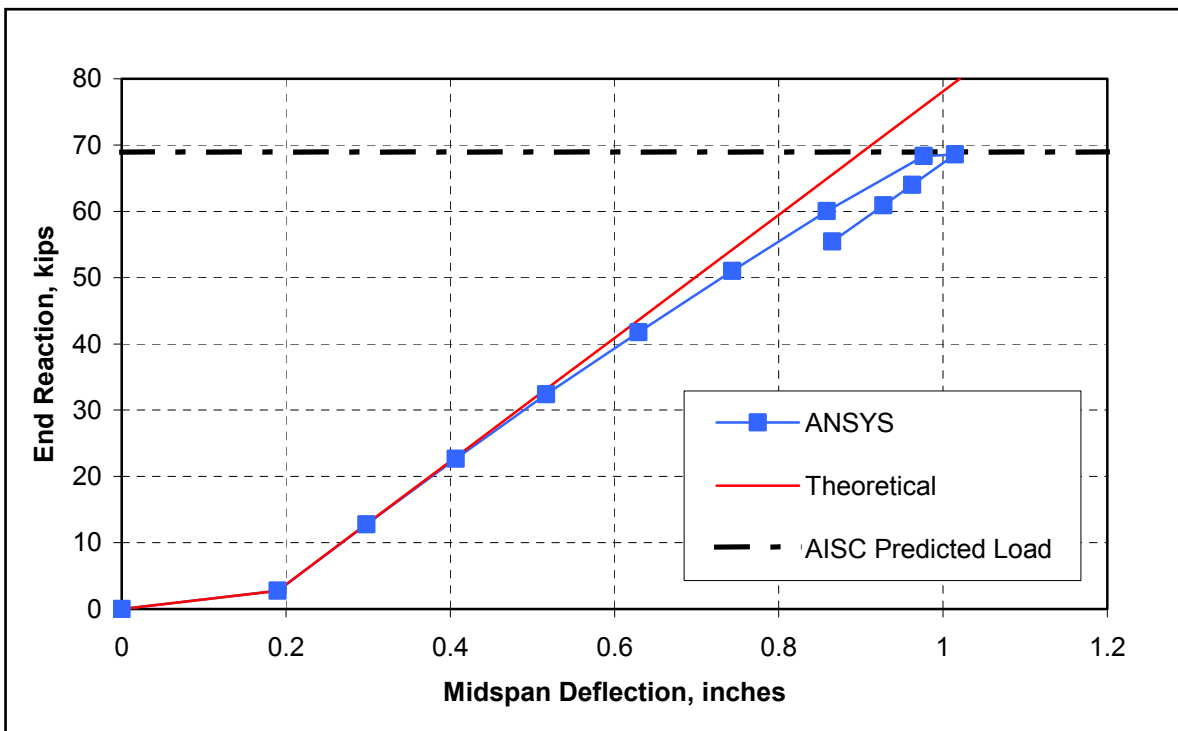


Figure 4.27 Load-deflection response of the model FEA-SC-2d, W14x22 with $N = 7.22$ in.

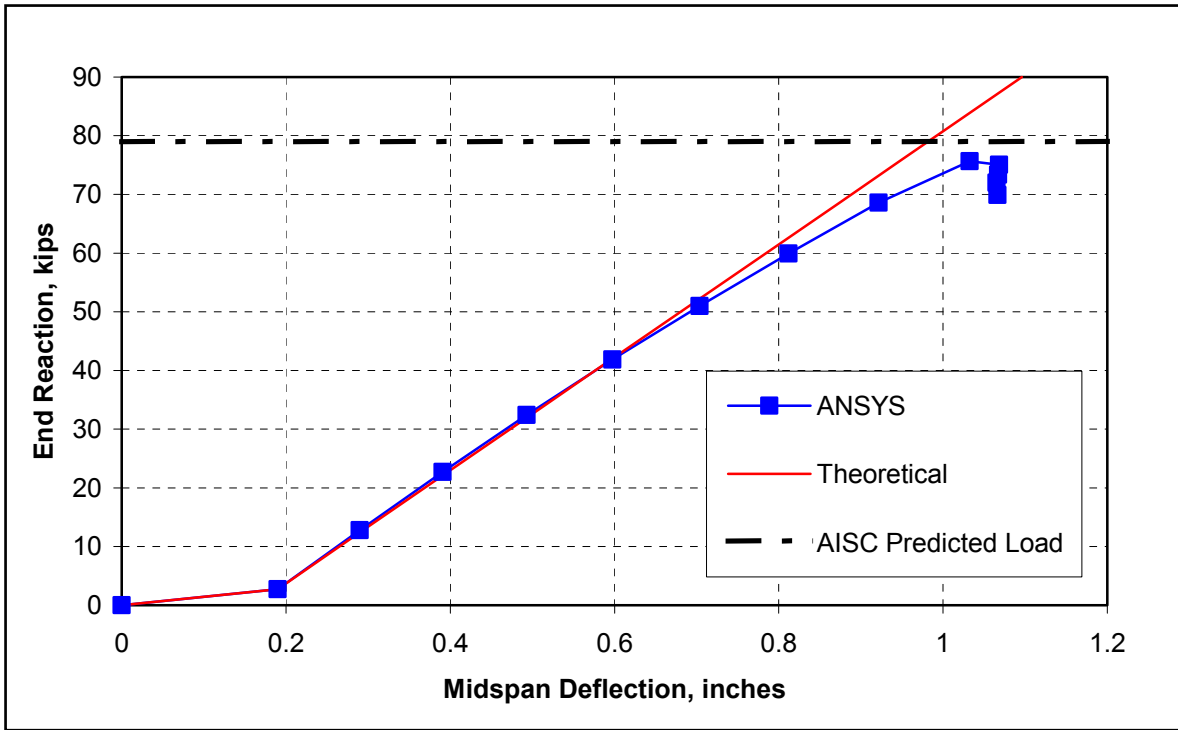


Figure 4.28 Load-deflection response of the model FEA-SC-2e, W14x22 with N = 9.02 in.

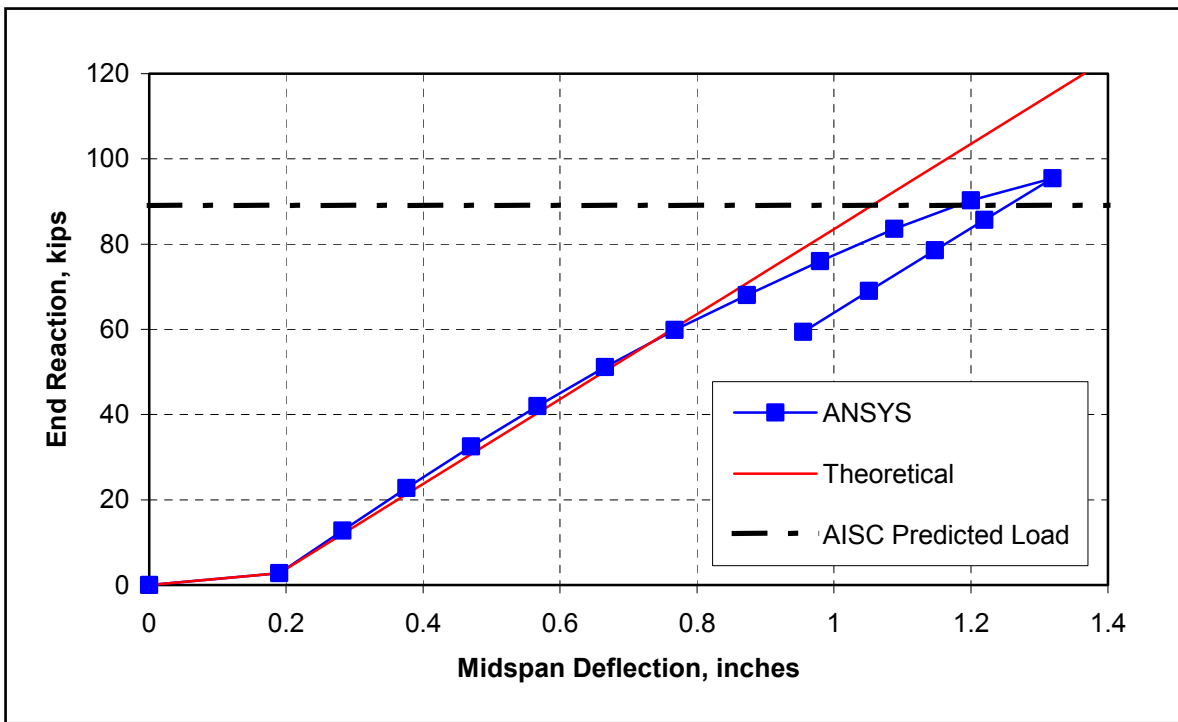


Figure 4.29 Load-deflection response of the model FEA-SC-2f, W14x22 with N = 10.93 in.

Table 4.6.

Summary and comparison between the FEM web crippling strength results of the composite models and the predictions of the 1999 AISC LFRD web crippling equation (K1-5b).

Test Designation	Beam Section	Bearing Length (in.)	N/d	FEM Failure Load, R_{FEM} (kips)	1999 AISC LFRD Failure Load, R_{AISC} (kips)	R_{FEM} / R_{AISC}
FEA-SC-2b	W14x22	4.43	0.3221	57.03	53.93	1.057
FEA-SC-2c	W14x22	5.36	0.3897	60.67	58.97	1.029
FEA-SC-2d	W14x22	7.22	0.5248	68.57	69.06	0.9929
FEA-SC-2e	W14x22	9.07	0.6599	75.63	79.12	0.9559
FEA-SC-2f	W14x22	10.93	0.7951	95.42	89.20	1.070

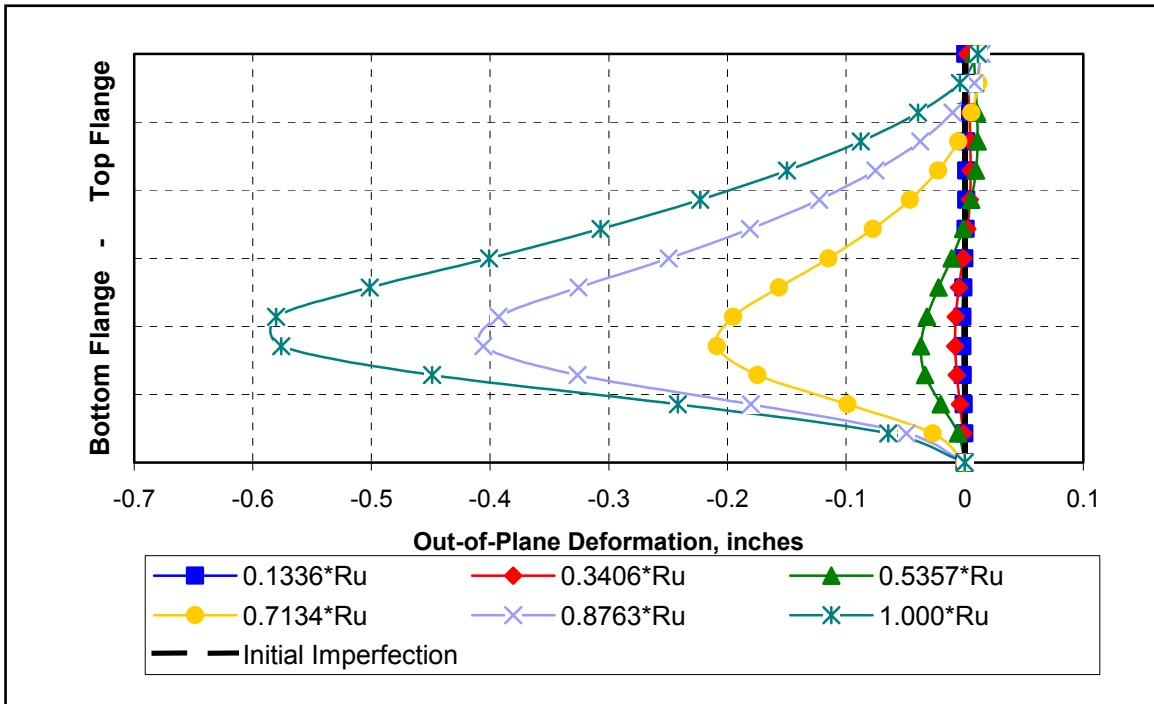


Figure 4.30 Web crippling shape at 10.0 in. from the end of the beam different load steps of the model FEA-SC-2f.

4.4. Discussion

First, it is noted that the finite element models analyzed in the validation stage closely predicted the failure loads of the tested beams. The load-deflection curve was also well predicted by the models in the finite element analyses. The differences found between the FEM and beam theory load-deflection curves for the non-composite models with large bearing-to-depth ratio are due to the restriction imposed by the support. Some difference was also found between the FEM and beam theory load-deflection curves for the composite models. Contrary to the first observation, the difference was found in the models with small bearing-to-depth ratio. This difference is due to the fact that the model was validated against the experimental load-deflection curve and not against the theoretical load deflection curve. The validation results in this series show good agreement between the FEM and experimental load-deflection curves. The length of the bearing also affected the load-deflection curve for the composite models. The arc-like behavior of the load-deflection curve of the model FEA-SC-2*f* illustrates this point.

In the validation stage, it was noted that model FEA-7*a* failed 5.97 kips below the experimental failure load. Since the shear span-to-depth ratio for this model was 0.644, direct compression failure could be the cause for this early failure. An additional model with a shear span-to-depth ratio greater than 1.0 was created and analyzed. The result showed that, in fact, the shear span length influenced the web crippling strength for this model. The same behavior was seen for the model FEA-4*a*. Table 4.7 presents a summary of the web crippling results with different shear span-to-depth ratios. Both results suggest that the web crippling strength is affected by the shear span-to-depth ratio. One might argue that this behavior is only encountered in the finite element models, however, this observation was made early in the 1930's. Ketchum and Draffin (1932) observed this behavior when they tested similar beam sections with two different load configurations. They observed that the ultimate collapse load for those beam sections tested with shear span-to-depth ratios greater than 1.0 was slightly higher than those beam sections tested with shear span-to-depth ratios less than 1.0. The difference was about 10% of the ultimate load capacity. The difference between the web crippling

failure load obtained from the models FEA-4*a* and FEA-4*b* was 4.82%, while the difference obtained from the model FEA-7*a* and FEA-7*b* was 9.18%.

The web crippling failure mode shape was predicted quite well in the finite element analyses. Figure 4.31 shows the FEM and the experimental failure mode shape for the validation model FEA-SC-2*a*. From this figure, it can be seen that the location of the maximum out-of-plane deformation is different in the FEM and test results. The maximum experimental out-of-plane deformation is observed to be approximately 1/3 of the depth of the beam, while the maximum FEM out-of-plane deformation was at the mid-height of the beam. This minor discrepancy is due to the fact that the initial imperfection governs the web crippling response of the beam section. The initial imperfection imposed to the web had its maximum amplitude at mid-height, therefore it is not surprising that the maximum out-of-plane deformation is obtained at the same location.

Table 4.7

Summary of the finite element analyses with different shear span-to-depth ratio.

Model Designation	Shear Span-to-Depth Ratio	FEM Failure Load, R_{FEA} (kips)
FEA-4 <i>a</i>	0.669	46.24
FEA-4 <i>b</i>	1.39	48.47
FEA-7 <i>a</i>	0.644	61.53
FEA-7 <i>b</i>	1.49	67.18

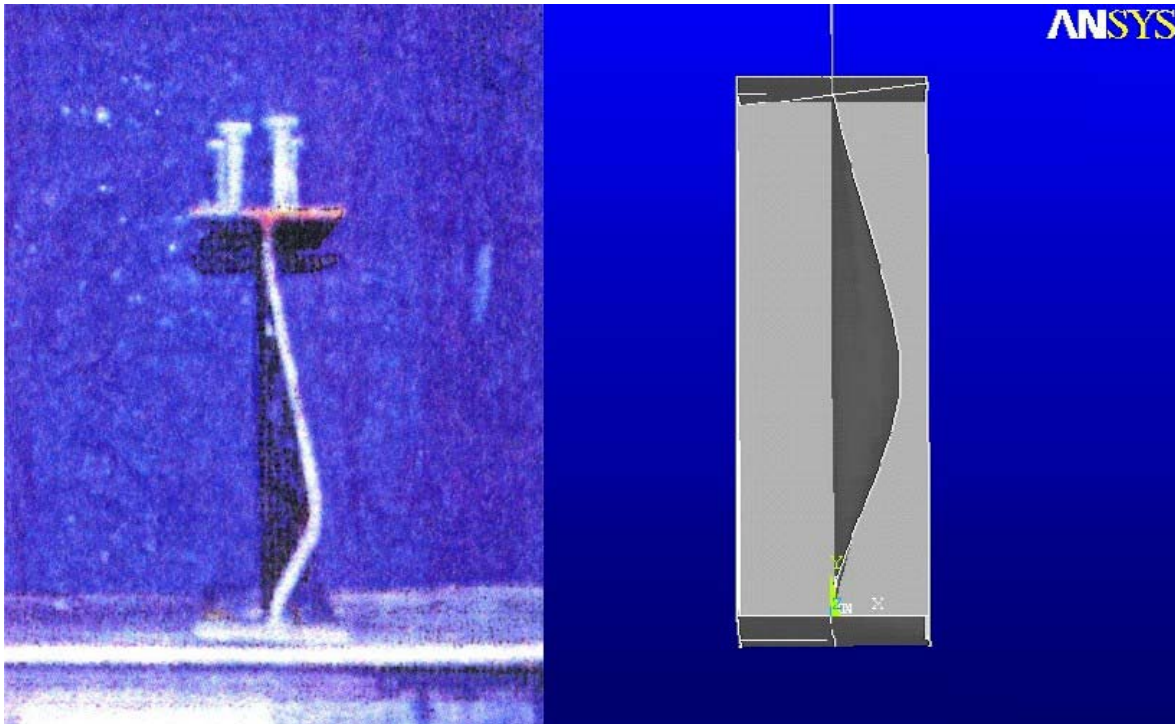


Figure 4.31 Comparison between the experimental and FEM web crippling failure mode shapes.

Figure 4.32 shows the results of the web crippling failure load-to-AISC ratio versus the bearing-to-depth ratio. It can be seen that, in general, the finite element results obtained in the parametric analysis were slightly higher than the 1999 AISC LRFD web crippling equation (K1-5b). Only two finite element results were lower than the predictions of the web crippling equation. These results are for the models FEA-SC-2*d* and FEA-SC-2*e*. Also, it can be seen that there is a tendency for the FEM failure load-to-AISC load ratio to decrease with increasing N/d ratio except for models FEA-7*c* and FEA-SC-2*f* within their respectively series. This tendency could be due to the fact that web imperfections govern the web crippling mode of the beam and thus influence the web crippling strength.

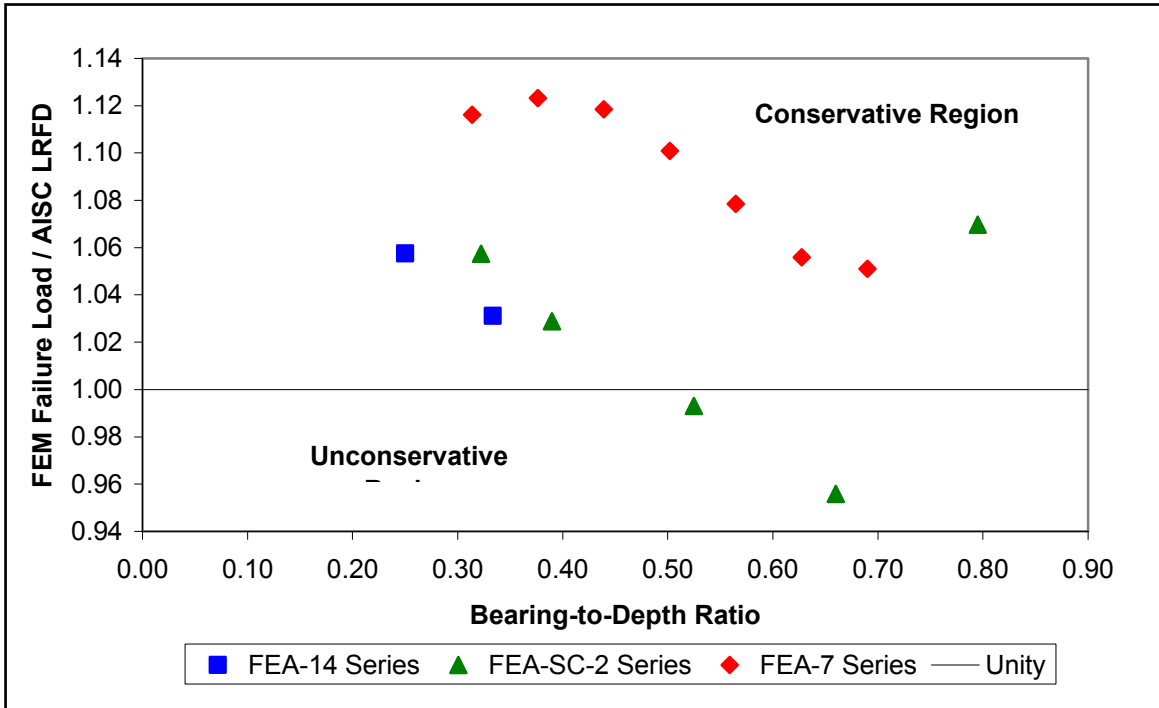


Figure 4.32 FEM failure load-to-AISC load ratio versus bearing-to-depth ratio.

Figures 4.33 to 4.35 show the accuracy of the 1999 AISC LRFD web crippling design equation for large bearing-to-depth ratios. It can be seen that the web crippling strength of W-sections is predicted by the 1999 AISC LRFD web crippling equations. However, it is conservative for thicker webs and for very large bearing-to-depth ratio as observed in the results obtained from the FEA-7x series and FEA-SC-2f, respectively.

Web crippling was the failure mode in every finite element model. The majority of the analyses was done within the FEA-7x and FEA-SC-2x series because the flexural capacity of these series was such that the bearing length could be increased greatly keeping the shear span-to-depth ratio greater than 1.0 and preventing bending failure at midspan. Only two analyses were done within the FEA-14x series because the bearing length could not be increased further without either having the shear span-to-depth ratio less than 1.0 or having a failure mode other than web crippling, such as flexural bending.

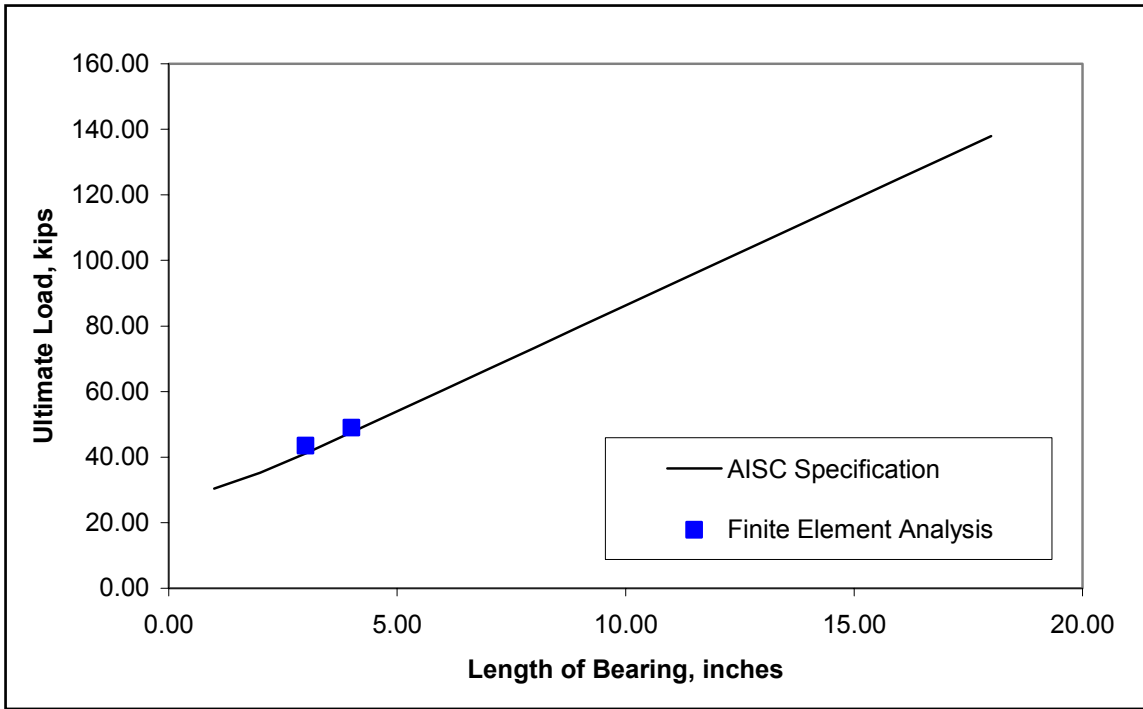


Figure 4.33 Prediction accuracy of the 1999 AISC LRFD web crippling equations on a W12x16 section.

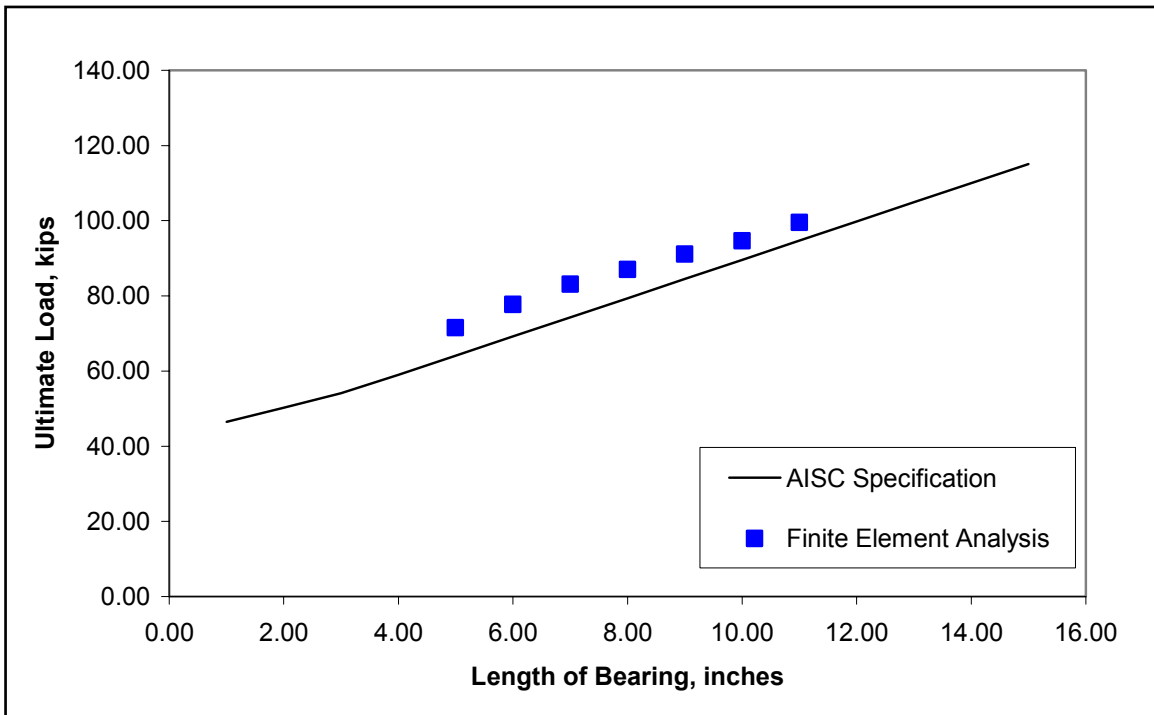


Figure 4.34 Prediction accuracy of the 1999 AISC LRFD web crippling equations on a W16x31 section.

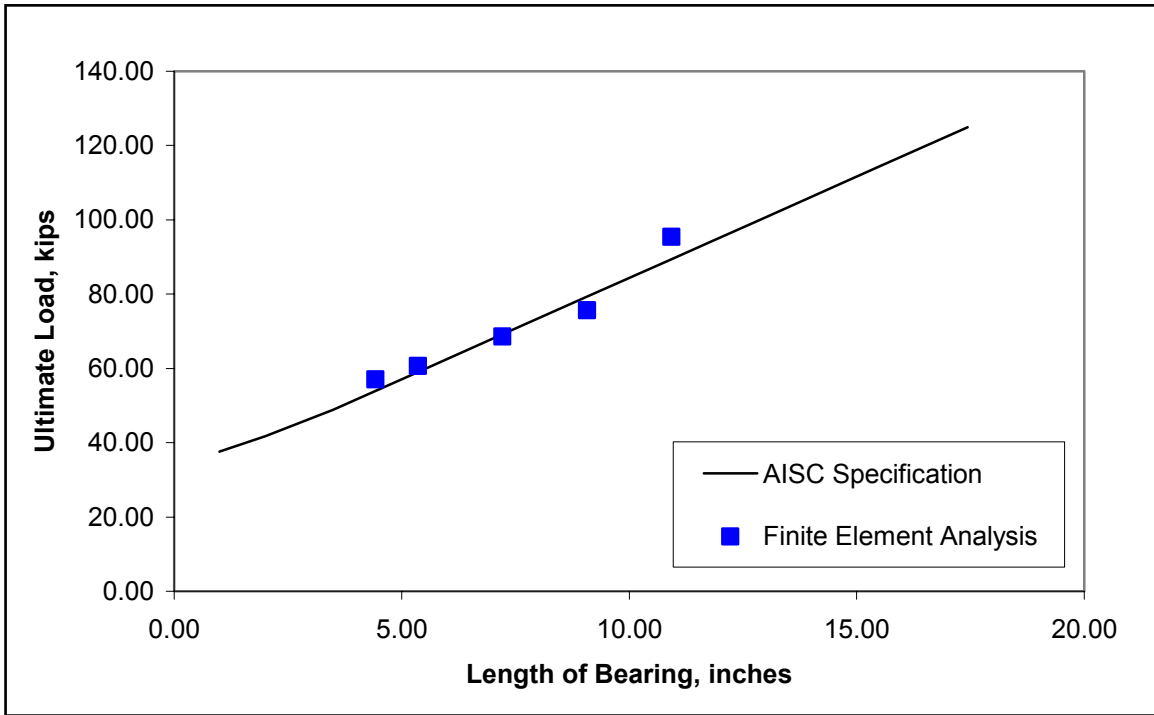


Figure 4.35 Prediction accuracy of the 1999 AISC LRFD web crippling equations on a W14x22 section.

CHAPTER 5

SUMMARY AND CONCLUSIONS

5.1 Summary

The primary objective of this study was to analytically investigate the web crippling strength of I-shape steel beams for large bearing-to-depth ratios on realistic span beams, and compare those results with the 1999 AISC LRFD web crippling equation (K1-5b). The commercial finite element package ANSYS 6.0 was used to model the steel beams and the connections.

The numerical simulations consisted of two main stages; the validation stage and the analysis stage. The first stage of this study consisted of validating the characteristics of the finite element models against experimental data. The experimental data from Elgaaly and Salkar (1991), and Bryant (1993), presented in Chapter 2, were used for this purpose. The second stage of the study consisted of performing a parametric analysis on those models that satisfactorily predicted the experimental failure load. The bearing-to-depth ratio was gradually increased to investigate the web crippling strength of the steel beams.

A total of twenty-one finite element models including geometric and material nonlinearities were created and analyzed. Seven of these models were used in the validation stage of this study, while the remaining fourteen were used to investigate the web crippling strength of the steel beams for different bearing-to-depth ratios.

The bearing-to-depth ratios in this study ranged from 0.250 to 0.690. Hot-rolled W12x16 sections were analyzed with bearing-to-depth ratios of 0.250 and 0.334. W16x31 sections were analyzed with bearing-to-depth ratios ranging from 0.314 to 0.690, and W14x22 sections using steel-concrete composite design were analyzed with bearing-to-depth ratios ranging from 0.322 to 0.795.

5.2 Conclusions

The finite element models developed in this study are capable of predicting the experimental failure load of steel beams due to web crippling failure. Good agreement was found between the FEM and theoretical load-deflection curves as well as the experimental failure load. The greatest difference of 5.37% was found in the validation model FEA-4a. However, this model was not used in the parametric stage. The FEM failure load of those validation models that were used in the second stage of this study differed from the experimental failure load by less than 1.25%.

Based on the results obtained in the parametric analyses, it was found that the 1999 AISC LRFD web crippling design equation (K1-5b) is conservative for stocky webs. The predictions of the equation were lower than the finite element results for a W16x31 section. The equation was also conservative when a very large bearing-to-depth ratio was used as demonstrated by the model FEA-SC-2f. A tendency for the FEM failure load-to-AISC load ratio to decrease with increasing bearing-to-depth, N/d , ratio was found. However, there is still a reason to believe that the web crippling strength of the steel beams increases with increasing N/d ratio. The geometric imperfection defined in the models seemed to govern the web crippling failure mode. This could have an influence on the web crippling strength of the models and thus show this tendency. It is important to point out that most of the web crippling shapes at failure were similar to their initial shape imperfection with the maximum out-of-plane deformation located at mid-height. The only model that showed a different behavior was the model FEA-SC-2f. As a result, this model carried 6.97% more load than predicted by the 1999 AISC LRFD web crippling equation deviating from the tendency the FEM failure load-to-AISC load ratio to decrease with increasing N/d ratio in the FEA-SC-2x series.

The finite element models FEA-7a and FEA-4a demonstrate that direct compression failure is the main mode of failure when the shear span of those models is less than the depth of the beam section. This observation was also reported by Ketchum and Draffin who tested several lightweight steel beams for failure at the support with two

different loading configurations. They reported that the 6 in. and 10 in. specimens loaded with a shear span-to-depth ratio greater than 1.0 carried about 10% greater strength than those specimens loaded with a shear span-to-depth ratio less than 1.0. These results question most of the results from the experimental study conducted by Elgaaly and Salkar (1991), where thirteen out of the twenty-seven specimens were loaded at a distance from the face of the support less than 3/4th of the depth of the sections. The failure of those specimens might be due to direct compression, not web crippling.

REFERENCES

AISC (1986), *Specification for Structural Steel Buildings, Load and Resistance Factor Design*, 1st American Institute of Steel Construction, Chicago, IL.

AISC (1993), *Specification for Structural Steel Buildings, Load and Resistance Factor Design*, 2nd American Institute of Steel Construction, Chicago IL.

AISC (1999), *Specification for Structural Steel Buildings, Load and Resistance Factor Design*, American Institute of Steel Construction, Chicago IL.

ANSYS (2001), *Documentation and Theory Reference*, Version 6.0, ANSYS, Inc., Canonsburg, PA.

Bergfelt, A., (1976), "The Behavior and Design of Slender Webs Under Partial Edge Loading" *Steel Plated Structures: An International Symposium*, Crosby Lockwood Staples Ltd, London, England, pp. 486-502.

Bryant, C. L. (1993), "Web Crippling of Hot-Rolled Beams at Stiffened-Seat Connections", *Master's Thesis*, Virginia Polytechnic Institute and State University, Blacksburg, VA.

Elgaaly, M. (1983), "Web Under Compressive Edge Loads". *Engineering Journal*, AISC, Fourth Quarter, pp. 153-171.

Elgaaly, M. and Salkar, R. K. (1991), "Web Crippling Under Compressive Edge Loading" *Proceedings*, 1991 National Steel Construction Conference, Washington, D.C., June 5-7, pp. 7-1 through 7-21.

Graciano, C. A., and Edlund B. (2002), "Nonlinear FE Analysis of Longitudinally Stiffened Girder Webs Under Patch Loading" *Journal of Constructional Steel Research*, Vol. 58, pp. 1231–1245.

Granath P. (1997), "Behavior of Slender Plate Girders Subjected to Patch Loading" *Journal of Constructional Steel Research*, Vol. 42, No. 1, pp. 1-19.

Ketchum M. S., and Draffin, J. O. (1932), "Strength of Light I-Beams" *Bulleting No. 24*, University of Illinois Engineering Experimental Station, Urbana, IL.

RISA-3D (2001) *User's Manual*, Version 4.5, RISA Technologies, Foothill Ranch, CA.

Roberts, T. M. (1981) "Slender Plate Girder Subjected to Edge Loading", *Proceedings of the Institute of Civil Engineers*, Part 2, 71, pp. 805-819.

Roberts, T. M. and Rockey, K. C. (1979), "A Mechanism Solution for Predicting the Collapse Loads of Slender Plate Girders When Subjected to In-Plane Patch Loading" *Proceedings*, Institute of Civil Engineers, Part 2, Vol. 67, London, England, 155-175.

Rockey, K.C., (1976), "The Design of Web Plates for Plate and Box Girders – A State of the Art Report", *Steel Plated Structures: An International Symposium*, Crosby Lockwood Staples Ltd, London, England, pp. 459-485.

Tryland, T., Hopperstad, O. S., and Langseth M. (1999), "Steel Girders Subjected to Concentrated Loading-Validation of Numerical Simulations" *Journal of Constructional Steel Research*, Vol. 50, pp. 199–216.

Tryland, T., Hopperstad, O. S., and Langseth M. (2001), "Finite-Element Modeling of Beams Under Concentrated Loading" *Journal of Structural Engineering*, ASCE, Vol. 127, No. 2, pp. 176-185.

APPENDIX A

CREATING AND ANALYZING THE FE MODEL

This section presents the procedure employed to create, analyze, and view the results of the nonlinear finite element model by using the ANSYS' Graphical User Interface. The purpose of this section is also to provide with an example problem that can be followed by others in order to get familiar with the ANSYS program, Version 6.0.

Problem Description

A W14x22 steel beam is loaded by means of a 100 kips force located 22 in. from the far end of the supports. The load is applied initially in increments of 5 kips, whenever the material is reaching the yield point the load is then applied in increments of 2 kips. The objective is to determine the ultimate capacity of the web due to crippling failure. The following dimensions are used for this problem:

Flange Width* = 5.12 in.

Flange Thickness* = 0.329 in.

Web Depth = 13.481 in. (from centerlines of the flanges)

Web Thickness* = 0.237 in.

Stiffener Thickness = 1.0 in.

Location of stiffeners = 22.0 in. from the end of the supports.

Span Length = 144 in.

Length of Bearing Block = 4.0 in.

Modulus of Elasticity = 29,000 ksi.

Yield Stress = 50.0 ksi.

Tangent Modulus = 2,900 ksi.

Specific Weight Density = 0.000284 kips/in³

* Dimensions properties reported by Elgaaly and Salkar (1991).

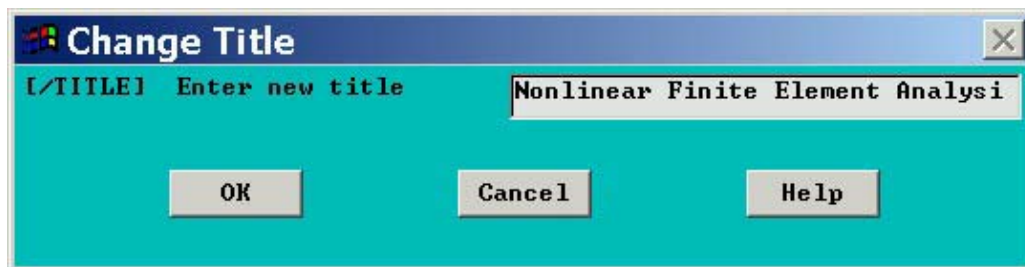
Applied Load = 100 kips

Load Location = 22.0 in. from the end of the supports.

Initial Condition Function = $0.25 * \text{COS}(0.233 * H)$, where H is measure from mid-depth of the beam.

1. Specify an Analysis Title

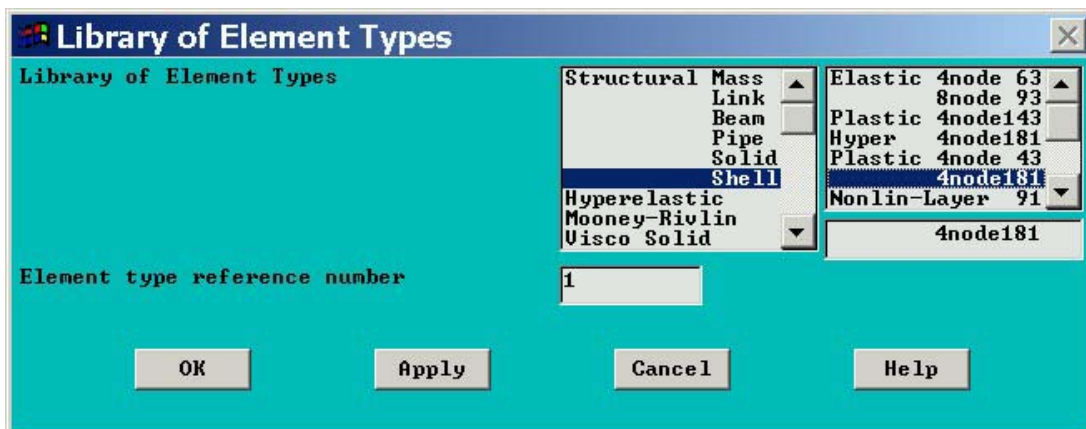
- 1.1. Choose menu path **Utility Menu>File>Change Title**. The following window will appear.



- 1.2. Type the text "Nonlinear Finite Element Analysis of a W14x22" and click on **OK**.

2. Define the Element Types

- 2.1. Choose menu path **Main Menu>Preprocessor>Element Type>Add/Edit/Delete**.
- 2.2. Click on **Add**. The Library of Element Types dialog box appears.
- 2.3. In the scroll box on the left, click once on "**Shell**".
- 2.4. In the scroll box on the right, click once on "**Plastic 4node 181**".



- 2.5. Click on **OK** to define it as element type 1. The Library of Element Types dialog box closes.

2.6. Click on **Close** on the Element Types dialog box.

3. Define Element Real Constants

3.1. Choose menu path **Main Menu>Preprocessor>Real Constants>Add/Edit/Delete.**

3.2. Click on **Add**. The Element Type for Real Constants dialog box appears.

3.3. Click on **Ok**. The Real Constants Set Number 1, for Shell 181 dialog box appears.

Element Type Reference No. 1	
Real Constant Set No.	1
Real Constants for SHELL181	
Shell thickness at node I TK(I)	0.237
at node J TK(J)	
at node K TK(K)	
at node L TK(L)	
Element X-axis rotation THETA	
Added mass/unit area ADMSUA	
Transverse shear stiffness E11	
Transverse shear stiffness E22	
Transverse shear stiffness E12	
Drill stiff scale factor DRILL	
Hourglass scale factor MEMBRANE	
Hourglass scale factor BENDING	

OK Apply Cancel Help

3.4. Enter 0.237 for the Shell thickness at node I, TK(I). Click on **Apply**.

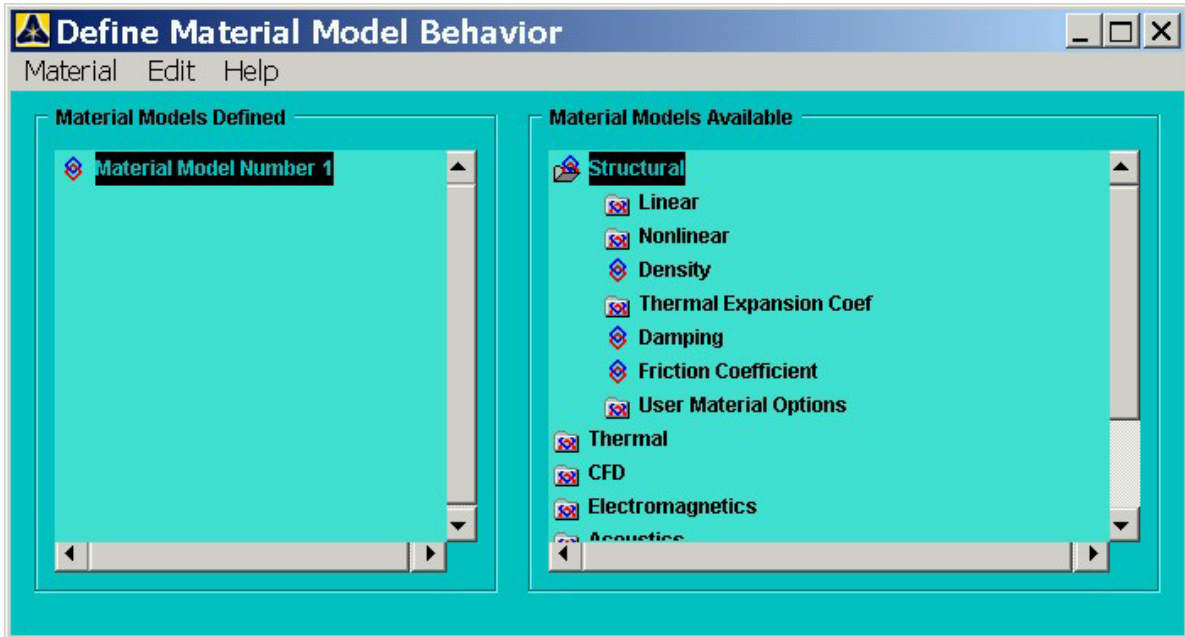
3.5. Enter 2 for the Real Constant Set No, and 0.329 for the Shell thickness at node I, TK(I). Click on **Apply**.

3.6. Enter 3 for the Real Constant Set No, and 1.0 for the Shell thickness at node I, TK(I). Click on **Apply**.

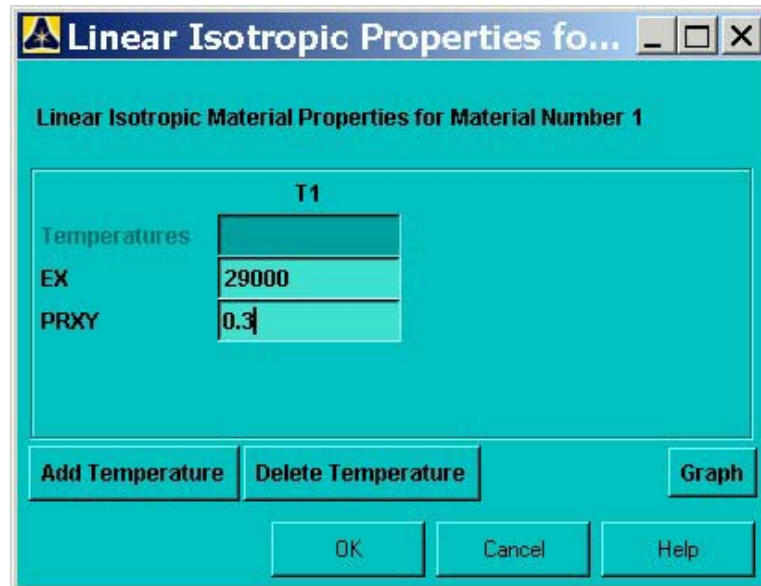
3.7. Close the Real Constant dialog box.

4. Define Material Properties for Steel

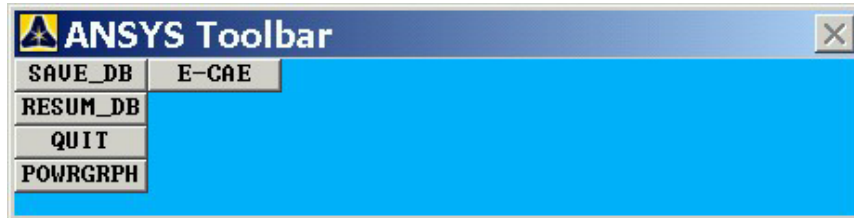
- 4.1. Choose menu path **Main Menu>Preprocessor>Material Props>Material Models**. The Define Material Model Behavior dialog box appears.
- 4.2. In the scroll box on the right, double click on **Structural>Linear>Elastic>Isotropic**.



- 4.3. The Linear Isotropic Properties for Model Number 1 dialog box appear. Type 29000 for **EX**, and 0.3 for **PRXY**. Click **OK**



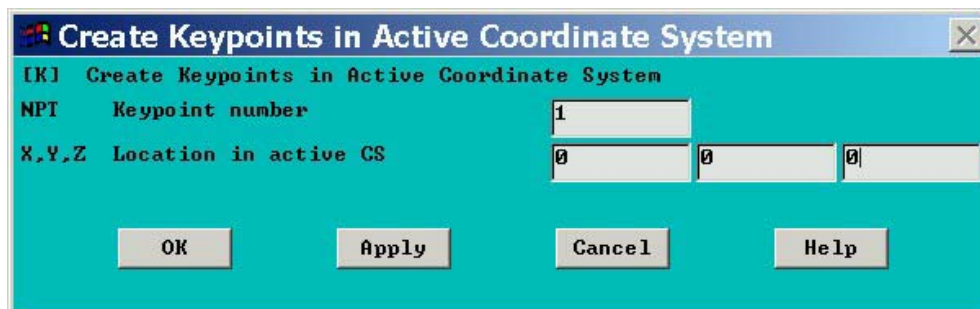
- 4.4. Click on **Structural>Nonlinear>Inelastic>Rate Independent>Isotropic Hardening Plasticity>Mises Plasticity>Bilinear**. The Bilinear Isotropic Hardening for Model Number 1 dialog box appear. Type 50.0 for **Yield Stss**, and 2900 for **Tang Mod**. Click **OK**.
- 4.5. Click on **Structural>Density**. The Density for Material Number 1 dialog box appears.
- 4.6. Type 0.000284 for **Dens**. Click **OK**.
- 4.7.. Click **Material>Exit**.
- 4.9. Click on **SAVE_DB** on the ANSYS Toolbar.



5. Creating the Model Geometry

5.1. Create Keypoints Along a Path

- 5.1.1. Choose menu path **Main Menu>Preprocessor>-Modeling-Create>Keypoints>In Active CS**. The Create Keypoints in Active Coordinate System dialog box appears.
- 5.1.2. Enter 1 for the keypoint number. Type a 0 in each of the **X,Y,Z** location fields. Click on **Apply**.



- 5.1.3. Enter 2 for the keypoint number. Type 2.56,0,0 for the **X,Y,Z** location respectively. Click on **Apply**.
- 5.1.4. Enter 3 for the keypoint number. Type 5.12,0,0 for the **X,Y,Z** location respectively. Click on **Apply**.
- 5.1.5. Enter 4 for the keypoint number. Type 0,13.481,0 for the **X,Y,Z** location respectively. Click on **Apply**.
- 5.1.6. Enter 5 for the keypoint number. Type 2.5,13.481,0 for the **X,Y,Z** location respectively. Click on **Apply**.

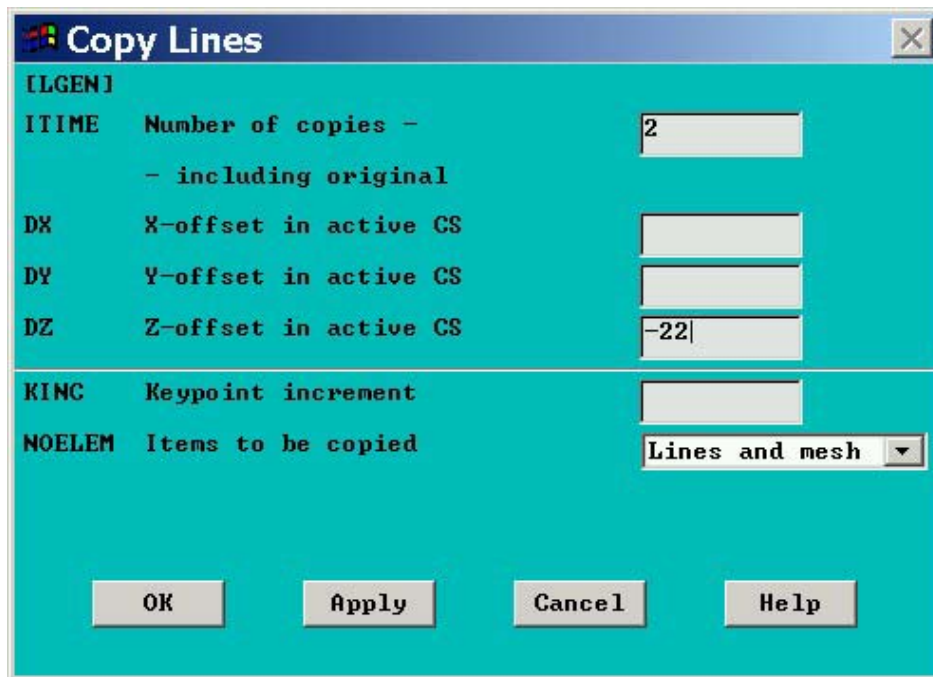
5.1.7. Enter 6 for the keypoint number. Type 5,13.481,0 for the **X,Y,Z** location respectively. Click on **OK**.

5.2. Create Lines Along a Path

- 5.2.1. Choose menu path **Main Menu>Preprocessor>-Modeling>Create>-Lines-Lines>Straight Line**. The Create Straight Line picking menu appears.
- 5.2.2. Click once on keypoint 1 and 2 to create a line between keypoint 1 and 2.
- 5.2.3. Click once on keypoint 2 and 3 to create a line between keypoint 2 and 3.
- 5.2.4. Click once on keypoint 4 and 5 to create a line between keypoint 4 and 5.
- 5.2.5. Click once on keypoint 5 and 6 to create a line between keypoint 5 and 6.
- 5.2.6. Click once on keypoint 5 and 2 to create a line between keypoint 5 and 2.
- 5.2.7. Click on **Ok** in the Create Straight Line picking menu.
- 5.2.8. Choose menu path **Utility Menu>PlotCtrls>Numbering**. The Plot Numbering Controls dialog box appears.
- 5.2.9. Click the Line numbers radio button to **On**. Click on **OK**.
- 5.2.10. Choose menu path **Utility Menu>Plot>Lines**. The numbered lines appear in the ANSYS Graphical window.

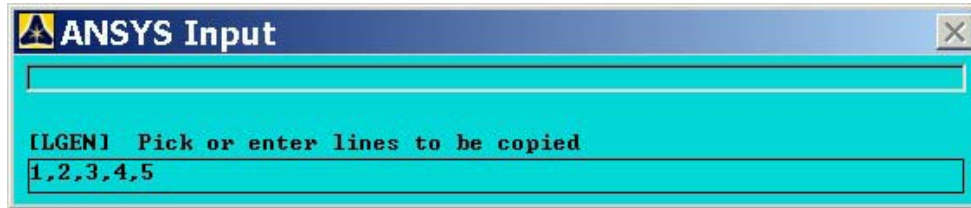
5.3. Copy Lines Along a Path

- 5.3.1. Choose menu path **Main Menu>Preprocessor>-Modeling-Copy>Lines**. The Copy Lines picking menu appears.
- 5.3.2. Click on **Pick All** in the Copy Lines picking menu. The Copy Lines dialog box appears.



5.3.3. Enter -22 for **DZ, Z-offset in active CS** location field. Click on **Apply**.

- 5.3.4. Type 1,2,3,4,5 in the **ANSYS Input**. Press **Enter** in the keyboard, and click **OK** on the Copy Lines picking menu.



- 5.3.5. The Copy Lines dialog box appears. Enter -72 for **DZ, Z-offset in active CS** location field. Click on **Apply**.
- 5.3.6. Type 1,2,3,4,5 in the **ANSYS Input**. Press **Enter** in the keyboard, and click **OK** in the Copy Lines picking menu.
- 5.3.7. The Copy Lines dialog box appears. Enter -122 for **DZ, Z-offset in active CS** location field. Click on **Apply**.
- 5.3.8. Type 1,2,3,4,5 in the **ANSYS Input**. Press **Enter** in the keyboard, and click **OK** in the Copy Lines picking menu.
- 5.3.9. The Copy Lines dialog box appears. Enter -144 for **DZ, Z-offset in active CS** location field. Click on **Ok**.

5.4. Create Additional Lines Along a Path

- 5.4.1. Choose menu path **Utility Menu>PlotCtrls>Pan/Zoom/Rotate**. The Pan-Zoom-Rotate dialog box appear.
- 5.4.2. Click on **"Iso"** to generate an isometric view. Click on **Close**.
- 5.4.3. Choose menu path **Utility Menu>PlotCtrls>Numbering**. The Plot Numbering Controls dialog box appears.
- 5.4.4. Click the Line numbers radio button to **Off**, and click the Keypoint numbers radio button to **On**. Click on **OK**.
- 5.4.5. Choose menu path **Main Menu>Preprocessor>-Modeling-Create>-Lines-Lines>Straight Line**. The Create Straight Line picking menu appears.

Note: If you have trouble reading the keypoint numbers in the ANSYS Graphic window, use the controls on the Pan-Zoom-Rotate dialog box (**Utility Menu>PlotCtrls>Pan/Zoom/Rotate**) to zoom in or zoom out.

- 5.4.6. Click once on keypoint 1 and 7 to create a line between keypoint 1 and 7
- 5.4.7. Click once on keypoint 2 and 8.
- 5.4.8. Click once on keypoint 3 and 9.
- 5.4.9. Click once on keypoint 4 and 10.
- 5.4.10. Click once on keypoint 5 and 11.
- 5.4.11. Click once on keypoint 6 and 12.
- 5.4.12. Click once on keypoint 7 and 13.
- 5.4.13. Click once on keypoint 8 and 14.
- 5.4.14. Click once on keypoint 9 and 15.
- 5.4.15. Click once on keypoint 10 and 16.

- 5.4.16. Click once on keypoint 11 and 17.
- 5.4.17. Click once on keypoint 12 and 18.
- 5.4.18. Click once on keypoint 13 and 19.
- 5.4.19. Click once on keypoint 14 and 20.
- 5.4.20. Click once on keypoint 15 and 21.
- 5.4.21. Click once on keypoint 16 and 22.
- 5.4.22. Click once on keypoint 17 and 23.
- 5.4.23. Click once on keypoint 18 and 24.
- 5.4.24. Click once on keypoint 19 and 25.
- 5.4.25. Click once on keypoint 20 and 26.
- 5.4.26. Click once on keypoint 21 and 27.
- 5.4.27. Click once on keypoint 22 and 28.
- 5.4.28. Click once on keypoint 23 and 29.
- 5.4.29. Click once on keypoint 24 and 30.
- 5.4.30. Click once on keypoint 7 and 10.
- 5.4.31. Click once on keypoint 9 and 12.
- 5.4.32. Click once on keypoint 19 and 22.
- 5.4.33. Click once on keypoint 21 and 24.
- 5.4.34. Click once on keypoint 25 and 28.
- 5.4.35. Click once on keypoint 27 and 30.
- 5.4.36. Click on **OK** on the Create Straight Line picking menu.

5.5. Create Areas Along a Path

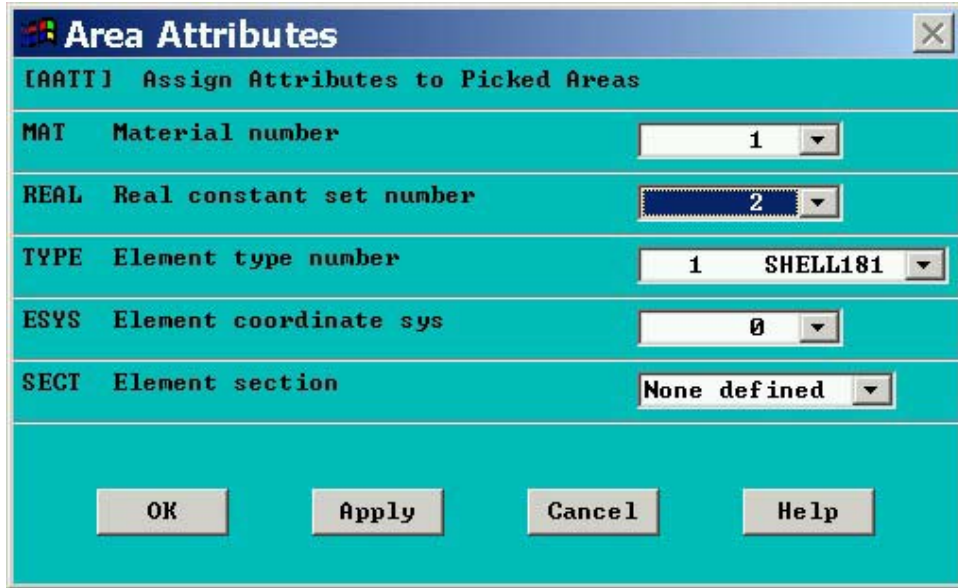
- 5.5.1. Choose menu path **Utility Menu>PlotCtrls>Numbering**. The Plot Numbering Controls dialog box appears.
- 5.5.2. Click the Keypoint numbers radio button to **Off**, and click the Line numbers radio button to **On**. Click on **OK**.
- 5.5.3. Choose menu path **Main Menu>Preprocessor>-Modeling>Create>-Areas-Arbitrary>By Lines**. The Create Areas by Lines picking menu appears.
- 5.5.4. Type 1,6,26,27 in the **ANSYS Input**. Press **Enter** in the keyboard, and click **Apply** on the Create Areas by Lines picking menu to create an area.
- 5.5.5. Type 2,7,27,28 in the **ANSYS Input**. Press **Enter** in the keyboard, and click **Apply** on the Create Areas by Lines picking menu.
- 5.5.6. Type 3,8,29,30 in the **ANSYS Input**. Press **Enter** in the keyboard, and click **Apply** on the Create Areas by Lines picking menu.
- 5.5.7. Type 4,9,30,31 in the **ANSYS Input**. Press **Enter** in the keyboard, and click **Apply** on the Create Areas by Lines picking menu.
- 5.5.8. Type 6,11,32,33 in the **ANSYS Input**. Press **Enter** in the keyboard, and click **Apply** on the Create Areas by Lines picking menu.
- 5.5.9. Type 7,12,33,34 in the **ANSYS Input**. Press **Enter** in the keyboard, and click **Apply** on the Create Areas by Lines picking menu.
- 5.5.10. Type 8,13,35,36 in the **ANSYS Input**. Press **Enter** in the keyboard, and click **Apply** on the Create Areas by Lines picking menu.
- 5.5.11. Type 9,14,36,37 in the **ANSYS Input**. Press **Enter** in the keyboard, and click **Apply** on the Create Areas by Lines picking menu.

- 5.5.12. Type 11,16,38,39 in the **ANSYS Input**. Press **Enter** in the keyboard, and click **Apply** on the Create Areas by Lines picking menu.
- 5.5.13. Type 12,17,39,40 in the **ANSYS Input**. Press **Enter** in the keyboard, and click **Apply** on the Create Areas by Lines picking menu.
- 5.5.14. Type 13,18,41,42 in the **ANSYS Input**. Press **Enter** in the keyboard, and click **Apply** on the Create Areas by Lines picking menu.
- 5.5.15. Type 16,21,44,45 in the **ANSYS Input**. Press **Enter** in the keyboard, and click **Apply** on the Create Areas by Lines picking menu.
- 5.5.16. Type 17,22,45,46 in the **ANSYS Input**. Press **Enter** in the keyboard, and click **Apply** on the Create Areas by Lines picking menu.
- 5.5.17. Type 18,23,47,48 in the **ANSYS Input**. Press **Enter** in the keyboard, and click **Apply** on the Create Areas by Lines picking menu.
- 5.5.18. Type 19,24,48,49 in the **ANSYS Input**. Press **Enter** in the keyboard, and click **Apply** on the Create Areas by Lines picking menu.
- 5.5.19. Type 5,10,27,30 in the **ANSYS Input**. Press **Enter** in the keyboard, and click **Apply** on the Create Areas by Lines picking menu.
- 5.5.20. Type 10,15,33,36 in the **ANSYS Input**. Press **Enter** in the keyboard, and click **Apply** on the Create Areas by Lines picking menu.
- 5.5.21. Type 15,20,39,42 in the **ANSYS Input**. Press **Enter** in the keyboard, and click **Apply** on the Create Areas by Lines picking menu.
- 5.5.22. Type 20,25,45,48 in the **ANSYS Input**. Press **Enter** in the keyboard, and click **Apply** on the Create Areas by Lines picking menu.
- 5.5.23. Type 6,8,10,50 in the **ANSYS Input**. Press **Enter** in the keyboard, and click **Apply** on the Create Areas by Lines picking menu.
- 5.5.24. Type 7,9,10,51 in the **ANSYS Input**. Press **Enter** in the keyboard, and click **Apply** on the Create Areas by Lines picking menu.
- 5.5.25. Type 16,18,20,52 in the **ANSYS Input**. Press **Enter** in the keyboard, and click **Apply** on the Create Areas by Lines picking menu.
- 5.5.26. Type 17,19,20,53 in the **ANSYS Input**. Press **Enter** in the keyboard, and click **Apply** on the Create Areas by Lines picking menu.
- 5.5.27. Type 21,23,25,54 in the **ANSYS Input**. Press **Enter** in the keyboard, and click **Apply** on the Create Areas by Lines picking menu.
- 5.5.28. Type 22,24,25,55 in the **ANSYS Input**. Press **Enter** in the keyboard, and click **Ok** on the Create Areas by Lines picking menu.
- 5.5.29. Click on **SAVE_DB** on the ANSYS Toolbar.

5.6. Define Attributes

- 5.6.1. Choose menu path **Utility Menu>PlotCtrls>Numbering**. The Plot Numbering Controls dialog box appears.
- 5.6.2. Click the Line numbers radio button to **Off**, and click the Area numbers radio button to **On**. Click on **OK**.
- 5.6.3. Choose menu path **Main Menu>Preprocessor>-Attributes-Define>Picked Areas**. The Area Attributes picking menu appears.
- 5.6.4. Type 17,18,19,20 in the **ANSYS Input**. Press **Enter** in the keyboard, and click **Ok** on the Areas Attributes picking menu. The Area Attributes dialog box appears. Click on **Apply**.

5.6.5. Type 1,2,3,4,5,6,7,8,9,10,11,12,13,14,15,16 in the **ANSYS Input**. Press **Enter** in the keyboard, and click **Ok** on the Areas Attributes picking menu. The Area Attributes dialog box appears. Set the Real constant set number to 2, and Click on **Apply**.

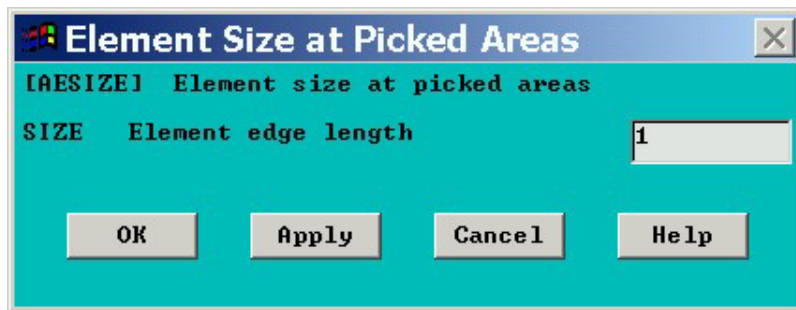


5.6.6. Type 21,22,23,24,25,26 in the **ANSYS Input**. Press **Enter** in the keyboard, and click **Ok** on the Areas Attributes picking menu. The Area Attributes dialog box appears. Set the Real constant set number to 3, and Click on **Ok**.

5.7. Set Mesh Density

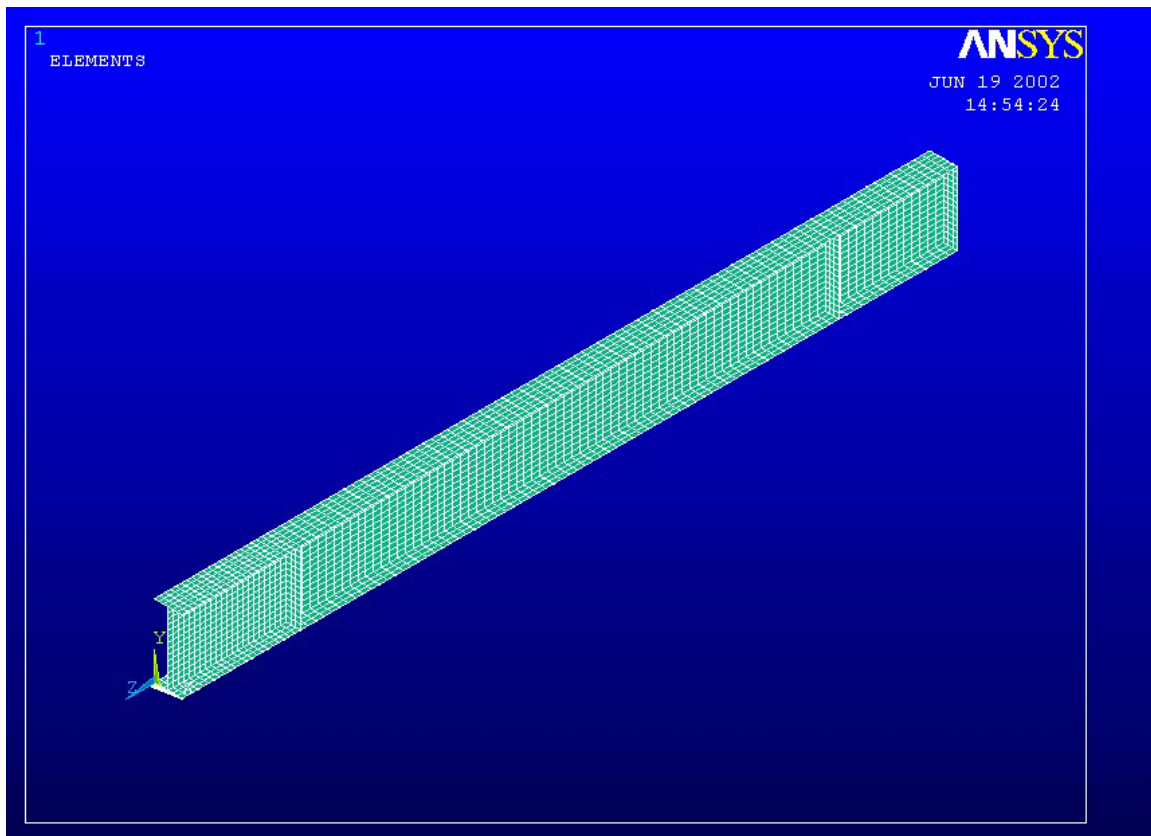
5.7.1. Choose menu path **Main Menu>Preprocessor>-Meshing-Size Cntrls->ManualSize-Areas->Picked Areas**. The Element Size at Picked Areas picking menu appears.

5.7.2. Type 1,2,3,4,17,21,22 in the **ANSYS Input**. Press **Enter** in the keyboard, and click **Ok** on the Element Size at Picked Areas picking menu. The Element Size at Picked Areas dialog box appears. Enter 1 for SIZE, Element edge length in the Element Size at Picked Areas location field. Click on **Apply**.



5.7.3. Type 5,6,7,8,9,10,11,12,13,14,15,16,18,19,20,21,22,23,24,25,26 in the **ANSYS Input**. Press **Enter** in the keyboard, and click **Ok** on the Element Size at Picked

- Areas picking menu. The Element Size at Picked Areas dialog box appears. Enter 1.5 for SIZE, Element edge length in the Element Size at Picked Areas location field. Click on **Ok**.
- 5.7.4. Choose menu path **Main Menu>Preprocessor>-Meshing-Mesher Opts**. The Mesher Option dialog box appears. Click on the Mapped radio button to select it. Click on **OK**. The Set Element Shape dialog box appears. Verify that Quad is currently selected on the 2D Shape Key, and click on **OK**.
- 5.7.5. Choose menu path **Main Menu>Preprocessor>-Meshing-Mesh>-Areas-Mapped>3or 4 sided**. The Mesh Area picking menu appears. Click on **Pick All**. The following model shall appear in the ANSYS Graphics Window.



- 5.7.6. Click on **SAVE_DB** on the ANSYS Toolbar.

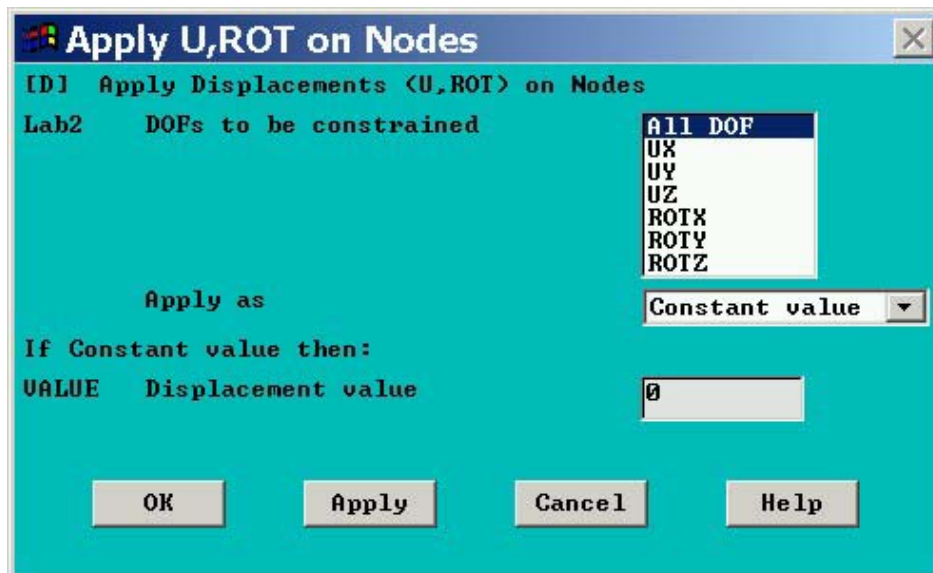
6. Apply the Constraints and Initial Conditions

6.1. Constraints

- 6.1.1. Choose menu path **Utility Menu>Select>Entities**. The Select Entities dialog box appears. In the top drop down menu, select **Nodes**. In the second drop down menu, select **By Location**.
- 6.1.2. Click on the **Y Coordinates** radio button to select it, enter 0 for Min, Max, and click on **Ok**.



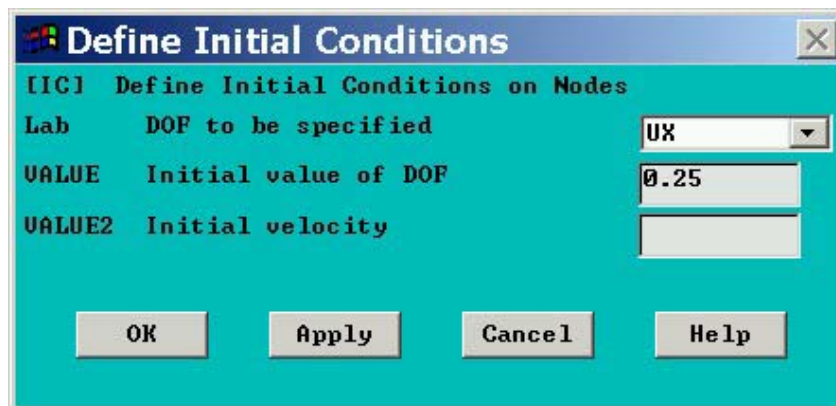
- 6.1.3. Choose menu path **Main Menu>Preprocessor>Loads>-Loads-Apply>-Structural-Displacements>On nodes**. The Apply U, ROT on Nodes picking menu appears. Click on the Box button ration to select it.
- 6.1.4. Select the first five nodes on the bottom left end of the section. Click on **Ok** on the Apply U, ROT on Nodes picking menu.
- 6.1.5. The Apply U,ROT on Nodes dialog box appears. Select **All DOF**, and type 0 for the Displacement value. Click on **Apply**.



- 6.1.6. Click on the Box button ration to select it on the Apply U, ROT on Nodes picking menu. Select the last nodes on the bottom right end of the section. Click on **Ok** on the Apply U, ROT on Nodes picking menu. The Apply U,ROT on Nodes dialog box appears. Click on **All DOF** to deselect it, click on UX, U, and type 0 for the Displacement value. Click on **Ok**.
- 6.1.7. Choose menu path **Utility Menu>Select>Everything**.
- 6.1.8. Choose menu path **Utility Menu>Select>Entities**. The Select Entities dialog box appears. Verify that the **Y Coordinates** radio button is selected, enter 13.481 for Min, Max, and click on **Ok**.
- 6.1.9. Choose menu path **Main Menu>Preprocessor>Loads>-Loads-Apply>-Structural-Displacements>On nodes**. The Apply U, ROT on Nodes picking menu appears. Click on **Pick All**. The Apply U,ROT on Nodes dialog box appears. Click on **UY** to deselect it, type 0 for the Displacement value. Click on **Ok**.
- 6.1.10. Choose menu path **Utility Menu>Select>Everything**.

6.2. Initial Conditions

- 6.2.1. Choose menu path **Main Menu>Preprocessor>Loads>-Loads-Apply>-Initial Condit'n>Define**. The Define Initial Conditions picking menu appears.
- 6.2.2. Type 1504,1517,1530,1543 in the **ANSYS Input**. Press **Enter** in the keyboard, and click **Ok** on the Define Initial Conditions picking menu. The Define Initial Conditions dialog box appears. In the top drop down menu, select **UX** and type 0.25 for the **Initial value of DOF**. Click on **Apply**.



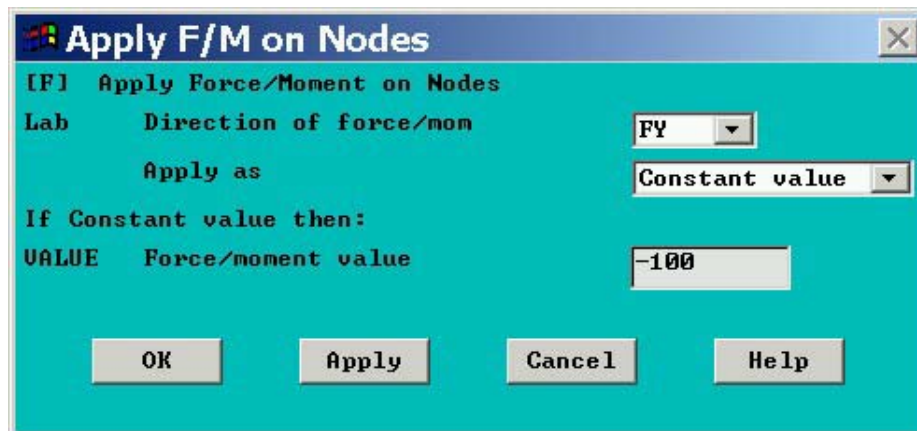
- 6.2.3. Type 1503,1504,1516,1518,1529,1531,1542,1544,1556 in the **ANSYS Input**. Press **Enter** in the keyboard, and click **Ok** on the Define Initial Conditions picking menu. The Define Initial Conditions dialog box appears. Type 0.24 for the Initial value of DOF. Click on **Apply**.
- 6.2.4. Type 1502,1506,1515,1519,1528,1532,1541,1545,1555,1557,1569 in the **ANSYS Input**. Press **Enter** in the keyboard, and click **Ok** on the Define Initial Conditions picking menu. The Define Initial Conditions dialog box appears. In

- the top drop down menu, select **UX** and type 0.22 for the **Initial value of DOF**. Click on **Apply**.
- 6.2.5. Type 1501,1507,1514,1520,1527,1533,1540,1546,1558,1554,1568,1570, 1582 in the **ANSYS Input**. Press **Enter** in the keyboard, and click **Ok** on the Define Initial Conditions picking menu. The Define Initial Conditions dialog box appears. In the top drop down menu, select **UX** and type 0.19 for the **Initial value of DOF**. Click on **Apply**.
- 6.2.6. Type 1500,1508,1513,1521,1526,1534,1539,1547,1553,1559,1567,1571, 1581,1583,1595 in the **ANSYS Input**. Press **Enter** in the keyboard, and click **Ok** on the Define Initial Conditions picking menu. The Define Initial Conditions dialog box appears. Type 0.15 for the Initial value of DOF. Click on **Apply**.
- 6.2.7. Type 1499,1509,1512,1522,1525,1535,1538,1548,1552,1560,1566,1572, 1580,1584,1594,1596,1608 in the **ANSYS Input**. Press **Enter** in the keyboard, and click **Ok** on the Define Initial Conditions picking menu. The Define Initial Conditions dialog box appears. In the top drop down menu, select **UX** and type 0.10 for the **Initial value of DOF**. Click on **Apply**.
- 6.2.8. Type 1498,1510,1511,1523,1524,1536,1537,1551,1561,1565,1573,1579, 1585,1593,1597,1607,1609,1621 in the **ANSYS Input**. Press **Enter** in the keyboard, and click **Ok** on the Define Initial Conditions picking menu. The Define Initial Conditions dialog box appears. In the top drop down menu, select **UX** and type 0.04 for the **Initial value of DOF**. Click on **Ok**.
- 6.2.9. Click on **SAVE_DB** on the ANSYS Toolbar.

7. Apply the Loads

7.1 Concentrated Loads

- 7.1.1. Choose menu path **Main Menu>Preprocessor>Loads>-Loads-Apply>-Structural-Force/Moment>On nodes**. The Apply F/M on Nodes dialog box appears. Type 166,1037 in the **ANSYS Input**. Press **Enter** in the keyboard, and click **Ok** on the Apply F/M on Nodes picking menu. The Apply F/M on Nodes dialog box appears. In the top drop down menu, select **FY**, and type -100 for the **Force/moment value**. Click on **Ok**.



7.2. Gravity Loads

- 7.2.1. Choose menu path **Main Menu>Preprocessor>Loads>-Loads-Apply>-Structural-Gravity**. The Apply (Gravitational) Acceleration dialog box appears. Type 1 for the **ACELY, Global Cartesian Y-comp**. Click on **Ok**.

Note: Since the specific weight density was defined previously for the steel material, the gravitational acceleration has to be defined as 1. Also note that a positive acceleration in the y direction stimulates gravity in the negative Y direction.

8. Set Solution Controls

- 8.1. Choose menu path **Main Menu>Solution>Unabridged>Analysis Options**. The Static or Steady-State Analysis dialog appears. Click on Large deform effect button ration to turn it on. In the Newton-Raphson option drop down menu, select **Full N-R**. In the Equation solver drop down menu, select **Sparse solver**. Finally, in the stress stiffness or prestress drop down menu, select **Stress stiff ON**. Click on **Ok**.

Static or Steady-State Analysis

Nonlinear Options

[NLGEOM] Large deform effects On

[NROPT] Newton-Raphson option Full N-R

Adaptive descent ON if necessary

Linear Options

[LUMPM] Use lumped mass approx? No

[EQSLU] Equation solver Sparse solver

Tolerance/Level -

- valid for all except Frontal and Sparse Solvers

Multiplier - 0

- valid only for Precondition CG

[PRECISION] Single Precision - Off

- valid only for Precondition CG

[MSAUE] Memory Save - Off

- valid only for Precondition CG

[PIUCHECK] Pivots Check On

- valid only for Frontal, Sparse and PCG Solvers

[SSTIF][PSTRES]

Stress stiffness or prestress Stress stiff ON

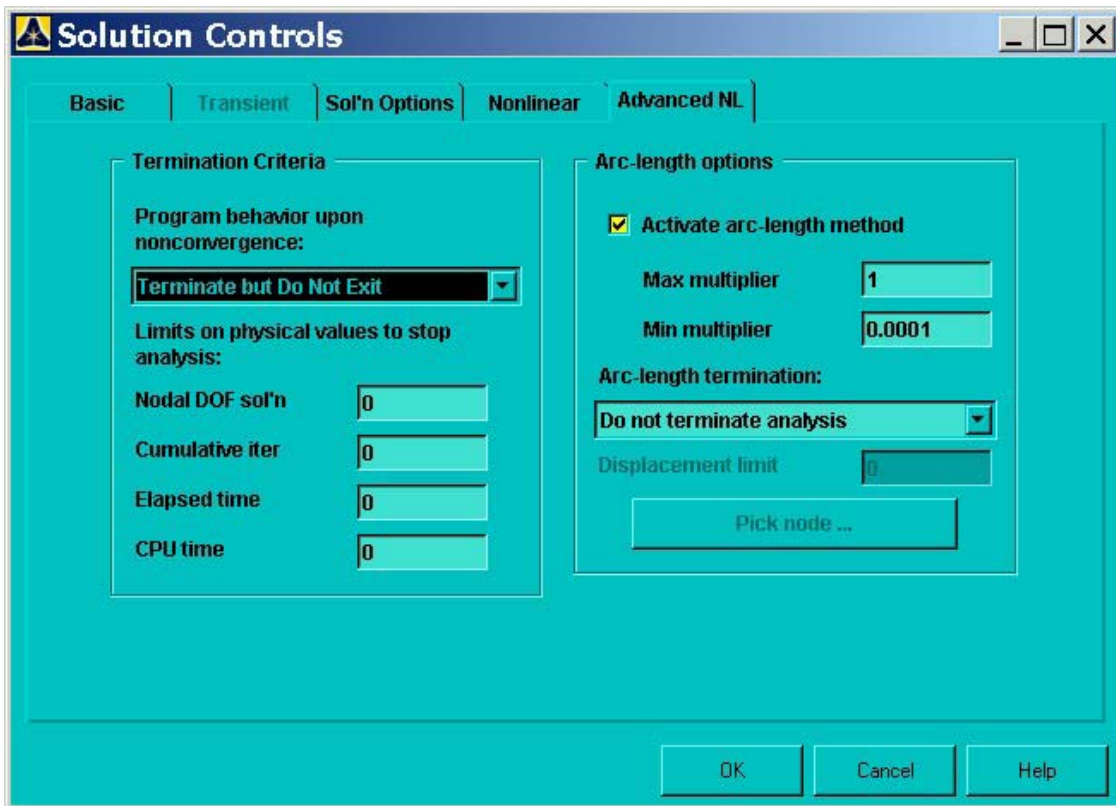
Note: If NLGEOM,ON then set SSTIF,ON.

[TOFFSI] Temperature difference- 0

- between absolute zero and zero of active temp scale

OK Cancel Help

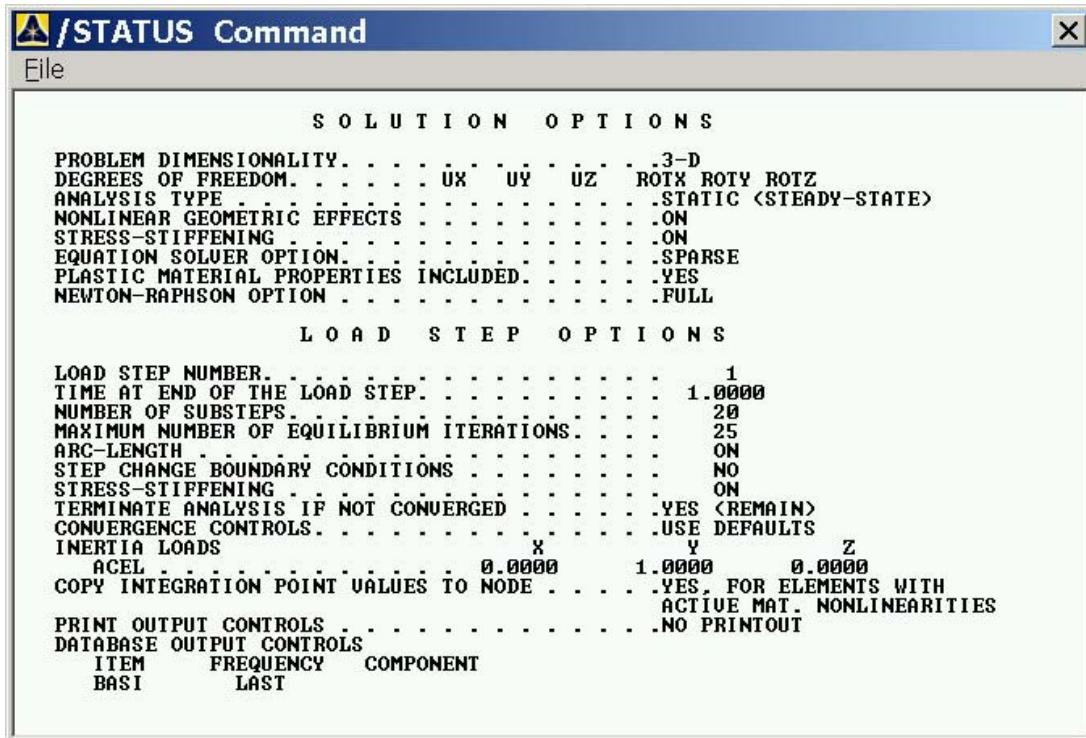
- 8.2. Choose menu path **Main Menu>Solution>Unabridged Menu-Load Step Opts-Time/Frequenc>Time and Substeps**. The Time and Substep Options dialog appears.
- 8.3. Type 1 for the **Time at the end of load step**, 20 for **Number of substeps**, 50 for **Maximum no. of substeps**, and 10 for **Minimum no. of substeps**. Click on **OK**.
- 8.4. Choose menu path **Main Menu>Solution>Unabridged>-Load Step Opts-Output Ctrls>DB/Results File**. The Control for Database and Results File Writing dialog appears. In the top drop down menu, select **Basic Quantities**, and click on **Every substep** button ration to turn it on. Click on **OK**.
- 8.5. Choose menu path **Main Menu>Solution>Unabridged Menu-Load Step Opt-Nonlinear>Arc-Length Opts**. The Arc-Length Options dialog appears. Click on the **Arc-length method on/off** button ration to turn it on. Type 1 for the **Maximum multiplier** and 0.0001 for the **Minimum multiplier**.
- 8.6. Choose menu path **Main Menu>Solution>Sol'n Control**. The Solution Controls dialog appears. Go to **Advanced NL**, in the Program behavior upon nonconvergence drop down menu, select **Terminate but Do Not Exit**. Click on **Ok**.



- 8.7. Click on **SAVE_DB** on the ANSYS Toolbar.

9. Solve the Analysis

- 9.1. Choose menu path **Main Menu>Solution>-Solve-Current LS**. Review the information in the /STATUS Command window, and click **File>Close**.



- 9.2. Click on **OK** on the Solve Current Load Step dialog box.



Note: The loads specify in this analysis is higher than the expected ultimate load of the beam. Therefore, the program will not terminate when the solution is done. The user has to stop the nonlinear analysis when the solution has converged, the ultimate load has been reached, and the load being applied is decreasing.

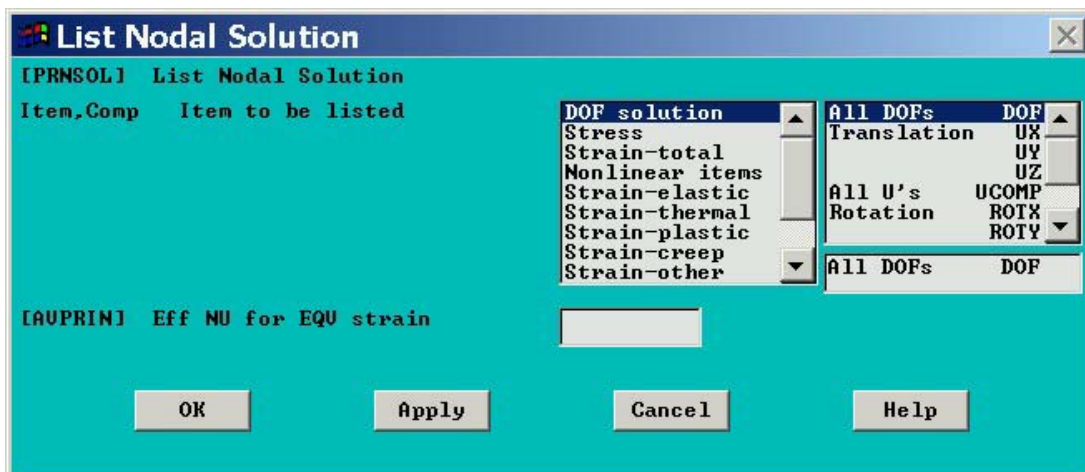
9.3. Click on **Close** on the Information dialog box when the solution is done.



10. Review the Results

10.1. Choose menu path **Main Menu>General Postproc>-ReadResults-First Set.**

10.2. Choose menu path **Main Menu>General Postproc>-List Result>Nodal Solution.** The List Nodal Solution dialog box appears. In the scroll box on the left, select **DOF Solution.** In the scroll box on the right select **All DOFs DOF.** Click on **Ok.**



10.3. Review the degrees of freedom at each node.

10.4. Choose menu path **Main Menu>General Postproc>Resul Summary.** The Result File: W14x22_4x144.rst dialog box appears. In the scroll box select any data set. Click on **Read.**



- 10.5. Choose menu path **Main Menu>General Postproc>Plot Results>Deformed Shape**. The Plot Deformed Shape dialog box appears. Click on **Def + undef edge** button radio. Click on **OK**. The deformed shape of the beam will appear in the ANSYS Graphic window.
- 10.6. Choose menu path **Main Menu>General Postproc>Plot Results>-Contour Plot>Nodal Solu**. The Contour Nodal Solution Data dialog box appears. In the scroll box on the top left, select **Stress**. In the scroll box on the right select **Z-direction SZ**. Click on **Ok**. The stress contour in z-direction will appear in the ANSYS Graphic window.
- 10.7. Choose menu path **Utility Menu>PoltCtrls>Capture Image**. A second ANSYS Graphic window appears. To save the image as a Bitmap file, choose **File Save As**.
- 10.8. Choose menu path **ANSYS Toolbar>Quit**. The Exit from ANSYS dialog box appears. Click on **Save Everything** button radio to select it.

Disclaimer:

I have made every effort to understand the applications and limitations of the finite element method, and the computer package, ANSYS 6.0. It was shown that the finite element models created in this study closely predicted the ultimate load and web crippling failure mode of the tested beams. However, I do not guarantee that the procedure presented in this section is the most accurate or proper procedure. The purpose of this section was to present the procedure used to create and analyze the finite element models, and to provide with an example problem that can be followed by others in order to get familiar with ANSYS 6.0.

APPENDIX B

FINITE ELEMENT RESULTS

This appendix presents the plots generated from the finite element results. The set of plots correspond to the web crippling responses of each model at different load steps. These responses were taken at the location of maximum out-of-plane deformation.

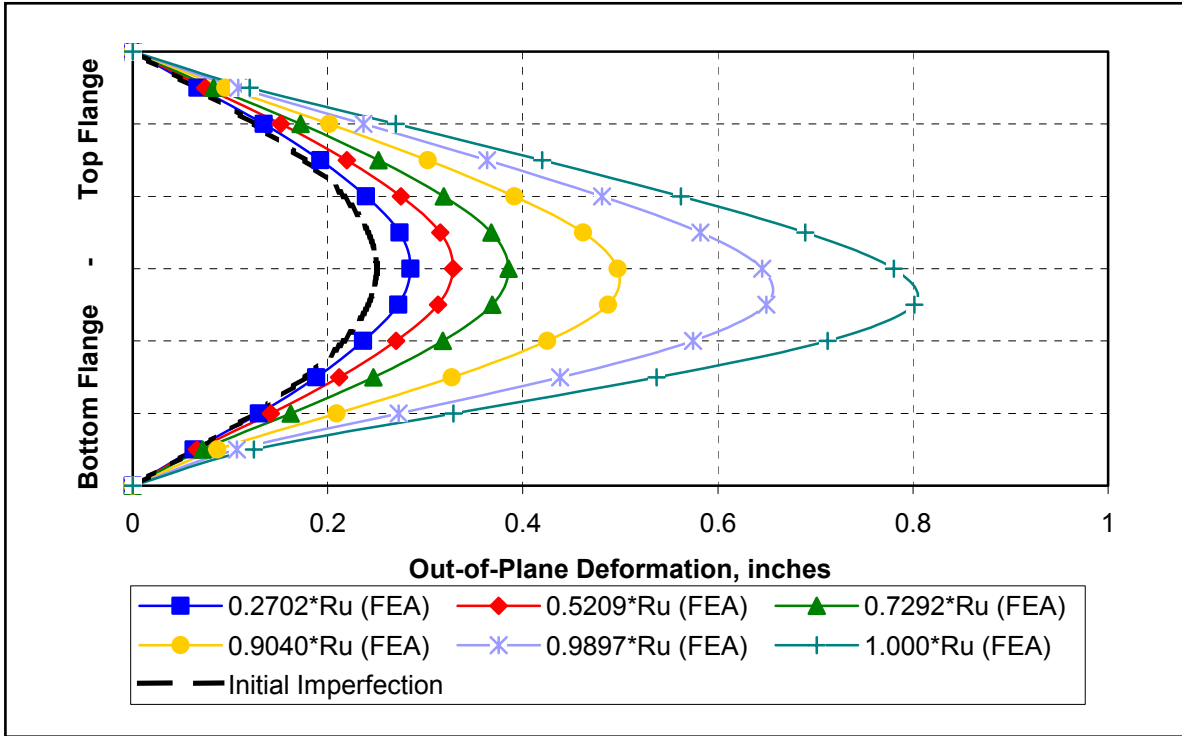


Figure B.1 Web crippling shape at different load steps of the model FEA-14a.

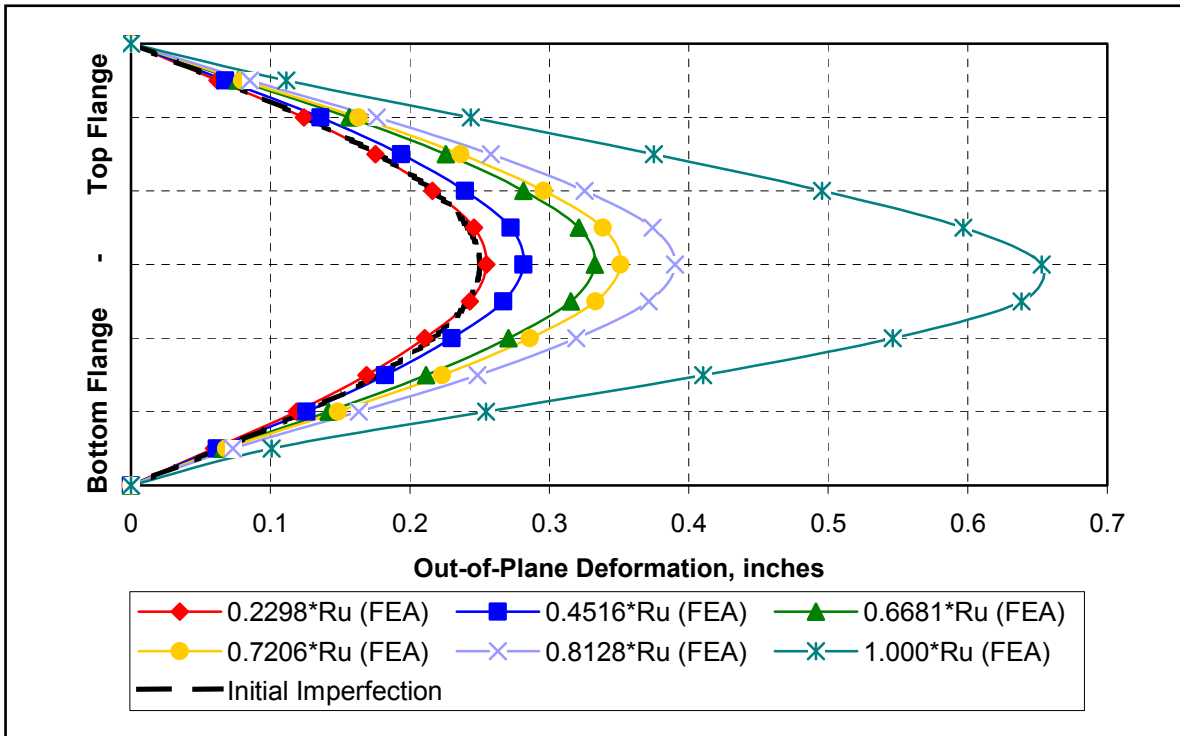


Figure B.2 Web crippling shape at different load steps of the model FEA-14b.

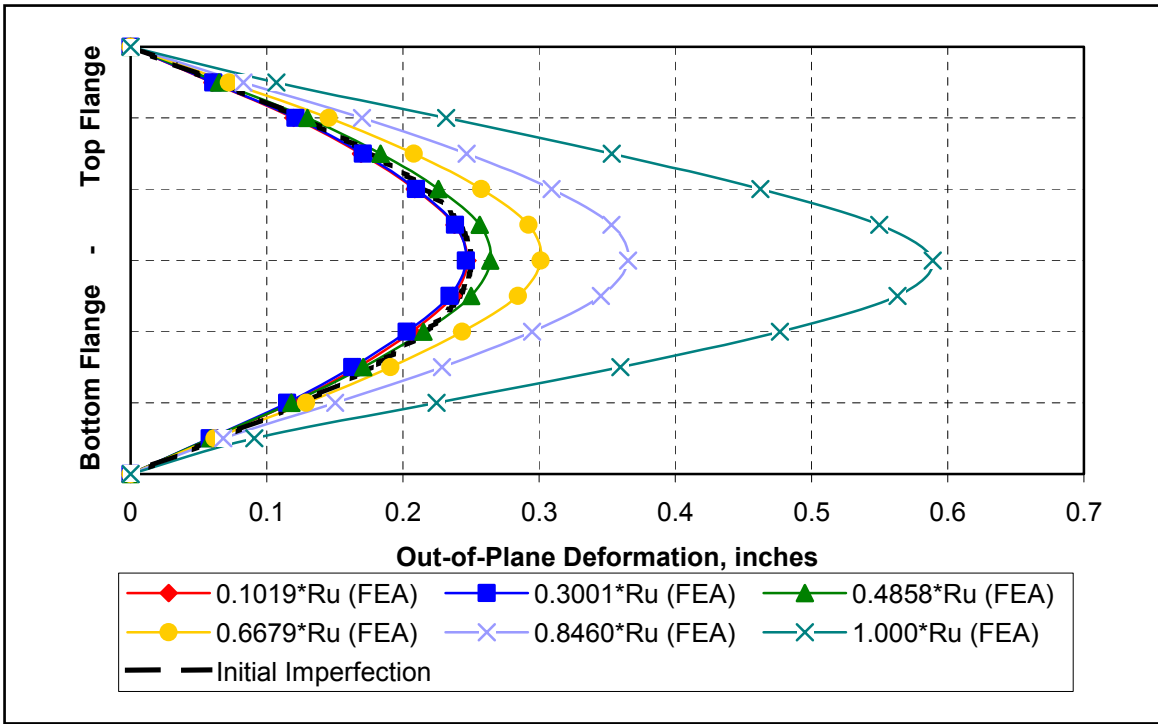


Figure B.3 Web crippling shape at different load steps of the model FEA-14c.

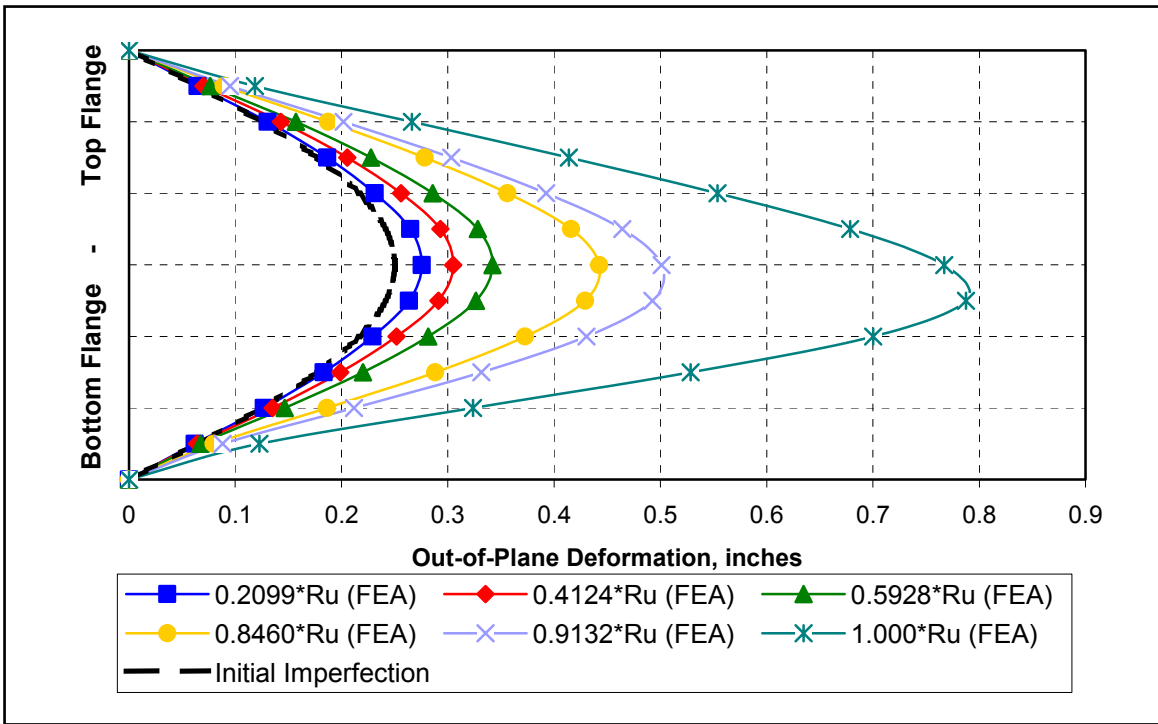


Figure B.4 Web crippling shape at different load steps of the model FEA-15a.

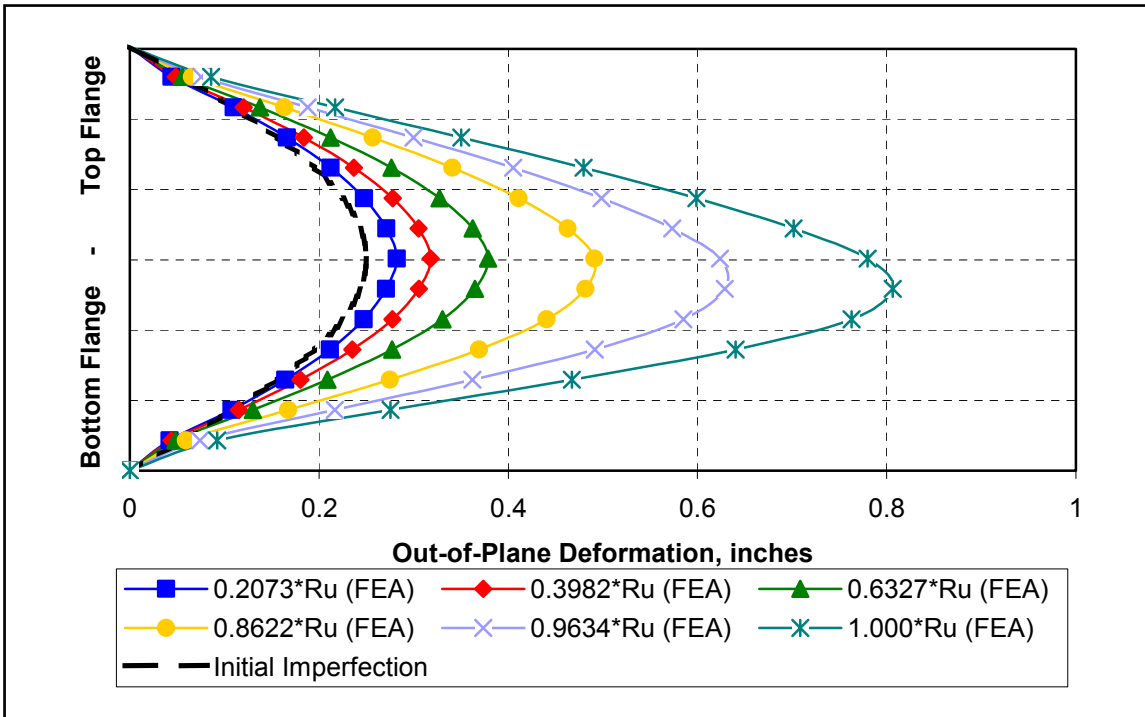


Figure B.5 Web crippling shape at different load steps of the model FEA-4a.

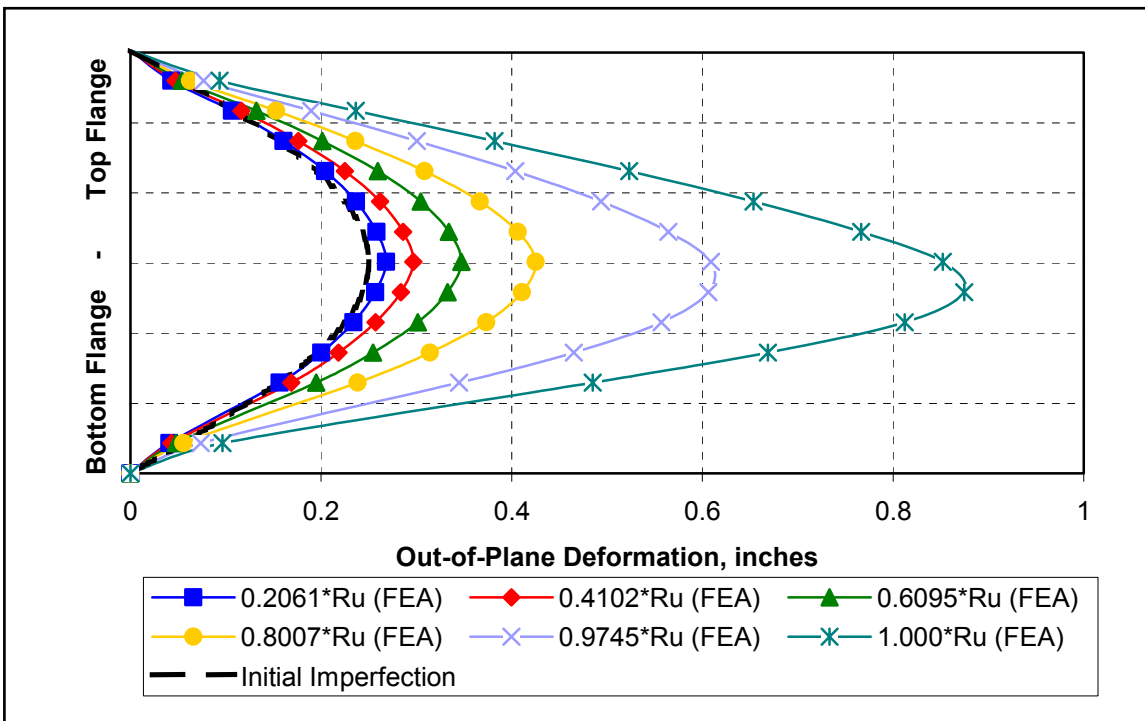


Figure B.6 Web crippling shape at different load steps of the model FEA-4b.

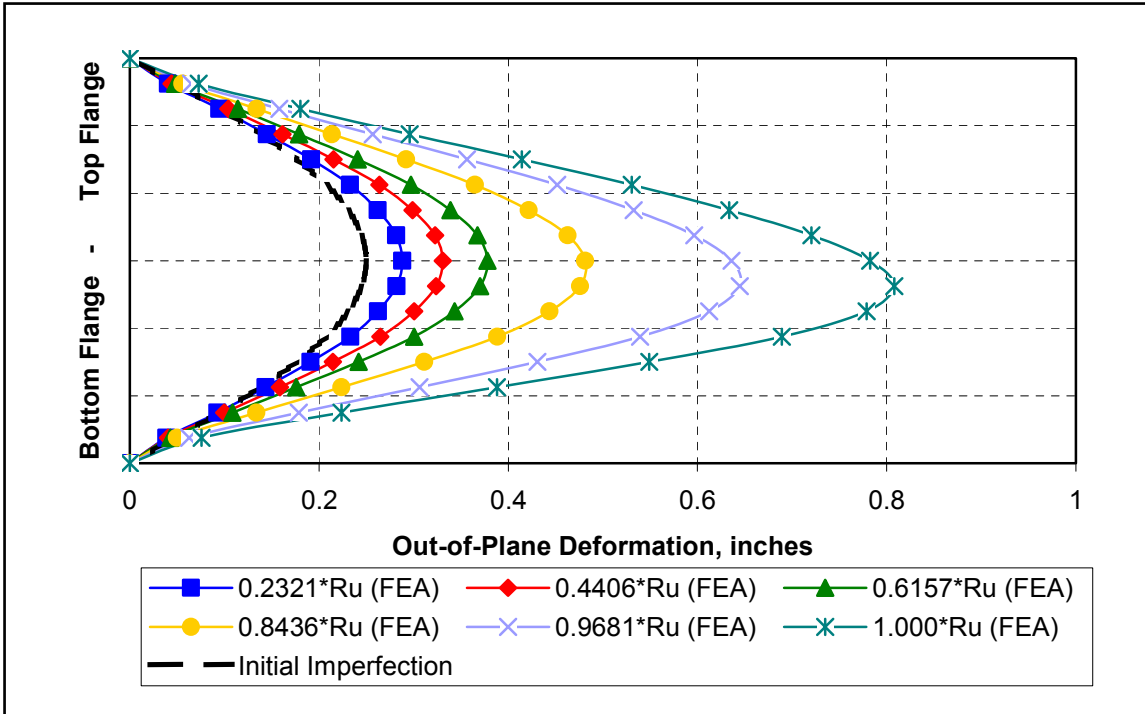


Figure B.7 Web crippling shape at different load steps of the model FEA-7a.

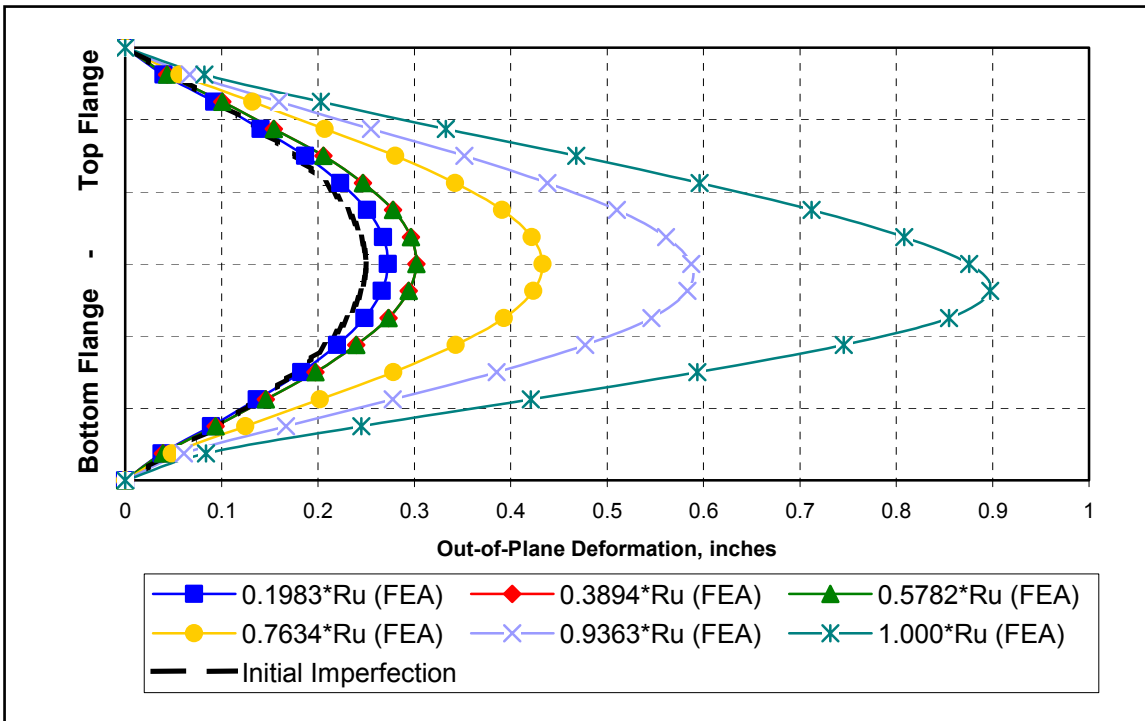


Figure B.8 Web crippling shape at different load steps of the model FEA-7b.

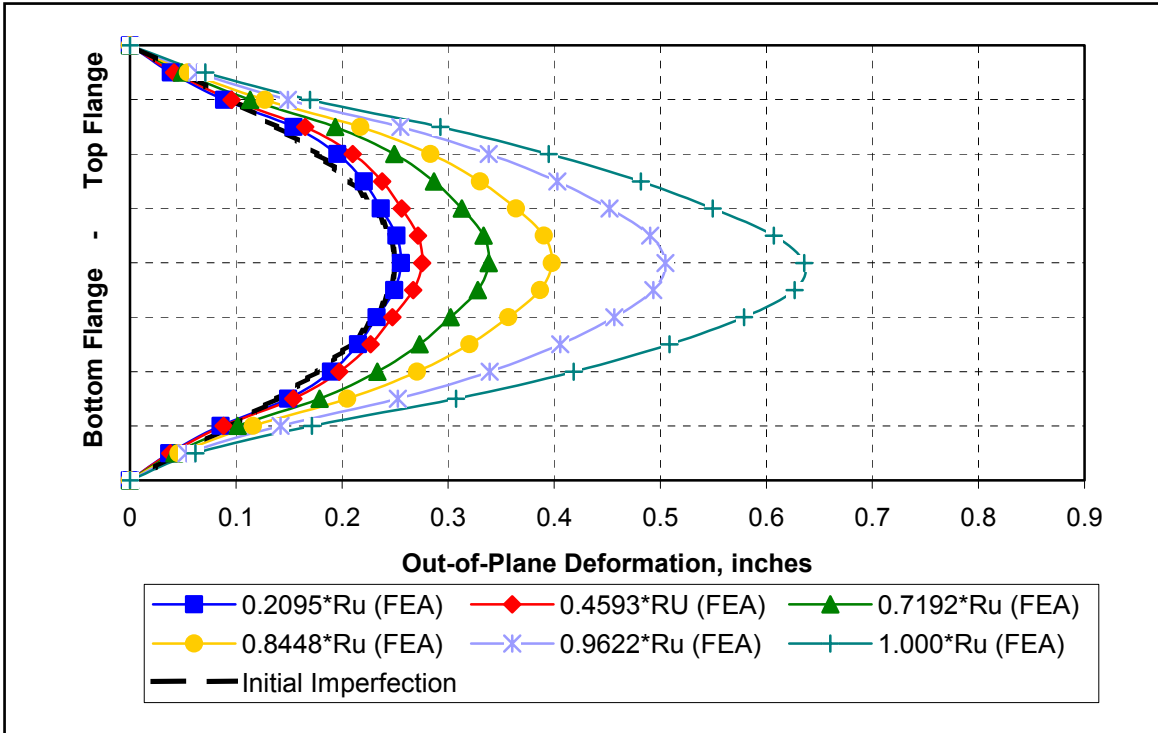


Figure B.9 Web crippling shape at different load steps of the model FEA-7c.

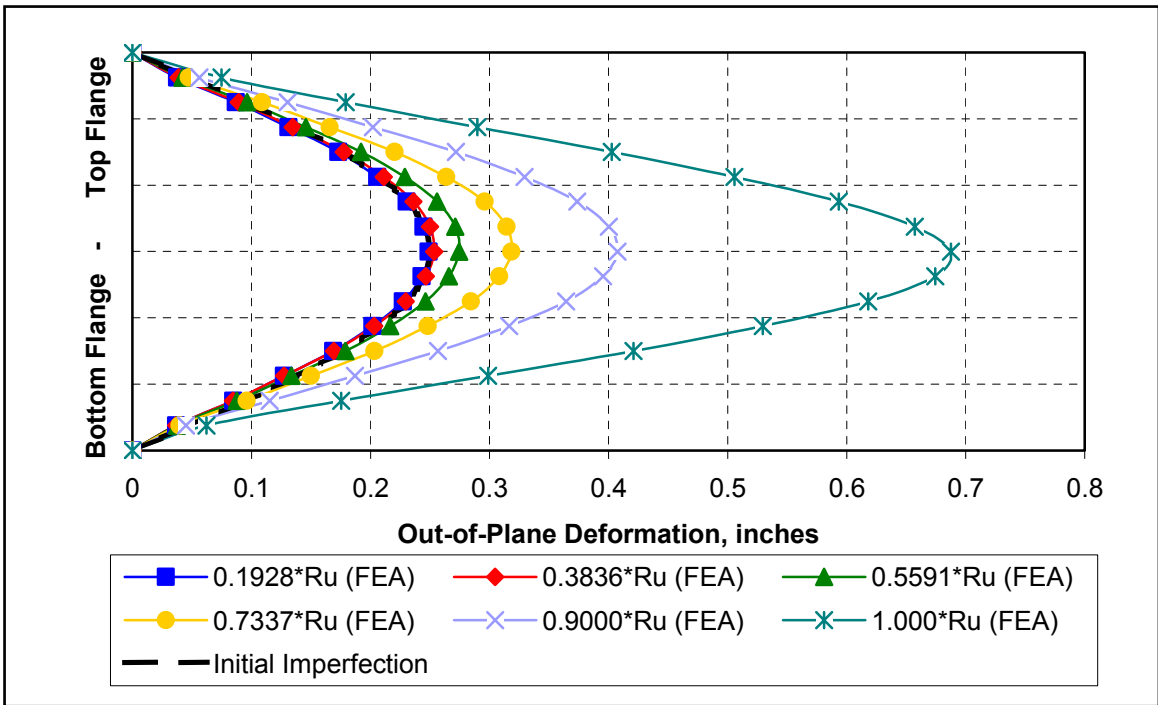


Figure B.10 Web crippling shape at different load steps of the model FEA-7d.

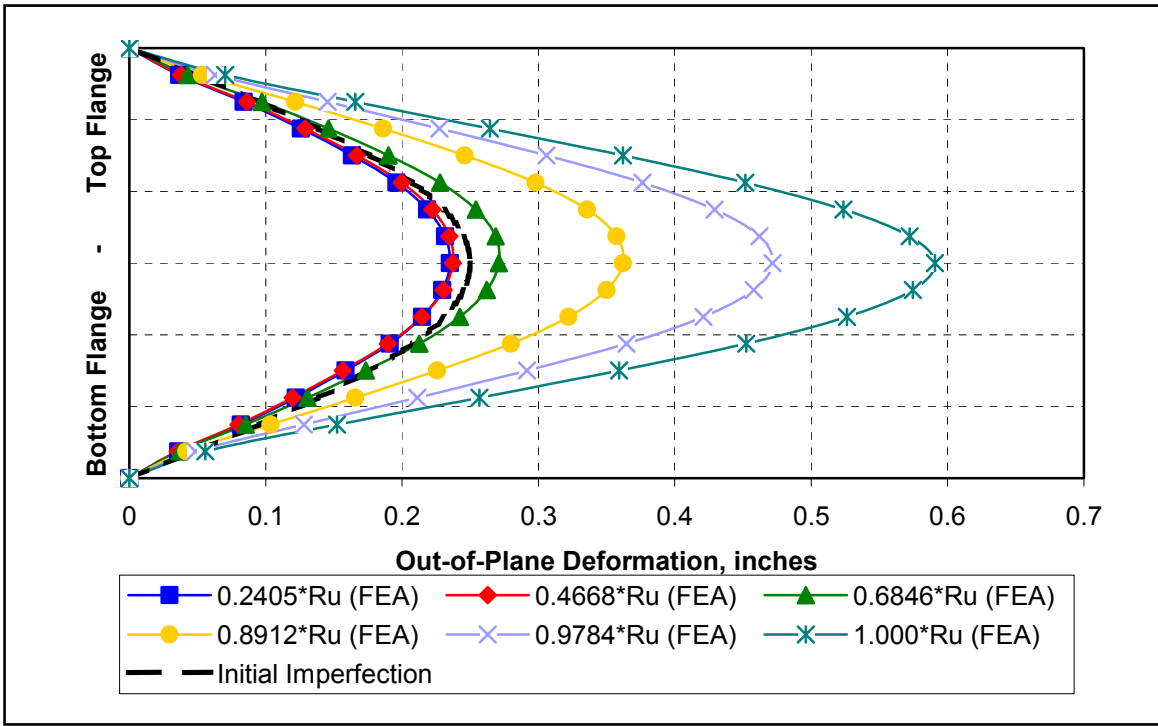


Figure B.11 Web crippling shape at different load steps of the model FEA-7e.

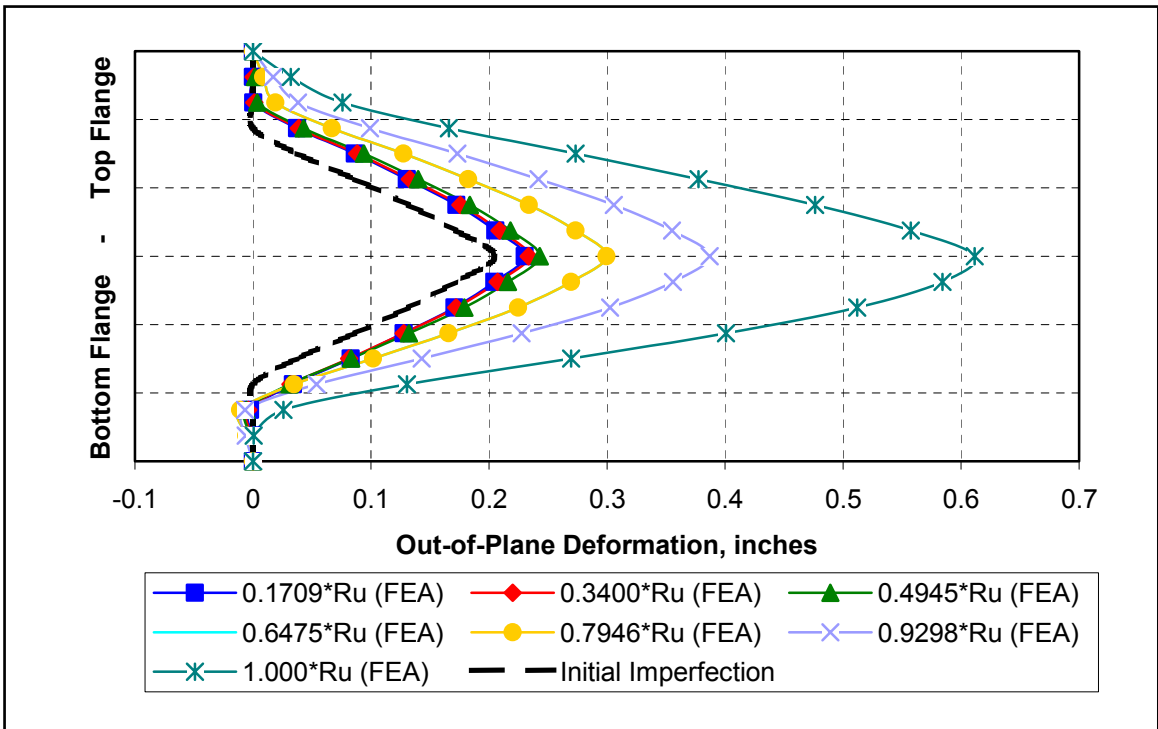


Figure B.12 Web crippling shape at different load steps of the model FEA-7f.

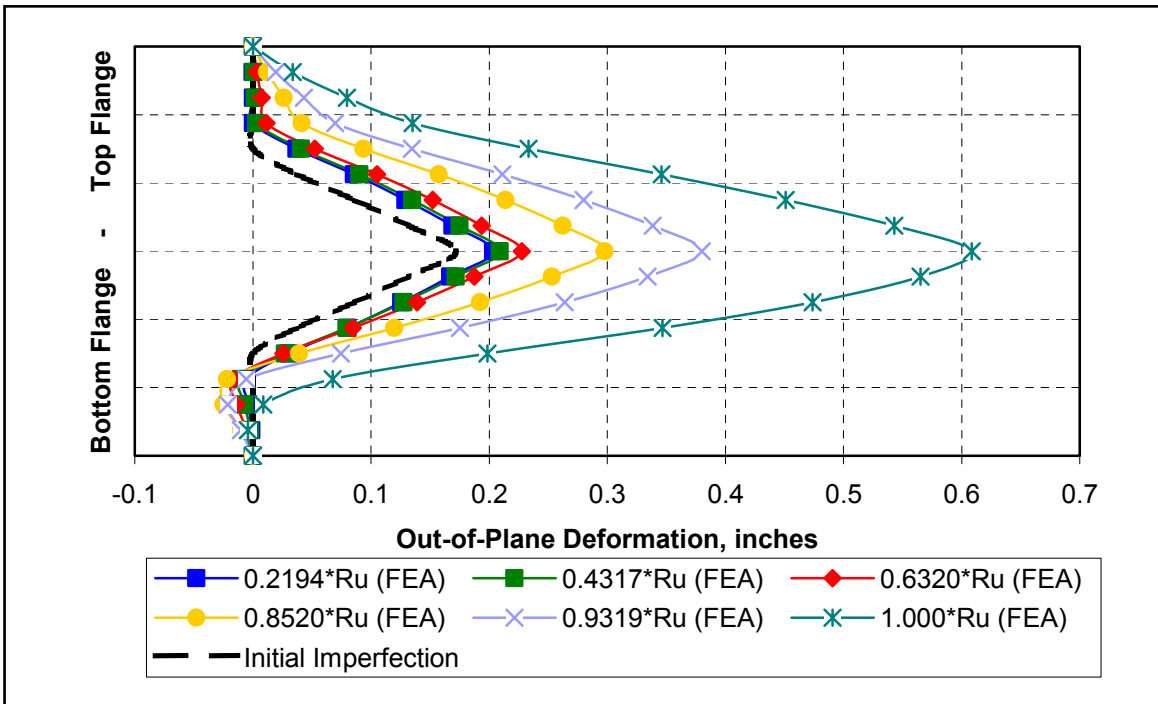


Figure B.13 Web crippling shape at different load steps of the model FEA-7g.

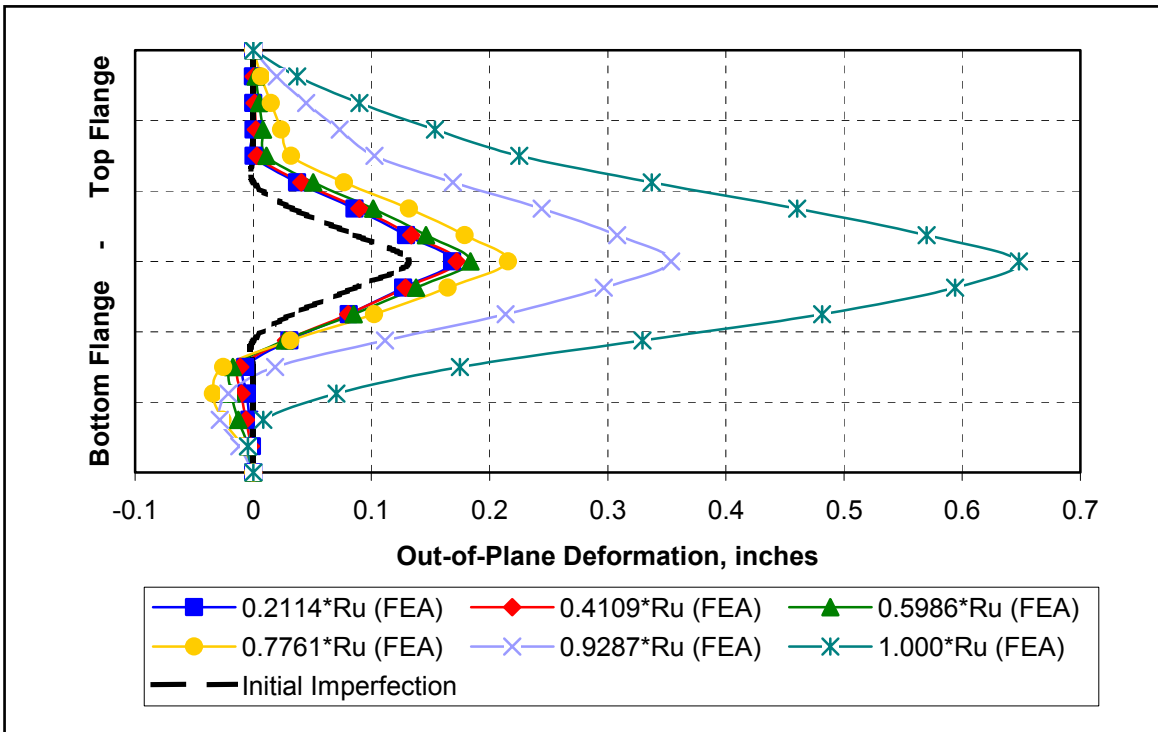


Figure B.14 Web crippling shape at different load steps of the model FEA-7h.

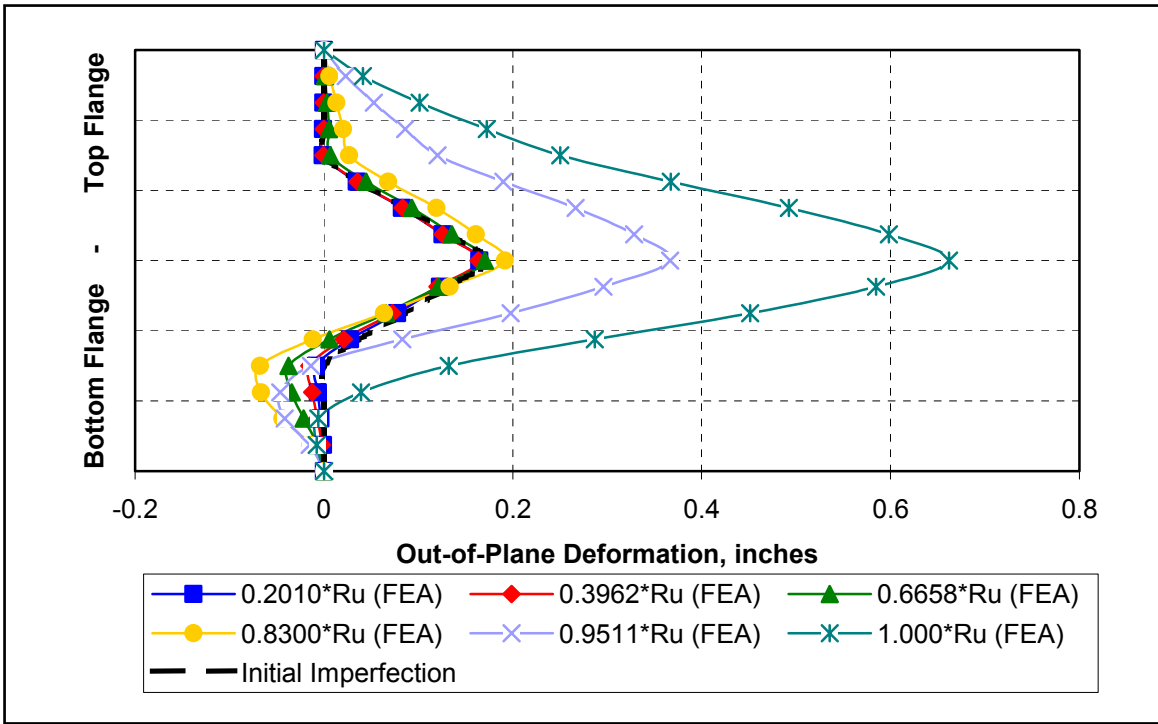


Figure B.15 Web crippling shape at different load steps of the model FEA-7i.

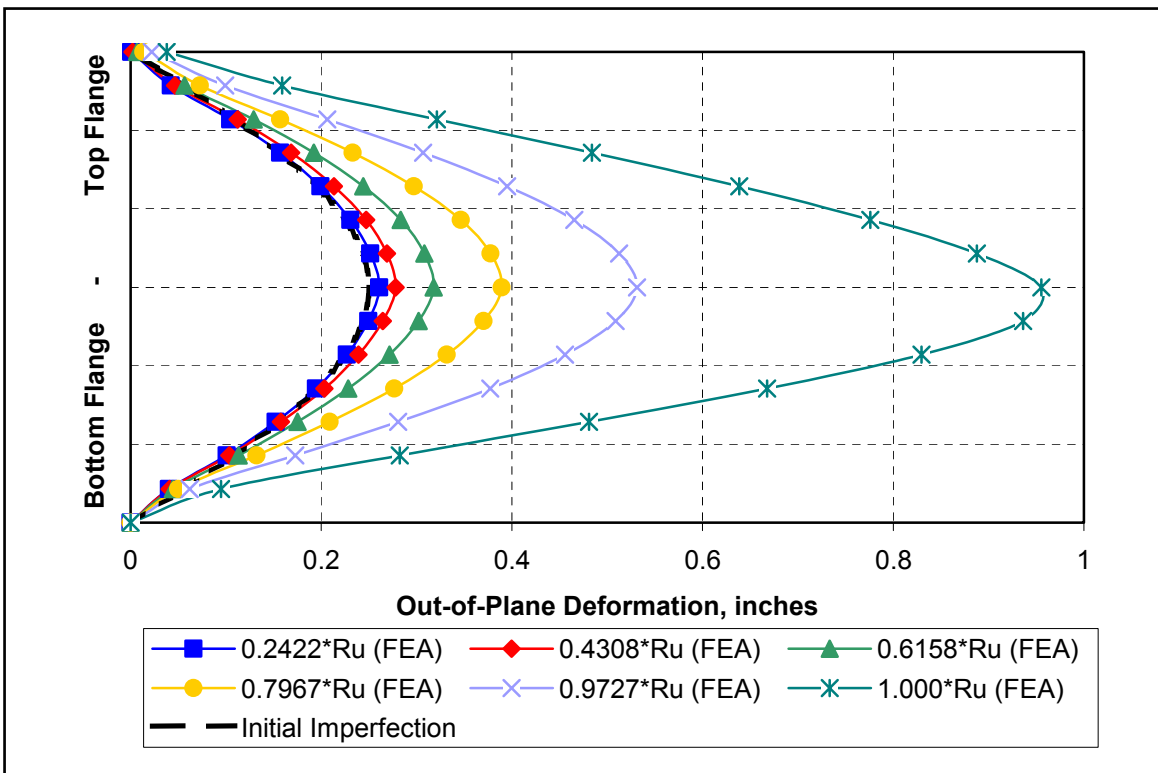


Figure B.16 Web crippling shape at different load steps of the model FEA-SC-2a.

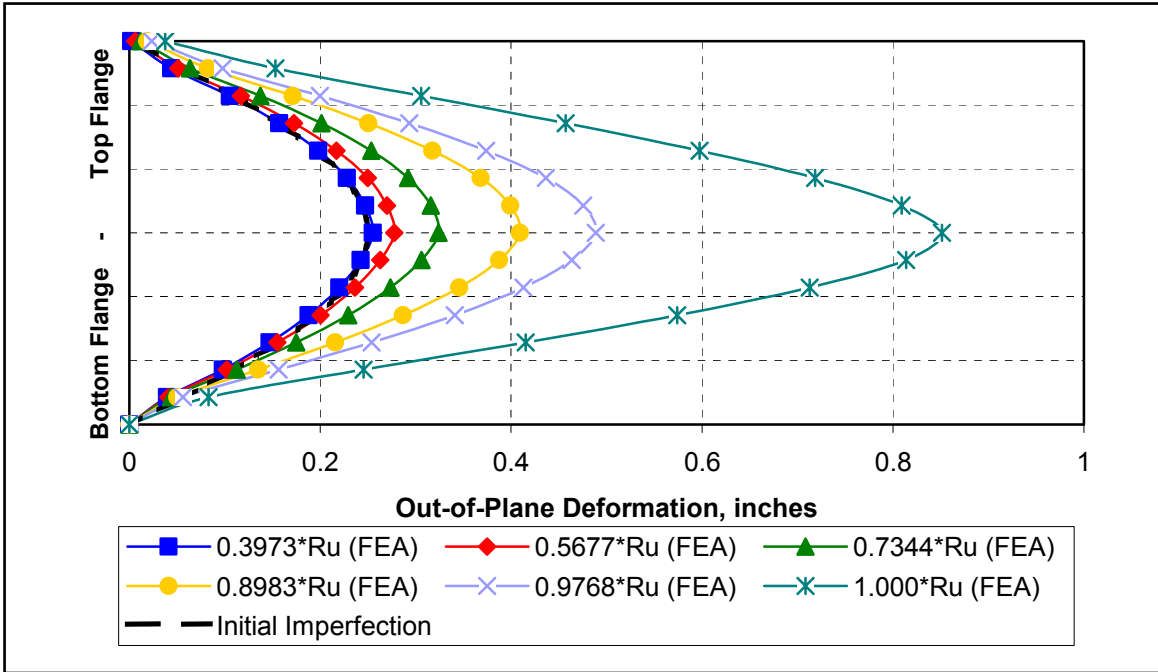


Figure B.17 Web crippling shape at different load steps of the model FEA-SC-2b.

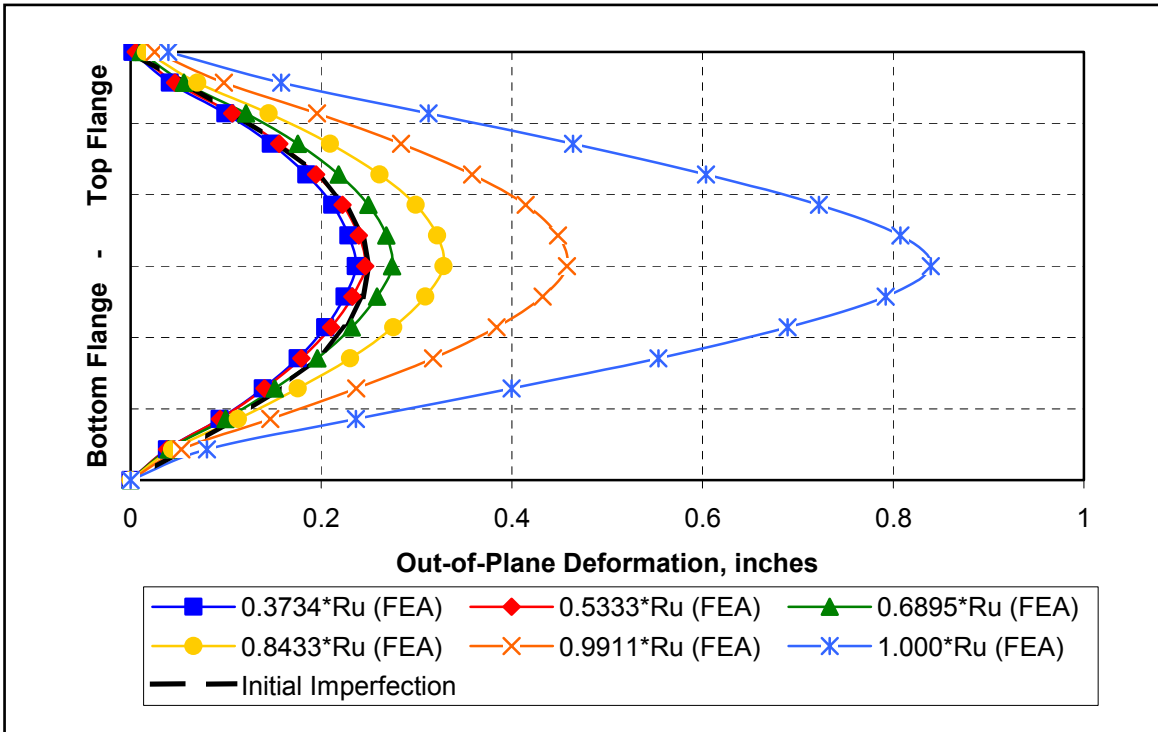


Figure B.18 Web crippling shape at different load steps of the model FEA-SC-2c.

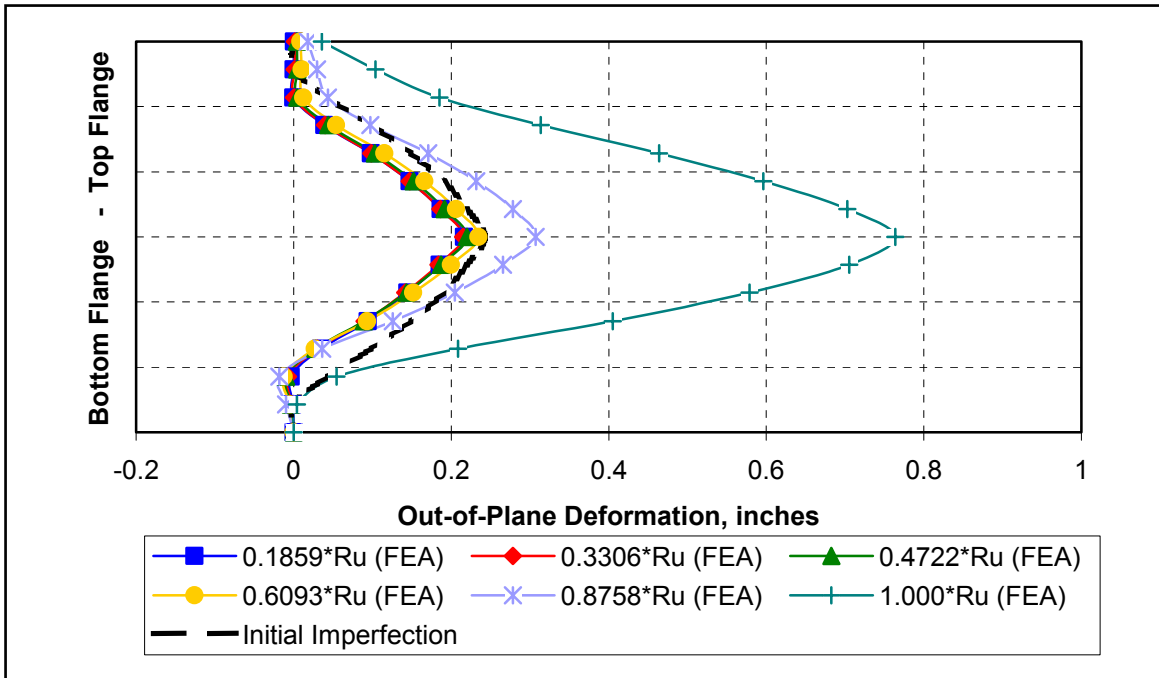


Figure B.19 Web crippling shape at different load steps of the model FEA-SC-2d.

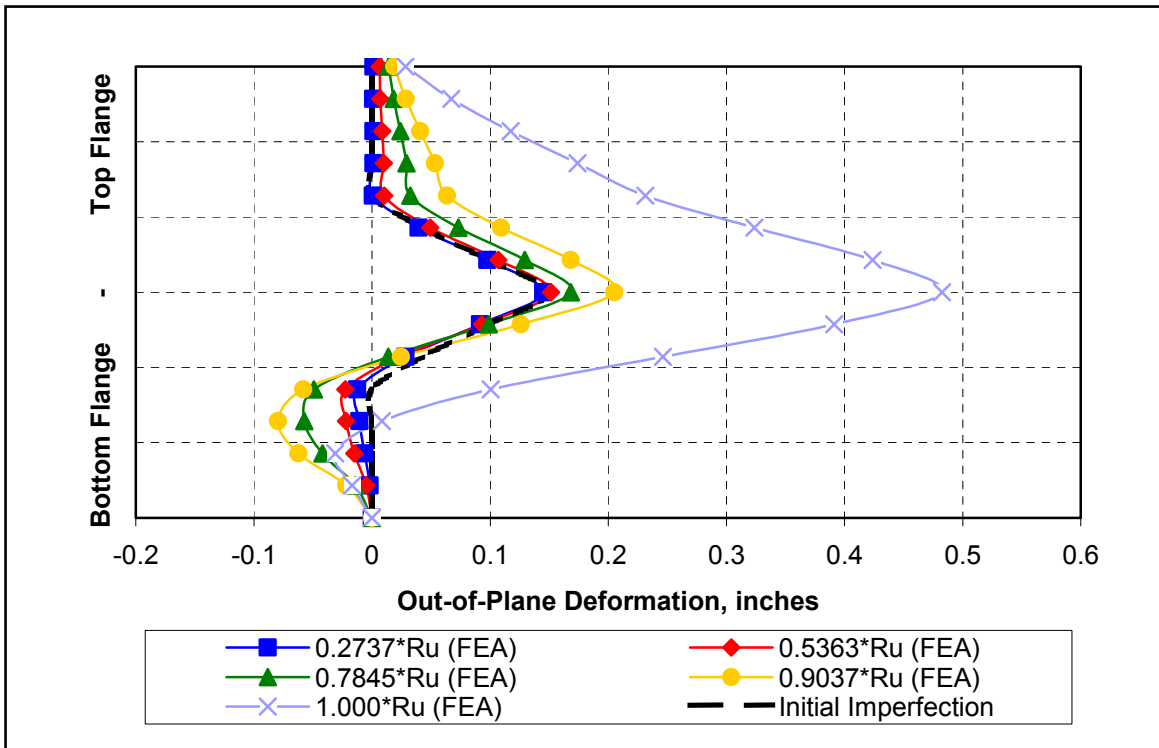


Figure B.20 Web crippling shape at different load steps of the model FEA-SC-2e.

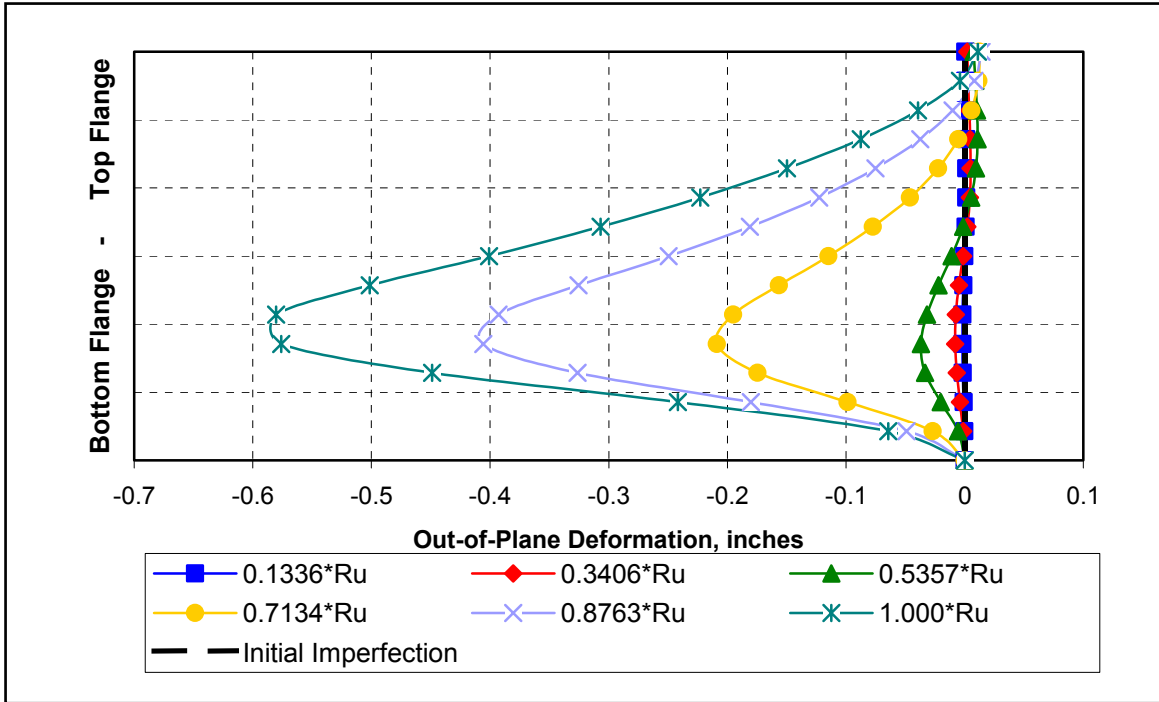


Figure B.21 Web crippling shape at different load steps of the model FEA-SC-2f.

APPENDIX C

ADDITIONAL SCREENED END WEB CRIPPLING DATA

This appendix presents additional screened end web crippling data not included in Chapter 2. This experimental data corresponds to tests conducted by Ketchum and Draffin (1932).

Table C.1.

Summary of the geometric and material properties for the series F tests conducted by Ketchum and Draffin.

Test Designation	Beam Section	Span (in.)	N (in.)	t_w (in.)	t_f (in.)	d (in.)	b_f (in.)	F_y (ksi)
F1	M10x9	16.00	1.920	0.1700	0.2060	10.00	2.6900	36.40
F2	M10x9	16.00	1.920	0.1670	0.2060	10.00	2.6900	36.40
F3	M6x4.4	10.00	1.920	0.1270	0.1710	6.00	1.8440	43.40
F4	M6x4.4	10.00	1.920	0.1320	0.1710	6.00	1.8440	43.40
F6	M6x4.4	10.80	1.200	0.1160	0.1710	6.00	1.8440	43.40
F7	M10x9	15.00	2.960	0.1520	0.2060	10.00	2.6900	36.40
F8	M10x9	15.00	2.960	0.1540	0.2060	10.00	2.6900	36.40
F21	M12x11.8	21.00	2.960	0.1670	0.2250	12.00	3.0650	43.70
F22	M12x11.8	21.00	2.960	0.1680	0.2250	12.00	3.0650	43.70
F23	M12x11.8	22.10	1.920	0.1690	0.2250	12.00	3.0650	43.70
F24	M12x11.8	22.10	1.920	0.1700	0.2250	12.00	3.0650	43.70
F25	M12x11.8	22.80	1.200	0.1700	0.2250	12.00	3.0650	43.70
F26	M12x11.8	22.80	1.200	0.1680	0.2250	12.00	3.0650	43.70
F27	M12x11.8	20.80	1.200	0.1710	0.2250	12.00	3.0650	43.70
F28	M12x11.8	18.50	2.960	0.1690	0.2250	12.00	3.0650	43.70

Table C.2.

Summary of the geometric and material properties for the midspan-loaded series K tests conducted by Ketchum and Draffin.

Test Designation	Beam Section	Span (in.)	N (in.)	t_w (in.)	t_f (in.)	d (in.)	b_f (in.)	F_y (ksi)
K35	M10x9	21.75	1.750	0.1590	0.2060	10.00	2.690	36.40
K36	M10x9	21.75	1.750	0.1610	0.2060	10.00	2.690	36.40
K41	M10x9	23.50	3.500	0.1640	0.2060	10.00	2.690	36.40
K42	M10x9	23.50	3.500	0.1640	0.2060	10.00	2.690	36.40

Table C.3.

Summary of the geometric and material properties for the midspan-loaded series K tests conducted by Ketchum and Draffin, and which the beam was projected beyond the outer edge of the bearing block.

Test Designation	Beam Section	Span (in.)	N ** (in.)	t _w (in.)	t _f (in.)	d (in.)	b _f (in.)	F _y (ksi)
K37	M10x9 *	21.00	1.750	0.163	0.206	10.00	2.690	36.40
K38	M10x9 *	21.00	1.750	0.161	0.206	10.00	2.690	36.40
K39	M10x9 *	21.00	3.000	0.163	0.206	10.00	2.690	36.40
K40	M10x9 *	21.00	3.000	0.161	0.206	10.00	2.690	36.40
K43	M10x9 *	21.75	3.500	0.160	0.206	10.00	2.690	36.40
K44	M10x9 *	21.75	3.500	0.157	0.206	10.00	2.690	36.40

* Bearing plate was not aligned with the end of the beam.

** N is the distance from the end of the beam to the end of the bearing plate.

Table C.4.

Summary of the screened web crippling strength results from experimental studies conducted by Ketchum and Draffin.

Test Designation	Beam Section	N/d	Experimental Failure Load, R_U (kips)	1999 AISC LRFD Specification, R_{AISC} (kips)	R_U / R_{AISC}
F1	M10x9	0.1920	18.00	18.72	0.9615
F2	M10x9	0.1920	18.55	18.08	1.026
F3	M6x4.4	0.3200	14.00	13.56	1.032
F4	M6x4.4	0.3200	12.91	14.69	0.8809
F6	M6x4.4	0.2000	9.850	9.790	1.006
F7	M10x9	0.2960	19.42	17.28	1.124
F8	M10x9	0.2960	17.42	17.74	0.9820
F21	M12x11.8	0.2470	13.42	21.47	0.6250
F22	M12x11.8	0.2470	16.22	21.73	0.7464
F23	M12x11.8	0.1600	19.12	19.48	0.9815
F24	M12x11.8	0.1600	19.02	19.69	0.9658
F25	M12x11.8	0.1000	11.18	17.92	0.6239
F26	M12x11.8	0.1000	15.01	17.55	0.8553
F27	M12x11.8	0.1000	13.81	18.11	0.7626
F28	M12x11.8	0.2470	20.10	21.99	0.9140
K35	M10x9	0.1750	18.84	16.04	1.174
K36	M10x9	0.1750	18.29	16.42	1.114
K37	M10x9 *	0.1750	18.10	16.81	1.077
K38	M10x9 *	0.1750	16.94	16.42	1.032
K39	M10x9 *	0.3000	19.30	20.05	0.9626
K40	M10x9 *	0.3000	18.44	19.54	0.9437
K41	M10x9	0.3500	21.35	21.63	0.9870
K42	M10x9	0.3500	19.48	21.63	0.9006
K43	M10x9 *	0.3500	20.18	20.52	0.9834
K44	M10x9 *	0.3500	23.17	19.71	1.176

* Bearing plate was not aligned with the end of the beam.

VITA

Abigail Marcano was born in San Juan, Puerto Rico on January 16, 1976 to Rufina Rivera and Abigail Marcano Sr. He is the youngest of three children. Abigail graduated from the University of Puerto Rico at Mayagüez, where he obtained his Bachelor of Science Degree in Civil Engineering in June 2000. In the fall of 2000, he joined the Structural Engineering and Materials Program of the Charles E. Via Department of Civil Engineering at Virginia Polytechnic Institute and State University to continue an academic career towards a Master's Degree in Civil Engineering. He worked as a Quality Control Technician for a ready mixed concrete producer in summer of 1999, and as an Assistant Bridge Engineer at the Federal Highway Administration Puerto Rico office in summer of 2001. Abigail legally adopted José as his first name in July 2002. José Abigail will be working as a Pipe Stress Analyst for Bechtel Power Corporation in Frederick, MD. José Abigail proudly received the degree of Master of Science in Civil Engineering in August 2002.